TECHNISCHE UNIVERSITÄT MÜNCHEN

Fakultät für Chemie

Enhancement and Degradation of the Graphite Electrode Kinetics in Vanadium Redox Flow Batteries

Tobias Greese

Vollständiger Abdruck der von der Fakultät für Chemie der Technischen Universität München zur Erlangung des akademischen Grades eines

Doktors der Naturwissenschaften (Dr. rer. nat.)

genehmigten Dissertation.

Vorsitzender:	Prof. Dr. Sebastian Günther
Prüfer der Dissertation:	1. Prof. Dr. Hubert A. Gasteiger
	2. Prof. Dr. Christina Roth

Diese Dissertation wurde am 23.05.2022 bei der Technischen Universität München eingereicht und durch die Fakultät für Chemie am 19.07.2022 angenommen.

„Du musst nur eine gute Geschichte erzählen, möglichst einfach und ohne Mathe.“

- Susi Greese -

Abstract

The performance of graphite electrodes in vanadium redox flow batteries (VRFB) is significantly limited by the sluggish kinetics of the V^{2+}/V^{3+}-reaction at the anode. It is still unclear which surface property most effectively improves the kinetics, although a central role is ascribed to oxygen functionalities. Furthermore, the anode kinetics are found to continuously deteriorate during operation, a degradation effect that has been frequently described in the literature, but for which no conclusive explanation has yet been provided.

The first part of this thesis rigorously studies how a combination of plasma and thermal treatment modifies the surface properties of graphite felt electrodes and, thus, how it improves their performance in VRFB single-cells. Surprisingly, oxygen functionalities are shown to be not primarily responsible for the improved performance, contrary to what is commonly assumed in the literature. Instead, decisive for the phenomenon are a high surface roughness and surface area and, accordingly, the number of carbon edge sites. In addition, electrodes with high roughness and area also show less degradation of the electrode kinetics in long-term operation.

The second part of this thesis proposes a new mechanism, providing an explanation for the anode kinetics degradation. In three-electrode half-cells, graphitic rotating disk electrodes are investigated for their electrochemical response in a sulfuric acid electrolyte containing different amounts of V^{2+}, V^{3+}, and VO^{2+}. It is shown that in the presence of V^{2+} the kinetics for the V^{2+}/V^{3+}-reaction decreases at cathodic potentials, while it regenerates at anodic potentials. Moreover, even low concentrations of V^{2+} are sufficient to inhibit the hydrogen evolution reaction (HER) that is typically strongly pronounced in a vanadium-free electrolyte. According to the new mechanism, V^{2+} is proposed to adsorb on the electrode surface, forming an equilibrium coverage and inhibiting the V^{2+}/V^{3+}-reaction as well as the HER. Correspondingly, a new operation strategy for VRFB full cells demonstrates that the degraded anode kinetics are completely regenerated upon reversing the electrode polarity, which increases the average electrode performance in long-term VRFB operation.

Kurzzusammenfassung

Die Leistung von Graphitelektroden in Vanadium-Redox-Flow-Batterien (VRFB) wird maßgeblich beschränkt durch die träge Kinetik der V^{2+}/V^{3+}-Reaktion an der Anode. Dabei ist noch unklar, welche Oberflächeneigenschaft die Kinetik am effektivsten verbessert, wobei den Sauerstofffunktionalitäten eine zentrale Rolle zugesprochen wird. Darüber hinaus zeigt sich, dass sich die Anodenkinetik während des Betriebs kontinuierlich verschlechtert, ein Degradationseffekt, der in der Literatur zwar mehrfach beschrieben wurde, für den aber noch keine schlüssige Erklärung geliefert werden konnte.

Im ersten Teil dieser Arbeit wird eingehend untersucht, wie eine Kombination aus Plasma- und Wärmebehandlung die Oberflächeneigenschaften von Graphitfilzelektroden verändert und damit ihre Leistung in VRFB-Vollzellen verbessert. Überraschenderweise sind für die verbesserte Leistung primär nicht die Sauerstofffunktionalitäten verantwortlich, entgegen der häufigen Annahme in der Literatur. Stattdessen ausschlaggebend ist eine hohe Oberflächenrauheit und Oberfläche und damit einhergehend die Anzahl an Kohlenstoffrandstellen. Darüber hinaus ist bei Elektroden mit hoher Rauheit und Fläche auch die Degradation der Kinetik weniger stark ausgeprägt.

Im zweiten Teil dieser Arbeit wird ein neuer Mechanismus vorgeschlagen, der eine Erklärung für die Degradation der Anodenkinetik bietet. In Drei-Elektroden-Halbzellen werden graphitische Rotierende-Scheibenelektroden auf ihr elektrochemisches Verhalten in einem Schwefelsäureelektrolyten untersucht, der unterschiedliche Mengen von V^{2+}, V^{3+} und VO^{2+} enthält. In Gegenwart von V^{2+} nimmt demnach die Elektrodenkinetik für die V^{2+}/V^{3+}-Reaktion bei kathodischen Potentialen ab, während sie bei anodischen Potentialen regeneriert werden kann. Darüber hinaus hemmen schon niedrige V^{2+}-Konzentrationen die Wasserstoffentwicklungsreaktion (HER), welche in einem vanadiumfreien Elektrolyten typischerweise stark ausgeprägt ist. Entsprechend dem neuen Mechanismus adsorbiert V^{2+} an der Elektrodenoberfläche, bildet dabei eine Gleichgewichtsbedeckung aus und hemmt die V^{2+}/V^{3+}-Reaktion sowie die HER. Daraus abgeleitet zeigt eine neue Betriebsstrategie für VRFB-Vollzellen, dass die degradierte Elektrodenkinetik im Zuge einer Umkehrung der Elektrodenpolarität vollständig regeneriert wird, was die durchschnittliche Elektrodenleistung im langfristigen Batteriebetrieb erhöht.

Contents

List of Acronyms

Abbreviation	**Desciption**
AEM	anion exchange membrane
ASA	active surface area
CE	counter electrode
CEM	cation exchange membrane
BET	brunauer-emmett-teller
BPP	bipolar plate
ECSA	electrochemically active surface area
EIS	electrochemical impedance spectroscopy
ETFE	ethylene tetrafluoroethylene
FEP	fluor-ethylene-propylene
GC	glassy carbon
GF	graphite felt
HER	hydrogen evolution reaction
HOPG	highly oriented pyrolytic graphite
HPL	highly pressurized laminate
IDFF	interdigitated flow field
IEM	ion exchange membrane
MPP	monopolar plate
OCP	open circuit potential
OCV	open circuit voltage
OER	oxygen evolution reaction
PAN	polyacrylonitrile
PC	polycarbonate
PE	polyethylene
PP	polypropylene
PTFE	polytetrafluoroethylene
PVC	polyvinylchloride
TSA	total surface area

RE	reference electrode
RDE	rotating disk electrode
RFB	redox flow battery
SEM	scanning electron microscopy
short-GCP	short galvanostatic cell polarization
SoC	state-of-charge
VRFB	vanadium redox flow battery
WE	working electrode
XPS	x-ray photoelectron microscopy

1. Introduction

The observed global warming already leads to significant socio-economic costs, which are predicted to intensify with every rise in average temperature in the future.[1] The temperature rise scales with the atmosphere's carbon dioxide (CO_2) content, which continuously increases due to the wide use of fossil fuels in all energy sectors,[2,3,4] eventually rendering parts of the globe uninhabitable.[5] Consequently, leading economies around the world commit to abandoning technologies that rely on fossil fuels in order to reduce carbon dioxide emissions. Instead, they aim at deploying more renewable energy sources such as wind and solar power, especially for generating electricity. Accordingly, fossil-fueled power plants commonly fired by coal or gas are substituted by CO_2-neutral wind power stations and photovoltaics.[6] These renewable systems convert the energy instantaneously, meaning their power output requires that wind and sunlight are, in fact, available when needed. However, the volatility of such sources can lead to a temporal mismatch in energy demand and supply.[7,8] Stationary electrical energy storage systems can bridge this gap in the time domain, offering to harvest excessive energy and to store it until needed.[9,10]

For this purpose, all-vanadium redox flow batteries (VRFB) meet the requirements of being reliable in use, flexible in size, and efficient in energy and cost,[11,12] and have already been demonstrated in the power and capacity size class of MW and MWh.[13] As energy carriers and reactive species, they employ vanadium at different valencies, dissolved in aqueous sulphuric acid. During charge and discharge, the vanadium ions change between four valence states V(II)/V(III) and V(IV)/V(V), storing and releasing electrochemical energy. These reactions occur in the conversion unit, which consists of a serial multi-cell assembly called the stack. According to model calculations, the stack holds a share of about 30% of the total system capital costs, while the vanadium electrolyte is responsible for another 40% of the investment.[14] The system costs can be lowered by achieving a higher stack power per active area. The resulting decrease in required stack size for a given amount of power would be a direct materials cost saving.[14,15,16] Another substantial leverage to lower the operational cost is high voltage efficiency, which is reached if the voltage losses during charging and discharging are kept small. Moreover, a reduced loss in charging voltage allows for harvesting more of the electrolyte's specific energy capacity and, therefore, reduces the required amount of vanadium electrolyte.[17]

A higher areal stack power density, a higher voltage efficiency, and a smaller charging voltage loss – all the three cost reduction strategies can be realized by decreasing the stack's total electric resistance, which is composed of the three characteristic partial resistances for ohmic conduction (R_Ω), reactive charge transfer (R_{ct}), and diffusional mass transfer (R_{c}). The three resistances are of the same order of magnitude and depend on the battery design, operation, and material. However, the R_{ct} term is especially dominated by the V^{2+}/V^{3+}-reaction on the graphite electrode surface, which at the same time is most poorly understood.[18,15,16]

The reason for this lack of understanding of R_{ct} is the interplay of several different electrode properties: Decisive for R_{ct} is the electrochemically active surface area (*ECSA*) determined by electrode wettability and electrode roughness.[17,19] Also, surface groups, such as carbon edge sites[20,21,22] and oxygen functionalities,[23,24] are attributed to an enhanced catalytic activity for the V^{2+}/V^{3+}-reaction lowering the R_{ct}. However, none of the properties have been studied separately, so it is still difficult to assign a surface property with its effectiveness for electrode performance. The situation is even more complex as the V^{2+}/V^{3+}-electrode kinetics degrade upon electrode operation, which manifests in a continuously rising R_{ct}, while the VO^{2+}/VO_2^{+}-kinetics are not affected.[25,26,27] To date, no valid explanation for the V^{2+}/V^{3+}-degradation has been found, and its reason is subject of ongoing discussions in the community.

This thesis studies graphite electrodes in order to identify surface properties that are responsible for enhanced electrode kinetics, improving the battery performance. Moreover, a new mechanism is proposed which explains the observed anode kinetics degradation, involving the adsorption of bivalent V(II) that inhibits the V^{2+}/V^{3+}-reaction. The new mechanism is validated with a newly developed test environment for full single-cells enabling stable long-term measurements. Operating strategies are demonstrated that regenerate the degradation and increase the average long-term electrode performance.

2. Vanadium Redox Flow Batteries

This chapter describes the electrochemical and physical fundamentals of vanadium redox flow batteries. Based on these fundamentals, the battery efficiency loss factors are described, the reduction of which is a central objective of this work.

2.1. Functional Principle - From Cell to System

A VRFB represents an electrochemical energy storage device that can take and release electrical energy by temporarily storing it in chemical energy. Based on two redox reactions, two pairs of electrochemically active species are oxidized and reduced at different electrochemical potentials. As an electrochemically active species, vanadium is dissolved in an aqueous sulfuric acid electrolyte. Thereby, vanadium takes on different oxidation states V(II), V(III), V(IV), and V(V), primarily represented by V^{2+}, V^{3+}, $VO^{2+,}$ and VO_2^+. If the battery is fully charged, vanadium is present in the electrolyte only as V^{2+} and VO_2^+. Vice versa, if the battery is fully discharged, the electrolyte contains only vanadium in the form of V^{3+} and VO^{2+}.

Figure 1 shows the schematics of an electrochemical cell comprising two half-cell compartments where the half-cell reactions take place according to

$$V^{2+} \leftrightarrow V^{3+} + e^- \qquad \text{at } E^{00} = -0.26\,V \tag{1}$$

and

$$VO_2{}^+ + 2H^+ + e^- \leftrightarrow VO^{2+} + H_2O \qquad \text{at } E^{00} = +1.00\,V \tag{2}$$

Here, E^{00} represents the standard reduction potential referenced to the standard hydrogen electrode potential (SHE). Within the half-cells, the respective redox reactions of the vanadium species take place at the anode and cathode electrodes that are carbon electrodes in the form of graphite fibers (gray). An ion-exchange membrane separates the two half-cells, allowing ionic charge carriers (red) to cross from one to the other compartment, balancing the overall charge. In Figure 1, the cell is shown while discharging, thus operating as a galvanic cell. Accordingly, in the anodic, i.e., in the electrochemically more negative half-cell (left), the oxidation of V^{2+} (purple) to V^{3+} (green) takes place, following the partial reaction:

$$V^{2+} \rightharpoonup V^{3+} + e^{-} \tag{3}$$

In the cathodic, i.e., in the electrochemically more positive half-cell, VO_2^+ (orange) is simultaneously reduced and reacts to form VO^{2+} (blue), corresponding to the partial reaction:

$$VO_2{}^{+} + 2H^{+} + e^{-} \rightharpoonup VO^{2+} + H_2O \tag{4}$$

During oxidation, V^{2+} releases an electron e^- (yellow) to the anode (gray) (Eq. (3)). The electron flows through the load via the external circuit to the cathode, where it reduces VO_2^+ according to Eq. (4). At the same time, a proton (H^+, red) migrates across the membrane from the anodic to the cathodic half-cell, thus providing charge balance.

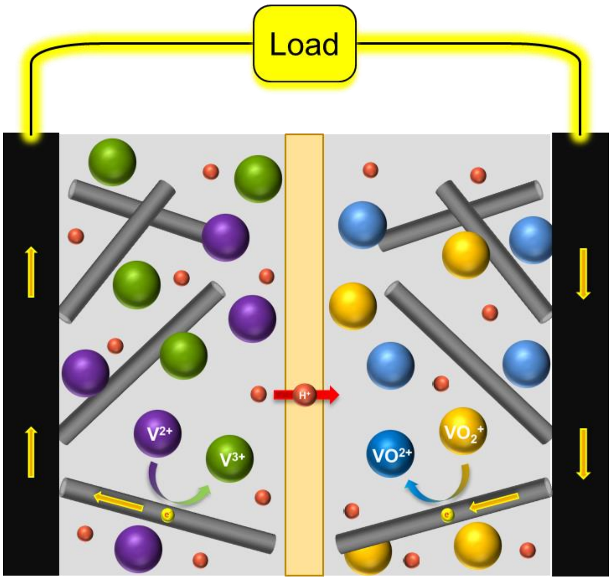

Figure 1: Schematics of a VRFB cell in galvanic operation, i.e., during discharge. The cell consists of two half-cells separated by an ion-exchange membrane. In the anodic half-cell (left), V^{2+} is oxidized to V^{3+}, releasing an electron (yellow) to the anode (gray). The electron flows via the external circuit through the load and to the cathode (right), reducing VO_2^+ to VO^{2+}. Simultaneously, a proton (H^+, red) balances the charge by migrating across the membrane from the anodic to the cathodic half-cell.

Figure 2 shows the flow schematics of a VRFB, comprising a single cell, anolyte and catholyte reservoirs, and the respective pumps needed for electrolyte circulation. Within the single cell, the educt species is partly converted into product species, as indicated by the color scheme. In Figure 2a, the battery is discharging, i.e., operating in galvanic mode.

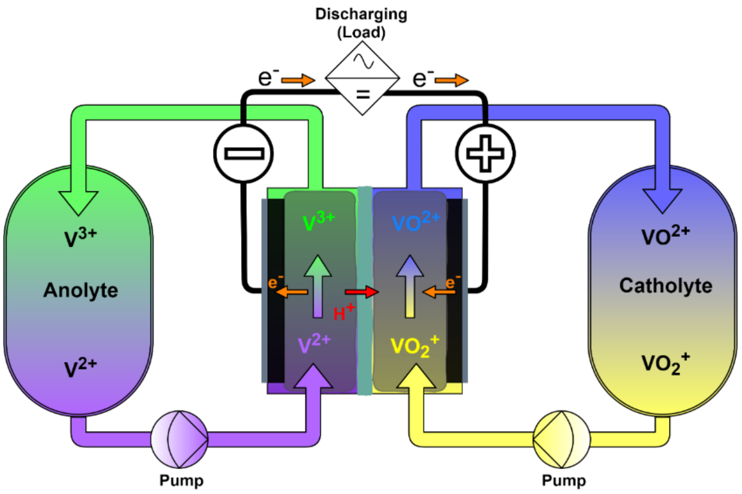

Figure 2: Flow schematics of a VRFB during discharge comprising the converter unit in the form of a single cell as well as the tanks, the pumps, and the external circuit with source or load. Adapted from reference.[28]

Figure 3 expands the design from a single cell towards a stack, being the application-relevant setup of not only one but several cells. Hydraulically, the electrolyte feeds the cells of the stack in parallel, leading to the same pressure drop across the stack compared to a single cell. Electrically, however, the cells are connected in series, leading to a stack voltage being the sum of all cell voltages.

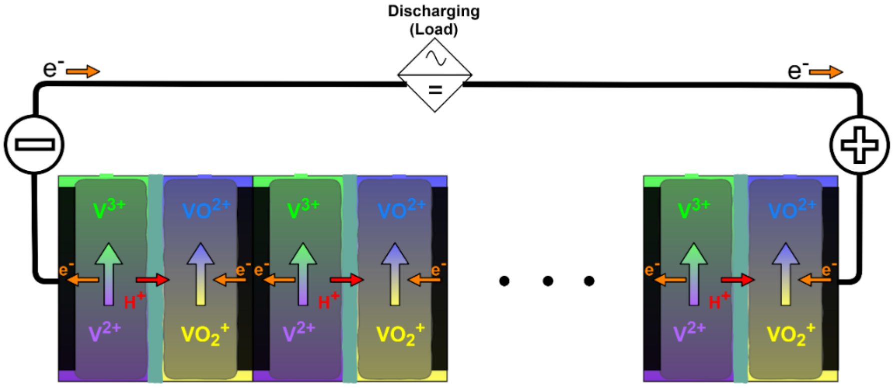

Figure 3: Several single cells electrically connected in series, forming a stack with increased system voltage. Adapted from reference.[28]

2.2. Open Circuit Potentials

If the cell is at open circuit, there is no net current flow across the electrodes, i.e., the redox reactions are at equilibrium. In this case, the potential established at the electrodes is called the open circuit potential (*OCP*). The standard equilibrium potentials E^{00} given in Eq. (1) and (2) are defined for standard electrolyte conditions, i.e., for a temperature of 25°C, a pressure of 1013 mbar, and activities of 1 for protons and the vanadium species. Also, the number of educts equals the one of the products. However, generally, the equilibrium potentials E_0 vary with the electrolyte temperature and with the concentration of redox educts and products, which is described by the Nernst equation

$$E_0 = E^{00} + \frac{RT}{nF} \ln \frac{\prod_i \left(a_i{}^{|\nu_i|}\right)_{\mathrm{ox}}}{\prod_i \left(a_i{}^{|\nu_i|}\right)_{\mathrm{red}}} \tag{5}$$

Here, a_i are the activities of the oxidized and reduced species i, and ν_i are the stoichiometric coefficients according to the respective half-cell redox reactions Eq. (3) and Eq. (4). For these reactions the number of transferred electrons $n = 1$.

Correspondingly, the equilibrium potential at the negative electrode can be expressed by

$$E_{\mathrm{an}}^{0} = E_{\mathrm{an}}^{00} + \frac{RT}{F} \ln \frac{a_{\mathrm{V}^{3+}}}{a_{\mathrm{V}^{2+}}} \tag{6}$$

and the equilibrium potential at the positive electrode is

$$E_{\mathrm{cat}}^{0} = E_{\mathrm{cat}}^{00} + \frac{RT}{F} \ln \frac{a_{\mathrm{VO}_2^+} \left(a_{\mathrm{cat,H}^+}\right)^2}{a_{\mathrm{VO}^{2+}}} \tag{7}$$

The term $\left(a_{\mathrm{cat,H}^+}\right)^2$ comprises the proton activity in the catholyte and accounts for the two moles protons H^+ evolving in the catholyte upon the oxidation of one mole VO^{2+} corresponding to Eq. (4).

Generally, the activities a_i for each species i can be expressed by

$$a_i = \gamma_i \cdot \frac{c_i}{c_{i,0}} \tag{8}$$

Here, $c_{i,0}$ is the standard concentration for a given species (usually 1 $\mathrm{mol/kg_{solvent}}$ or 1 $\mathrm{mol/l_{solvent}}$). An additional activity coefficient γ_i for each species i accounts for the fact that each ion is surrounded by counter ions building the solvation shell, shielding the ion in the center. For highly dilute ideal solutions, the center ions find not enough counter ions to build a solvation shell and the activities a_i equal the concentrations c_i with $\gamma_i = 1$. For dilute solutions with concentrations < 10 mM, the activity coefficients γ_i can be approximated using the Debye-Hückel limiting law.[29] At higher concentrations > 10 mM, applicable for the technical vanadium electrolytes containing vanadium and sulfuric acid at concentrations > 1 M, the approximation is no longer valid, and γ_i has to be derived from experimental data. As a simplification, the activity coefficients can be extracted from the logarithmic terms, combined, and expressed as an additive, yet concentration-dependent term Γ:

$$\frac{RT}{F}\ln\prod_i (a_i)^{\nu_i} = \frac{RT}{F}\ln\prod_i (\gamma_i \cdot \frac{c_i}{c_{i,0}})^{\nu_i} = \Gamma + \frac{RT}{F}\ln\prod_i \left(\frac{c_i}{c_{i,0}}\right)^{\nu_i} \tag{9}$$

with

$$\Gamma = \frac{RT}{F}\ln\prod_i (\gamma_i)^{\nu_i} \tag{10}$$

Applying Eq. (8)-(10) to Eq. (6) and Eq. (7), the electrode potentials E^0_{an} and E^0_{cat} are a function of the partial concentrations of V^{2+} and VO_2^+:

$$E^0_{\mathrm{an}} = E^{00}_{\mathrm{an}} + \Gamma_{\mathrm{V^{2+},V^{3+}}} + \frac{RT}{F}\ln\frac{c_{\mathrm{V^{3+}}}/c_{\mathrm{V^{3+},0}}}{c_{\mathrm{V^{2+}}}/c_{\mathrm{V^{2+},0}}} \tag{11}$$

and

$$E^0_{\mathrm{cat}} = E^{00}_{\mathrm{cat}} + \Gamma_{\mathrm{VO^{2+},VO_2^+,H^+}} + \frac{RT}{F}\ln\frac{c_{\mathrm{VO_2^+}}/c_{\mathrm{VO_2^+,0}}\left[c_{\mathrm{cat,H^+}}/c_{\mathrm{cat,H^+,0}}\right]^2}{c_{\mathrm{VO^{2+}}}/c_{\mathrm{VO^{2+},0}}} \tag{12}$$

For the case of an electrolyte containing a total vanadium concentration of $c^0_{\mathrm{V,tot}} = 1.6$ M (based on 0.8 M V^{3+} and 0.8 M VO^{2+}) dissolved in 2.0 M aqueous sulfuric acid, the concentrations of $c_{\mathrm{cat,H^+}}$ and $c_{\mathrm{an,H^+}}$ calculate as follows: In the as-received state of the electrolyte, i.e., before charging, its state-of-charge (*SoC*) corresponds to an *SoC* -50% by definition. The somewhat unintuitive term *SoC* -50% derives from the fact that 50% of the theoretical energy capacity are needed to charge the electrolyte to an *SoC* 0%. At this *SoC* -50%, the resulting proton concentration $c_{\mathrm{H^+}}^{SoC-50\%}$ of the uncharged electrolyte is approximately 2.6 M. This number accounts for the first complete dissociation stage of 2.0 M H_2SO_4 into 2.0 M H^+ and 2.0 M HSO_4^+, and the second incomplete dissociation stage of HSO_4^+ by 30% into 0.6 M H^+ and 0.6 M SO_4^{2-}.[30] Initially, the uncharged electrolyte corresponds to the oxidation state of $V^{3.5+}$, meaning it contains equal shares of 0.8 M V^{3+} and 0.8 M VO^{2+}, respectively. Until charging to *SoC* 0%, two protons will evolve in the catholyte per each oxidized V^{3+} ($V^{3+} + H_2O \rightarrow VO^{2+} + 2H^+ + e^-$), and two protons will be consumed in the anolyte per reduced VO^{2+} ($VO^{2+} + 2H^+ + e^- \rightarrow V^{3+} + H_2O$). At the same time, for each V^{3+} oxidized in the catholyte, a proton migrates from catholyte to anolyte across the membrane for charge balancing. The resulting proton concentrations at *SoC* 0% (i.e., when all V^{3+} in the catholyte is oxidized to VO^{2+} and all VO^{2+} in the anolyte is reduced to V^{3+}) calculate to

$$c_{\mathrm{cat,H^+}}^{\mathrm{SoC\ 0\%}} = 2.6\ \mathrm{M} + 2 \cdot 0.8\ \mathrm{M} - 0.8\ \mathrm{M} = 3.4\ \mathrm{M} \tag{13}$$

$$c_{\mathrm{an,H^+}}^{\mathrm{SoC\ 0\%}} = 2.6\ \mathrm{M} - 2 \cdot 0.8\ \mathrm{M} + 0.8\ \mathrm{M} = 1.8\ \mathrm{M} \tag{14}$$

Upon further charging, for each VO^{2+} oxidized to VO_2^+ in the catholyte, two protons evolve. Also, one of those protons migrates across the membrane into the anolyte. Consequently, the overall proton concentration in catholyte and anolyte is described by

$$c_{\mathrm{cat,H^+}} = c_{\mathrm{cat,H^+}}^{\mathrm{SoC\ 0\%}} + SoC \cdot 1.6\ \mathrm{M} = 3.4\ \mathrm{M} + SoC \cdot 1.6\ \mathrm{M} \tag{15}$$

$$c_{\mathrm{an,H^+}} = c_{\mathrm{an,H^+}}^{\mathrm{SoC\ 0\%}} + SoC \cdot 1.6\ \mathrm{M} = 1.8\ \mathrm{M} + SoC \cdot 1.6\ \mathrm{M} \tag{16}$$

The reference proton concentration $c_{\mathrm{cat,H^+,0}}$ in the catholyte is defined for the proton concentration at *SoC* 50%, i.e., $c_{\mathrm{cat,H^+}}^{\mathrm{SoC\ 50\%}} = 4.2$ M. Accordingly, $c_{\mathrm{an,H^+,0}}$ in the anolyte is $c_{\mathrm{an,H^+}}^{\mathrm{SoC\ 50\%}} = 2.6$ M.

Moreover, the partial vanadium concentrations and also the *SoC* are correlated by

$$\frac{c_{\mathrm{V^{2+}}}}{c_{\mathrm{V,tot}}} = 1 - \frac{c_{\mathrm{V^{3+}}}}{c_{\mathrm{V,tot}}} = SoC = 1 - \frac{c_{\mathrm{VO^{2+}}}}{c_{\mathrm{V,tot}}} = \frac{c_{\mathrm{VO_2^+}}}{c_{\mathrm{V,tot}}} \tag{17}$$

Here, $c_{\mathrm{V,tot}}$ is the total electrolyte vanadium concentration being 1.6 M.

Combining Eq. (13)-(17) into Eq. (11)-(12), Figure 4 represents the electrode potentials E_{an}^0 and E_{cat}^0 for partial concentrations of V^{2+} and VO_2^+ in the range of 0-100%, while assuming all activity coefficients $\gamma_i = 1$, or $\Gamma_{\mathrm{V^{2+},V^{3+}}} = \Gamma_{\mathrm{VO^{2+},VO_2^+,H^+}} = 0$.

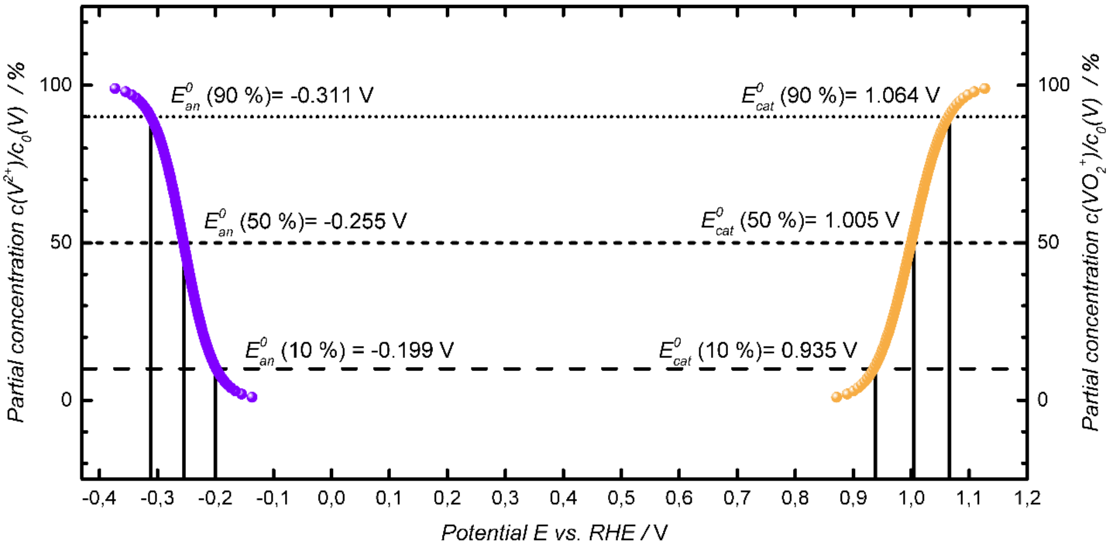

Figure 4: Equilibrium electrode potentials $E_{0,an}$ and $E_{0,cat}$ for partial concentrations of V^{2+} and VO_2^+ in the range of 0-100%.

2.3. Open Circuit Voltage

The cell voltage is described by the difference of the two electrode potentials together with the Donnan potential forming across the membrane and owing to the different proton concentrations in anolyte and catholyte.[31,29]

$$OCV = E^0_{\text{cat}} - E^0_{\text{an}} + E_{Donnan} \tag{18}$$

Thereby, the Donnan potential is determined by

$$E_{Donnan} = \frac{RT}{F}\ln\frac{a_{cat,H^+}}{a_{an,H^+}} \tag{19}$$

With Eq. (11), (12), and (19), the *OCV* is described by

$$OCV = E^{00}_{\text{cat}} - E^{00}_{\text{an}} + \Gamma_{\text{V}^{2+},\text{V}^{3+},\text{VO}^{2+},\text{VO}_2^+,\text{H}^+} + \frac{RT}{F}\ln\left\{\frac{c_{\text{VO}_2^+}/c_{\text{VO}_2^+,0}\left[c_{\text{cat,H}^+}/c_{\text{cat,H}^+,0}\right]^2}{c_{\text{VO}^{2+}}/c_{\text{VO}^{2+},0}}\cdot\frac{c_{\text{V}^{2+}}/c_{\text{V}^{2+},0}}{c_{\text{V}^{3+}}/c_{\text{V}^{3+},0}}\cdot\frac{c_{\text{cat,H}^+}/c_{\text{cat,H}^+,0}}{c_{\text{an,H}^+}/c_{\text{an,H}^+,0}}\right\} \tag{20}$$

The reference concentrations $c_{\mathrm{VO}_2^+,0}$, $c_{\mathrm{VO}^{2+},0}$, $c_{\mathrm{V}^{3+},0}$, and $c_{\mathrm{V}^{2+},0}$ all equal 0.8 M and vanish. Substituting Eq. (17), (15), and (16) into Eq. (20) delivers an expression of the *OCV* vs. the *SoC*:

$$OCV = 1.255\ \mathrm{V} + \Gamma_{\mathrm{V}^{2+},\mathrm{V}^{3+},\mathrm{VO}^{2+},\mathrm{VO}_2^+,\mathrm{H}^+} + 25.7\ \frac{\mathrm{mV}}{\mathrm{s}} \ln\left\{\left[\frac{SoC}{1-SoC}\cdot\frac{(3.4\ \mathrm{M}+SoC\cdot 1.6\ \mathrm{M})}{4.2\ \mathrm{M}}\right]^2 \cdot \frac{(3.4\ \mathrm{M}+SoC\cdot 1.6\ \mathrm{M})/4.2\ \mathrm{M}}{(1.8\ \mathrm{M}+SoC\cdot 1.6\ \mathrm{M})/2.6\ \mathrm{M}}\right\} \tag{21}$$

In Eq. (21), the activity coefficients γ_i that constitute $\Gamma_{\mathrm{V}^{2+},\mathrm{V}^{3+},\mathrm{VO}^{2+},\mathrm{VO}_2^+,\mathrm{H}^+}$ are a function of the concentrations c_i. However, by assuming all γ_i to be constant over the entire *SoC* range, curve fitting based on Eq. (21) revealed that a constant $\Gamma_{\mathrm{V}^{2+},\mathrm{V}^{3+},\mathrm{VO}^{2+},\mathrm{VO}_2^+,\mathrm{H}^+} = 0.158\ \mathrm{V}$ provides very good agreement with experimental data for the *OCV* versus *SoC* (using precise coulometric charge counting).[32] Knowledge of the *OCV* vs. *SoC* values thus offers the ability to assign a measured *OCV* to a precise *SoC* value, as sketched in Figure 5.

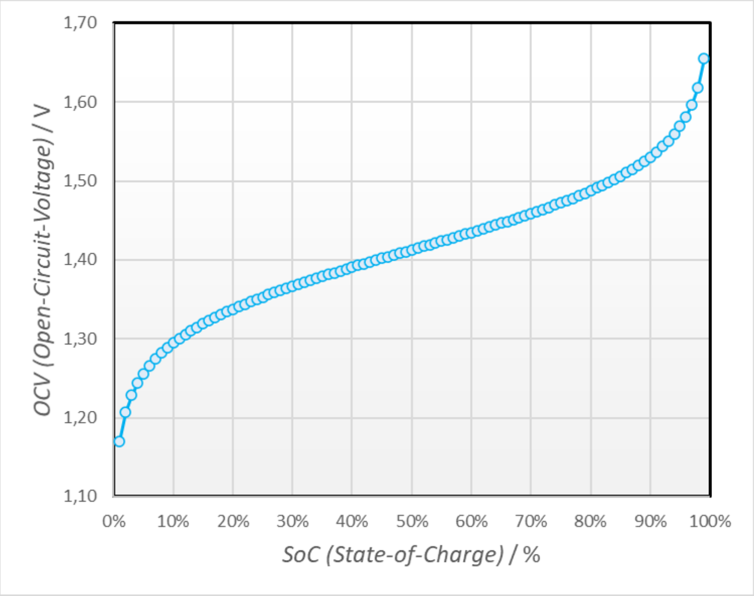

Figure 5: Open-circuit-voltage (*OCV*) vs. state-of-charge (*SoC*) for a total vanadium concentration of 1.6 M in 2.0 M H_2SO_4 (aq.) electrolyte at 25°C, calculated from Eq. (21) using $\Gamma_{\mathrm{V}^{2+},\mathrm{V}^{3+},\mathrm{VO}^{2+},\mathrm{VO}_2^+,\mathrm{H}^+} = 0.158\ V$. Reproduced with permission from supporting information of reference.[33]

2.4. Voltage Loss Factors

The terminal voltage of the battery deviates from the equilibrium voltage as soon as current flows across the closed circuit. In order to ensure the current flow, various conduction, charge transfer, and mass transport processes must take place in the cell. These processes each result in voltage losses that reduce the dischargeable energy.

At open circuit, an equilibrium potential forms at the two electrodes (c.f., Section 2.2). At the anode, the equilibrium potential results from equal rates of V^{2+} oxidation to V^{3+} (Eq. (3)) and V^{3+} reduction to V^{2+}. The same applies to the cathode, where VO^{2+} and VO_2^+ get oxidized and reduced, respectively at equal rates (see Eq. (4)). The mutually compensating, area-specific current densities of oxidation and reduction at an electrode is called exchange current density i_0 and is defined for the anode as[34]

$$i_0 = nFk_0\left(c^0_{V^{2+}}\right)^{\alpha}\left(c^0_{V^{3+}}\right)^{1-\alpha} \tag{22}$$

In Eq. (22), n is the number of electrons transferred per reaction ($n = 1$), F is the Avogadro constant (96485 C mol^{-1}), k_0 is the standard rate constant of the reaction (cm s^{-1}), α is the charge-transfer coefficient, and $c^0_{V^{2+}}$ and $c^0_{V^{3+}}$ are the V^{2+} and V^{3+} concentrations in the bulk electrolyte (mol L^{-1}).

2.4.1. Reactive Charge Transfer

At closed circuit, V^{2+} oxidizes to V^{3+} at the anode, and VO_2^+ reduces to VO^{2+} at the cathode. Figure 6 (right panel) illustrates this process of charge transfer for the V^{2+}/V^{3+}-reaction. Correspondingly, V^{2+} adsorbs at the surface of the graphite fiber electrode (state 1 to 2), releases an electron there, and transforms into V^{3+} (state 2 to 3). Subsequently, V^{3+} desorbs from the surface (state 3 to 4).

The kinetic current (i_{kin}) is generally a function of the kinetic overpotential (η_{kin}), which is the difference of the electrode potential under load and the equilibrium potential. This relation is commonly described by the Butler-Volmer equation:

$$i_{\mathrm{kin}} = i_0\left(e^{\frac{\alpha F\eta_{\mathrm{kin}}}{RT}} - e^{\frac{-(1-\alpha)F\eta_{\mathrm{kin}}}{RT}}\right) \tag{23}$$

Here, R is the ideal gas constant (8.314 J mol^{-1} K^{-1}), and T is the electrolyte temperature (in K). The left panel of Figure 6 represents the characteristic course of $i_{\mathrm{kin}}\ vs.\ \eta_{\mathrm{kin}}$ according to Eq. (23), with an exchange current density of $i_0 = 0.257\ \mathrm{mA\ cm^{-2}}$, a charge-transfer coefficient of $\alpha = 0.5$, and a temperature of $T = 298.15\ \mathrm{K}$. The equilibrium potential was chosen as $E_{an}^0 = -0.255\,\mathrm{V}$, which, referring to Figure 4, corresponds to equal amounts of V^{2+} and V^{3+} present in the electrolyte.

For small η ($\eta \approx 0$), the exponential terms in Eq. (23) can be approximated by $\exp(x) = 1 + x$, which simplifies Eq. (23) to its linear form:

$$i_{\mathrm{kin}} = i_0 \frac{F\eta_{\mathrm{kin}}}{RT} = \frac{\eta_{\mathrm{kin}}}{R_{\mathrm{ct}}} \tag{24}$$

R_{ct} is the charge-transfer resistance, a characteristic measure for the kinetics of the electrode.

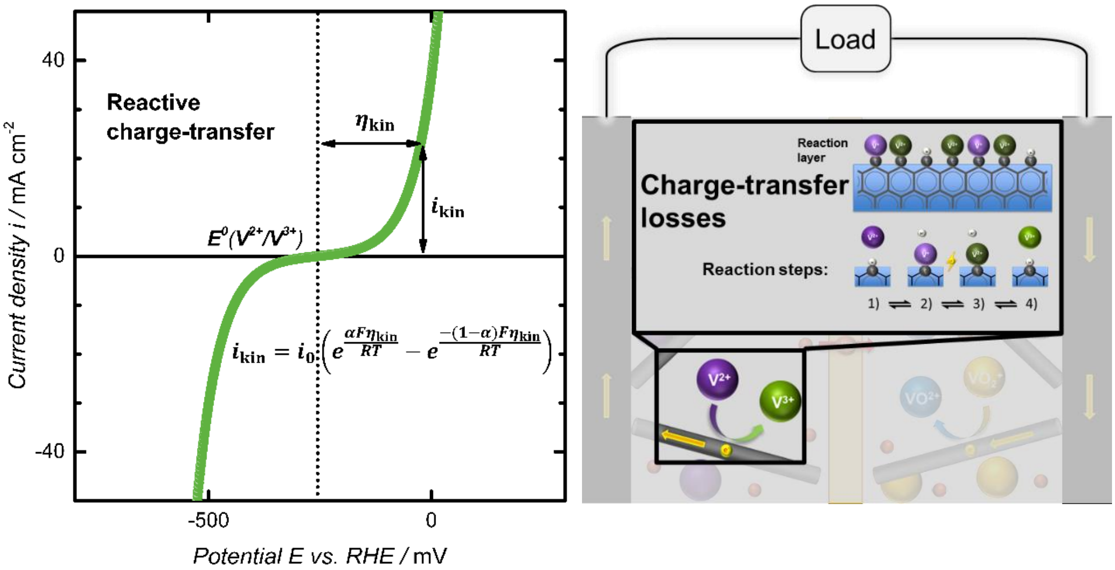

Figure 6: Potential losses upon charge transfer at the electrode surface described by the Butler-Volmer equation (left panel) with an exchange current density of $i_0 = 0.257\ \mathrm{mA\ cm^{-2}}$ (corresponding to $R_{\mathrm{ct}} = 100\ \Omega\ \mathrm{cm^2}$), a charge-transfer coefficient of $\alpha = 0.5$, and a temperature of $T = 298.15\ \mathrm{K}$. Exemplarily shown in the right panel is the situation on the surface of the anode graphite fibers employing the catalytically active surface area for the V^{2+}/V^{3+}-reaction.

2.4.2. Diffusive Mass Transport

When a current is being drawn, the reactant is continuously consumed at the surface of the electrode, so the reactant concentration on the electrode surface is lower than in the bulk electrolyte, while the product concentration is higher than that in the bulk. In case of the V^{2+}/V^{3+} anode, this means that the surface concentrations of V^{2+} and V^{3+} ($c_{V^{2+}}^s$ and $c_{V^{3+}}^s$) differ from their bulk concentrations ($c_{V^{2+}}^0$ and $c_{V^{3+}}^0$). The Butler-Volmer equation accounts for this situation by its extended form:

$$i = i_0 \left(\frac{c^s_{V^{2+}}}{c^0_{V^{2+}}} e^{\frac{\alpha F \eta}{RT}} - \frac{c^s_{V^{3+}}}{c^0_{V^{3+}}} e^{\frac{-(1-\alpha)F\eta}{RT}} \right) \tag{25}$$

Considering the V^{2+}/V^{3+} anode during discharge (i.e., $\eta = E_{\text{an}} - E^0_{\text{an}} > 0$), the reactant concentration at the surface will decrease so that $c^s_{V^{2+}} < c^0_{V^{2+}}$. This situation is shown in the right panel of Figure 7. The reactant depletes at the surface, and a concentration gradient is formed from bulk electrolyte to the surface, which extends across the Nernst diffusion layer with a thickness δ_N. To compensate for the reactant depletion at the surface, reactant from the bulk electrolyte must pass across the thickness of the Nernst layer via diffusive mass transport, which imposes additional concentration overpotential losses (η_c) that can be estimated as follows. For $\eta \gg 0$, the influence of the negative exponential term in Eq. (23) can be neglected, yielding

$$i \cong i^+ = i_0 \frac{c^s_{V^{2+}}}{c^0_{V^{2+}}} e^{\frac{\alpha F \eta}{RT}} \tag{26}$$

An expression for $c^s_{V^{2+}}/c^0_{V^{2+}}$ is obtained by considering the concentrations that occur at the electrode surface during continuous mass transport. According to Fick's first law, the following applies to the mass flow reaching the surface via diffusion in a one-dimensional case (e.g., large planar electrodes separated by a short distance)

$$i = nFD \left(\frac{\partial c}{\partial x} \right)_{x=0} = FD \frac{c^0_{V^{2+}} - c^s_{V^{2+}}}{\delta_N} \tag{27}$$

Here, D is the diffusion coefficient of V^{2+} and transport by migration is neglected. In the mass transport limited case, the V^{2+} concentration at the electrode surface becomes zero, i.e., $c^s_{V^{2+}} = 0$, so that the diffusion-limited current i_{lim} can be described by

$$i_{\text{lim}} = FD \left(\frac{c^0_{V^{2+}}}{\delta_{\text{N}}} \right) \tag{28}$$

Dividing Eq. (27) by (28) gives

$$\frac{i}{i_{lim}} = 1 - \frac{c^s_{V^{2+}}}{c^0_{V^{2+}}} \tag{29}$$

Moreover, approximating Eq. (23) for $\eta \gg 0$ delivers

$$i_{\text{kin}} \cong i^+_{\text{kin}} = i_0 e^{\frac{\alpha F \eta_{\text{kin}}}{RT}} \tag{30}$$

Dividing Eq. (26) by Eq. (30) and combining with Eq. (29) leads to

$$\frac{i}{i_{\mathrm{kin}}} = \frac{c^{s}_{V^{2+}}}{c^{0}_{V^{2+}}} = 1 - \frac{i}{i_{\mathrm{lim}}} \tag{31}$$

In practice, the current i is measured, so resolving Eq. (31) can yield i_{kin}, which is also known from the Koutecky-Levich compensation.[35] However, here, we derive an expression for the measured, Koutecky-Levich uncompensated current

$$i = \frac{i_{\mathrm{kin}} \cdot i_{\mathrm{lim}}}{i_{\mathrm{kin}} + i_{\mathrm{lim}}} \tag{32}$$

The diffusive mass transport limits the kinetic current according to Eq. (32) and contributes to the effective electrode potential. Solving Eq. (26) for η yields

$$\eta = \frac{RT}{\alpha F}\left[\ln\left(\frac{i}{i_0}\right) - \ln\left(\frac{c^{s}_{V^{2+}}}{c^{0}_{V^{2+}}}\right)\right] \tag{33}$$

With interpreting Eq. (33) as $\eta = \eta_{\mathrm{kin}} + \eta_{\mathrm{c}}$ and substituting Eq. (29), the concentration overpotential (η_c) is

$$\eta_{\mathrm{c}} = -\frac{RT}{\alpha F}\ln\left(1 - \frac{i}{i_{\mathrm{lim}}}\right) \tag{34}$$

For illustration, the left panel of Figure 7 draws the current i from Eq. (32) vs. η_{c} from Eq. (34). The limiting current was chosen as $i_{\mathrm{lim}} = 40\ \mathrm{mA\ cm^{-2}}$.

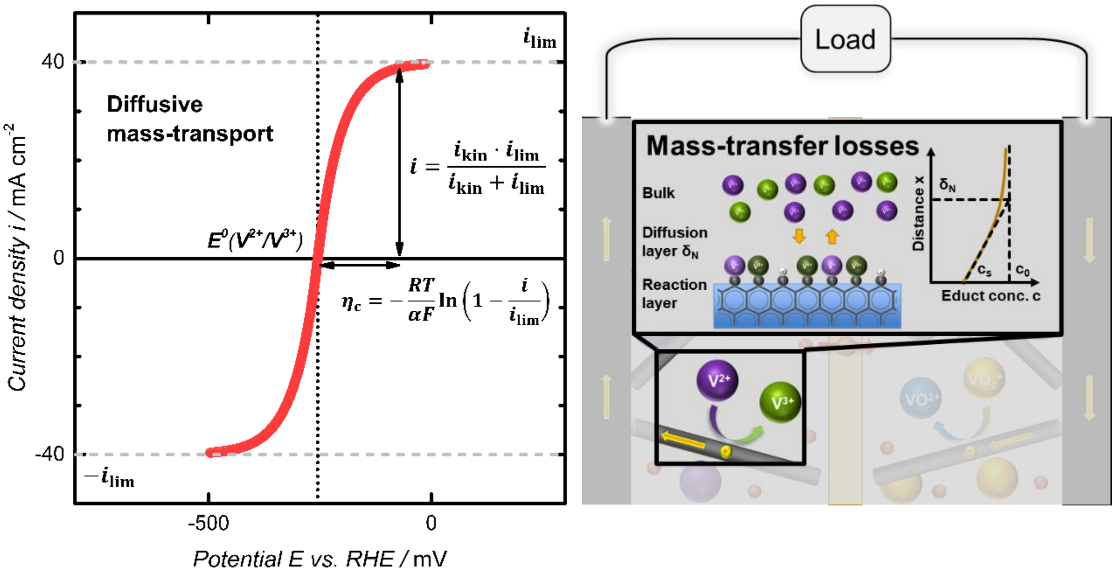

Figure 7: Koutecky-Levich uncompensated current i from Eq. (32) vs. concentration overpotential losses η_{c} from Eq. (34) using a limiting current of $i_{\mathrm{lim}} = 40\ \mathrm{mA\ cm^{-2}}$, an equilibrium potential of $E^0_{an} = -0.255\ \mathrm{V}$, a charge-transfer coefficient of $\alpha = 0.5$, and a temperature of $T = 298.15\ \mathrm{K}$ (left panel). The

right panel shows the situation of a constant rate of reaction. V^{2+}/V^{3+}-reactants transfer by diffusive mass transport across the Nernstian diffusion layer with thickness δ_N from the bulk electrolyte to the graphite fiber electrode surface. Under electrolyte flux due to forced convection, a constant diffusion layer thickness formed, which depends on the reaction rate and on the educt concentration on the electrode surface.

2.4.3. Ohmic Resistances

Electronically conductive components in serial contact provide the current flow of the electrons released and received by the redox reactants. When discharging, the electrons start from an oxidation site on the anode fiber surface and flow through the fiber into the bipolar plates, the current collectors, and the external circuit. They then re-enter the battery and flow through the same components on the cathode side in reverse order to finally reach a reduction site. To counteract this directional flow of electrons and ensure electroneutrality, ions, in turn, migrate across the anion or cation exchange membrane. In the right panel of Figure 8, protons migrate across the here shown cation exchange membrane. It may be noted that the direction depends on whether an anion or a cation exchange membrane is used. The electronic as well as the ionic transport is subject to area-specific conduction resistances R_{el} and R_{ion}, which add up according to their serial connection and, for a current density i, lead to the ohmic potential drop η_{Ω}:

$$\eta_{\Omega} = i \cdot R_{\Omega} = i \cdot (R_{\mathrm{el}} + R_{\mathrm{ion}}) \tag{35}$$

The left panel of Figure 8 demonstrates the linear character of the resulting potential losses according to the electronic and ionic conduction resistances, which are assumed by $R_{\Omega} = 2\ \Omega\ \mathrm{cm}^2$.

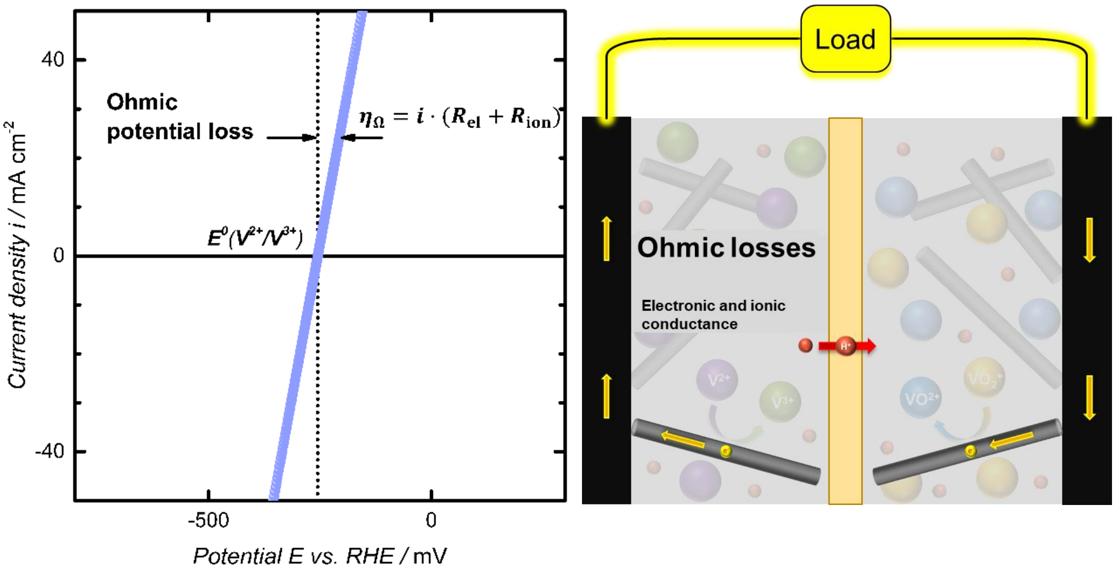

Figure 8: Potential losses caused by ohmic electronic and ionic conduction resistances (assumed to be $R_\Omega = 2\ \Omega\ \mathrm{cm}^2$) at an anode equilibrium potential of $E^0_{an} = -0.255$ V. The right panel shows the situation during discharging, when the electrons (yellow) flow from the anode through the external load to the cathode side of the battery. On their way, the electrons face a serial connection of conducting components such as the graphite electrode fibers, the bipolar plates, the current collectors, and the outer wiring. At the same time, ions such as H^+ (red) migrate through the electrolyte and across the membrane from the anode to the cathode side, balancing the charge brought about by the transferred electrons and ensuring electroneutrality. The ionic and electronic conduction resistances lead to ohmic potential losses.

2.4.4. Voltage Loss Factors Combined

Figure 9 summarizes the three characteristic voltage loss terms illustrated for the V^{2+}/V^{3+} electrode, namely ohmic losses, charge transfer overpotentials, and concentration overpotentials. The plot shows 1) the Koutecky-Levich-uncompensated current i (Eq. (32)) vs. the ohmic overpotential η_Ω (Eq. (35)) (blue curve), 2) the kinetic current i_{kin} vs. the kinetic (Eq. (23)) plus the ohmic (Eq. (35)) overpotential $\eta_{\mathrm{kin}} + \eta_\Omega$ (green curve), and 3) the Koutecky-Levich-uncompensated current i (Eq. (32)) vs. the kinetic (Eq. (23)) plus the ohmic (Eq. (35)) plus the concentration (Eq. (34)) overpotential $\eta_{\mathrm{kin}} + \eta_\Omega + \eta_{\mathrm{c}}$ (red curve).

As can be seen, the Koutecky-Levich-uncompensated current i (resulting from the kinetic and the limiting current) combined with the characteristic overpotentials leads to the typical sigmoidal wave-form of current vs. potential. This waveform can be measured at rotating disk electrodes under controlled electrolyte conditions, such as a defined temperature and mass transport towards the electrode. This measurement technique was central to the results of this thesis and is described in detail in Section 3.2.

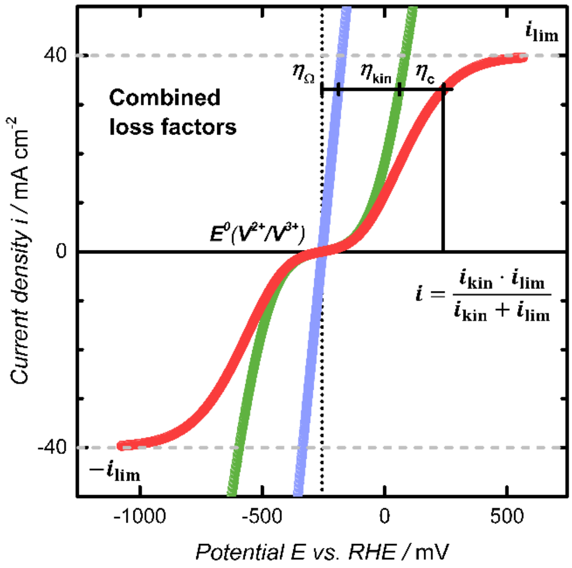

Figure 9: Modelled current vs. electrode potential representing the combined characteristic loss factors in a cumulative manner: 1) ohmic potential losses η_Ω (blue curve) (resulting from $R_\Omega = 2\ \Omega\ \mathrm{cm}^2$), 2) charge-transfer potential losses η_{kin} (green curve) (resulting from an exchange current density of $i_0 = 0.257\ \mathrm{mA\ cm}^{-2}$ corresponding to $R_{\mathrm{ct}} = 100\ \Omega\ \mathrm{cm}^2$), and 3) concentration potential losses η_{c} (red curve) with a limiting current of $i_{\mathrm{lim}} = 40\ \mathrm{mA\ cm}^{-2}$. For the calculations, a charge-transfer coefficient of $\alpha = 0.5$, a temperature of $T = 298.15$ K, and an anode equilibrium potential of $E^0_{an} = -0.255$ V was used. Note that the red curve represents the course of the current i vs. the sum of the potential losses $\eta_\Omega + \eta_{\mathrm{ct}} + \eta_{\mathrm{c}}$.

2.5. Current vs. Potential Relationships at 50% *SoC*

Figure 10 shows the modeled current-potential curves of both VRFB electrodes, namely for the V^{2+}/V^{3+}-reaction and the $VO^{2+}/VO_2{}^+$-reaction. As in the previous considerations, the equilibrium potentials $E^0_{\mathrm{an}} = -0.255$ V and $E^0_{\mathrm{cat}} = 1.011$ V used here represent equal V^{2+} and V^{3+} concentrations of 0.8 M in the anolyte and VO^{2+} and $VO_2{}^+$ in the catholyte, referring to an *SoC* of 50% (c.f., Figure 4). For simplicity, the same absolute limiting currents of $\pm 40\ \mathrm{mA\ cm}^{-2}$ were used. However, the model calculation is done with a tenfold higher i_0 for the $VO^{2+}/VO_2{}^+$-reaction, which is closer to reality and causes the anode and cathode curves to differ. Consequently, the extent of the respective loss factors contributing to the overpotentials varies for a given current density. For example, the faster VO^{2+}/VO_2^+-reaction kinetics result in a lower kinetic overpotential at the cathode than at the anode.

Interestingly, the three loss factors contribute differently to the total overpotential depending on the current density. While, according to Eq. (35), the ohmic overpotential increases linearly with the current density, the kinetic overpotential as described by Eq. (30) increases only logarithmically with the current density according to

$$\eta_{\mathrm{kin}} = \frac{RT}{\alpha F} \ln\left(\frac{i_{\mathrm{kin}}^{+}}{i_0}\right) \tag{36}$$

The concentration overpotential, on the other hand, described by Eq. (34), increases significantly as the effective current i approaches the limiting current i_{lim}.

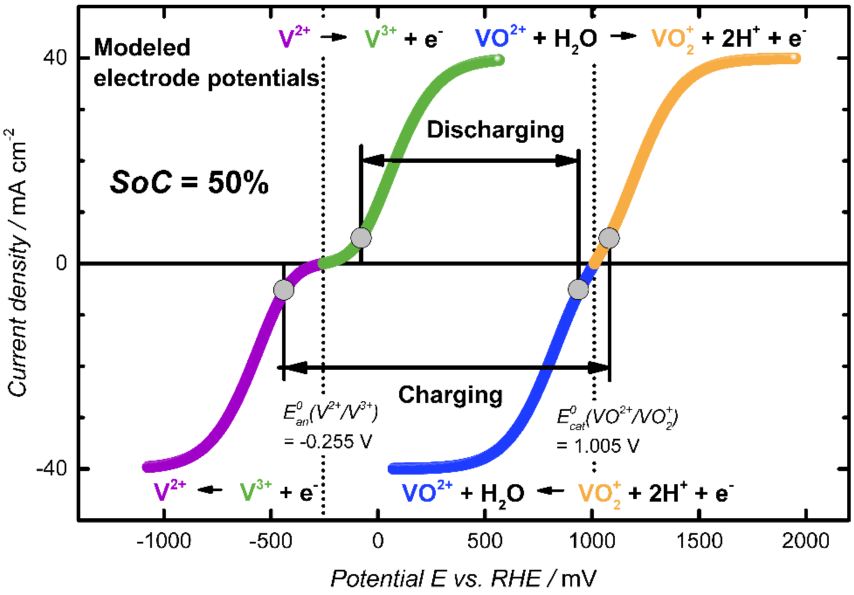

Figure 10: Modeled current vs. anode and cathode potential of a VRFB at an *SoC* of 50%, demonstrating the potential difference during charging and discharging, which strongly depends on the current density. The charge and discharge potentials at an absolute current density of 5 mA cm^{-2} are marked by the black horizontal arrows. The relevant parameters that were used to construct these curves are $c_{\mathrm{V}^{2+}} = c_{\mathrm{V}^{3+}} = c_{\mathrm{VO}^{2+}} = c_{\mathrm{VO_2}^+} = 0.8\ \mathrm{M}$, $R_{\Omega,\mathrm{an}} = 2\ \Omega\ \mathrm{cm}^2$, $R_{\Omega,\mathrm{cat}} = 2\ \Omega\ \mathrm{cm}^2$, $R_{\mathrm{ct,an}} = 100\ \Omega\ \mathrm{cm}^2$, $R_{\mathrm{ct,cat}} = 10\ \Omega\ \mathrm{cm}^2$, $i_{\mathrm{lim}} = \pm 40\ \mathrm{mA\ cm}^{-2}$, $\alpha = 0.5$, $T = 298.15\ \mathrm{K}$, $E^0_{\mathrm{an}} = -0.255\ \mathrm{V}$, and $E^0_{\mathrm{cat}} = 1.011\ \mathrm{V}$.

2.6. Current vs. Potential Relationships at 10% *SoC*

While the above current-potential curves are shown for an *SoC* 50%, the *SoC* of the battery has a significant influence on the contributions of the various overpotential terms.

During charging and discharging the battery, the electrolyte composition changes continuously, especially concerning the reactant concentrations of V^{2+} and V^{3+} in the anolyte and VO^{2+} and VO_2^+ in the catholyte.

Assuming an *SoC* of 10%, the current vs. anode and cathode potentials are displayed in Figure 11. At the lower *SoC*, the exchange current density, according to Eq. (22), changes as follows:

$$i_0|_{SoC\ 10\%} = \frac{\left(c_{V^{2+}}^{SoC\ 10\%}\right)^{\alpha}\left(c_{V^{3+}}^{SoC\ 10\%}\right)^{1-\alpha}}{\left(c_{V^{2+}}^{SoC\ 50\%}\right)^{\alpha}\left(c_{V^{3+}}^{SoC\ 50\%}\right)^{1-\alpha}} \cdot i_0|_{SoC\ 50\%} = 0.6 \cdot i_0|_{SoC\ 50\%} \tag{37}$$

with $c_{V^{2+}}^{SoC\ 50\%} = c_{V^{3+}}^{SoC\ 50\%} = 50\%\ \cdot 1.6\ \mathrm{M} = 0.8\ \mathrm{M}$, $c_{V^{2+}}^{SoC\ 10\%} = 10\% \cdot 1.6\ \mathrm{M} = 0.32\ \mathrm{M}$, $c_{V^{3+}}^{SoC\ 10\%} = 90\% \cdot 1.6\ \mathrm{M} = 1.44\ \mathrm{M}$, and $\alpha = 0.5$.

The concentration overvoltage also changes, since the lower reactant concentration reduces the limiting current during discharge ($i_{\mathrm{lim,dc}}$) and increases the limiting current during charge ($i_{\mathrm{lim,ch}}$). Given by Eq. (28), i_{lim} changes for the discharge case at *SoC* 10% according to

$$i_{\mathrm{lim,dc}}|_{SoC\ 10\%} = \frac{c_{V^{2+}}^{SoC\ 10\%}}{c_{V^{2+}}^{SoC\ 50\%}} \cdot i_{\mathrm{lim}}|_{SoC\ 50\%} = 0.2 \cdot i_{\mathrm{lim,dc}}|_{SoC\ 50\%} \tag{38}$$

The limiting current in this example would be only 8 mA cm^{-2} instead of $40\ \mathrm{mA\ cm}^{-2}$. As a result, according to Eq. (34), the concentration overpotential increases from $\eta_{\mathrm{c}}|_{SoC\ 50\%} = 7$ mV to $\eta_{\mathrm{c}}|_{SoC\ 10\%} = 50$ mV for a discharge current (i_{dc}) of 5 mA cm^{-2}.

At the same time, the equilibrium potentials of the two electrodes approach each other, so that the usable cell voltage is also reduced (c.f., Figure 4).

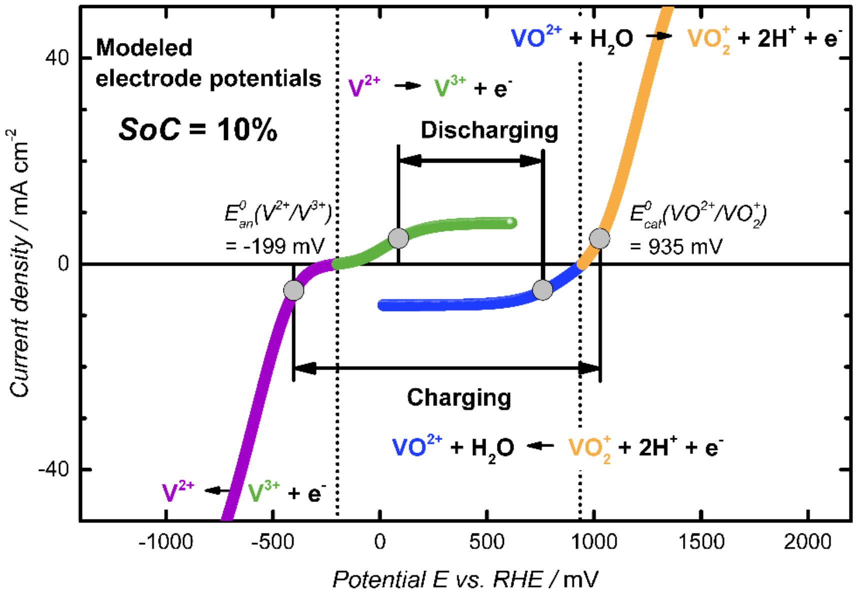

Figure 11: Modeled current vs. anode and cathode potential at an *SoC* of 10%. The model is based on $c_{V^{2+}} = c_{VO_2^+} = 0.32\ \mathrm{M}$, $c_{V^{3+}} = c_{VO^{2+}} = 1.44\ \mathrm{M}$, $R_{\Omega,\mathrm{an}} = 2\ \Omega\ \mathrm{cm}^2$, $R_{\Omega,\mathrm{cat}} = 2\ \Omega\ \mathrm{cm}^2$, $R_{\mathrm{ct,an}} = 100\ \Omega\ \mathrm{cm}^2$, $R_{\mathrm{ct,cat}} = 10\ \Omega\ \mathrm{cm}^2$, $i_{\mathrm{lim,dc}} = \pm 8\ \mathrm{mA\ cm^{-2}}$, $i_{\mathrm{lim,ch}} = \pm 72\ \mathrm{mA\ cm^{-2}}$, $\alpha = 0.5$, $T = 298.15\ \mathrm{K}$, $E^0_{\mathrm{an}} = -0.199\ \mathrm{V}$, and $E^0_{\mathrm{cat}} = 0.935\ \mathrm{V}$.

2.7. Galvanostatic Charge and Discharge Voltage vs. Time

During galvanostatic charging or discharging, the cell voltage changes constantly. Additional processes affect the current-voltage characteristic, but all previous considerations qualitatively apply. The cell voltage is the difference of the electrode potentials, dominated by the *OCV*, but also depends on the charge or discharge current density. Figure 12 shows experimental data from a charge-discharge cycle of a VRFB single cell with 25 cm^2 of active geometric electrode area. The electrolyte flow rate (FR) was 100 ml min$^{-1,}$ and the electrolyte temperature was 20°C. The cell used an FAP 450 membrane (i.e., a fluorinated anion exchange membrane), and the magnitude of the charge-discharge current density was ±60 mA cm^{-2}.

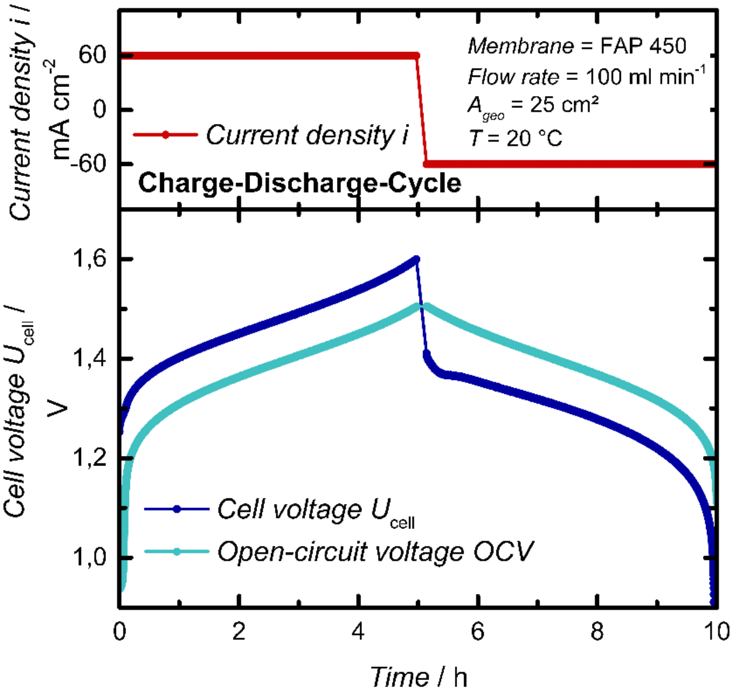

Figure 12: Experimental charge-discharge cycle of a VRFB single cell at a current density of $\pm 60\ \mathrm{mA\ cm^{-2}}$ with an active geometric area of $A_{\mathrm{geo}} = 25\ \mathrm{cm}^2$. Shown are the current density i (red line) and the cell voltage U_{cell} (blue line) measured with the single cell together with the *OCV* (cyan line) measured with an *OCV*-cell. The electrolyte contained a total vanadium concentration of 1.6 M (based on 0.8 M V^{3+} and 0.8 M VO^{2+} in the as-received state, i.e., before charging) dissolved in 2.0 M aqueous sulfuric acid, its flow rate through anode and cathode was $100\ \mathrm{ml\ min^{-1}}$, and the electrolyte temperature was $T = 20°\mathrm{C}$.

The course of the cell voltage U_{cell} over time during galvanostatic charging and discharging (with $U_{\mathrm{cell}} = OCV + \eta_{\mathrm{cell}}$) can be explained as follows:

First, according to Eq. (21), the *OCV* increases with the *SoC* in the charging case and decreases in the discharging case. Also, for $SoC \rightarrow 0$ and $SoC \rightarrow 1$, η_{cell} increases due to increasing kinetic overpotentials ($\eta_{\mathrm{kin}} \propto \frac{i_{\mathrm{kin}}}{i_0}$, c.f., Eq. (24)), being a result of the fact that the exchange current densities i_0 for both electrode reactions approach zero (c.f., Eq. (22)):

$$\lim_{SoC \rightarrow 0,1} i_0 = \lim_{SoC \rightarrow 0,1} \left[SoC^{\alpha} (1 - SoC)^{1-\alpha} \right] = 0 \tag{39}$$

Also, the concentration overvoltage η_{c} increases with a decrease in reactant concentration. According to Eq. (34) and Eq. (28), the decreasing i_{lim} values as the *SoC* approaches 0 or 1 begin to approach the applied constant current density i, or $\frac{i}{i_{\mathrm{lim}}} \rightarrow 1$, which leads to rapidly diverging η_c values according to

$$\lim_{\frac{i}{i_{\mathrm{lim}}} \rightarrow 1} \eta_c = \lim_{\frac{i}{i_{\mathrm{lim}}} \rightarrow 1} \left[-\frac{RT}{\alpha F} \ln\left(1 - \frac{i}{i_{\mathrm{lim}}}\right) \right] = \infty \tag{40}$$

While a higher flow rate would result in smaller concentration overpotentials due to improved convection (and thereby a decreased diffusion layer thickness δ_{N} and increased i_{lim}, c.f., Eq. (28)), it would also lead to higher pumping losses.[36]

Interestingly, even the membrane resistance is dependent on the concentration of the different reactants. For anion exchange membranes such as the FAP 450, it can be observed that for specific electrolyte compositions or *SoC*, the ionic resistance of the membrane increases. This increase is particularly pronounced for discharging the battery at an *SoC* between 50-90%. In Figure 12, between hours 5-7, the discharge voltage is much lower than expected. Depending on the electrolyte pH, this observation can be explained by considering that VO_2^+ in the catholyte forms ionic complexes with sulfate anions that are negatively charged overall, such as $(VO_2^+ \cdot SO_4^{2-})^-$.[37] Upon discharge, these negative ions are suggested to adsorb on the surface or in the conduction channels of the membrane thereby limiting its conductivity. This phenomenon is known in the literature as the "power-drop effect" and is the subject of current research.[38,39] Accordingly, the resistance of cation exchange membranes also depends on the size and direction of the current density. Again, increased resistance can be observed during discharge. In this case, however, no tetra- or pentavalent but bi- and trivalent vanadium ions are responsible for the behavior. Presumably, V^{2+} ions migrate into the membrane during discharge and exchange for protons, which lowers the proton conductivity. This effect of cation poisoning was observed by Sun et al. for Cu^{2+} in water electrolyzers. However, it can be reversed by treating the membrane with sulfuric acid.[40]

2.8. Coulombic Loss Factors

In addition to voltage losses, losses of coulombic charge during a charge-discharge process also reduce the usable amount of energy of the battery. In the following, the physical relationships are discussed.

2.8.1. Cross-over Losses

Ion exchange membranes separate the anolyte and catholyte solutions, as shown in Figure 8. At the same time, they ensure electroneutrality on both sides of the membrane. Depending on their material composition, they conduct either cations such as H^+ or anions such as HSO_4^-. For cation exchange membranes (CEM), the membrane backbone material holds negative ionic groups such as sulfonic acid groups ($-SO_3^-$), which facilitate cation transport but restrict the passage of anions due to Donnan exclusion.[41] Cations such as protons move across the membrane in two different ways, i.e., the Grotthus and the vehicular mechanism. By the Grotthus mechanism, the proton forms hydrogen bonds to hydrolyzed water molecules present along with the negatively charged sites at the membrane's polymer backbone. With a respective driving force such as a gradient in potential or concentration, the proton is hopping from one water molecule to another. By the vehicular mechanism, the proton attaches to a water molecule and drags through the membrane with it. In anion exchange membranes (AEM), the same working principles prevail, except that the charge of the ions is reversed in each case.

Unfortunately, for both CEMs and AEMs, not only the desired H^+ or $HSO4^-$ ions travel across the membrane, but sometimes also vanadium ions.[42,43] This vanadium crossing leads to a self-discharge of the electrolyte. Thereby, cross-over V^{2+} and V^{3+} ions react with the VO^{2+} and VO_2^+ ions according to the following reactions:

V^{2+} and V^{3+} crossed-over into the catholyte are reacting to:

$$2VO_2^+ + V^{2+} + 2\mathrm{H}^+ \rightharpoonup 3VO^{2+} + H_2O \tag{41}$$

$$VO_2^+ + V^{3+} \rightharpoonup 2VO^{2+} \tag{42}$$

$$VO^{2+} + V^{2+} + 2\mathrm{H}^+ \rightharpoonup 2V^{3+} + H_2O \tag{43}$$

VO^{2+} und VO_2^+ crossed-over into the anolyte are reacting to:

$$2V^{2+} + VO_2^+ + 4\mathrm{H}^+ \rightharpoonup 3V^{3+} + 2H_2O \tag{44}$$

$$V^{2+} + VO^{2+} + 2\mathrm{H}^+ \rightharpoonup 2V^{3+} + H_2O \tag{45}$$

$$V^{3+} + VO_2^+ \rightharpoonup 2VO^{2+} \tag{46}$$

The ion cross-over proceeds via electromigration driven by the electric field across the membrane, via diffusion driven by the concentration difference, and via electro-osmotic drag driven by the ion movement creating a convective flux.[44,45,46]

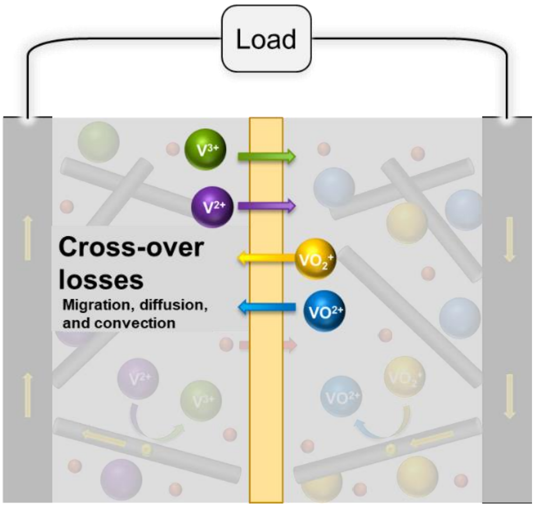

Figure 13: Charge losses upon cross-over of charged vanadium species across the membrane. The ion cross-over proceeds via electromigration, diffusion, and electro-osmosis.

2.8.2. Shunt Current Losses

Shunt currents occur in stacks of multiple cells where the cells are electrically connected in series and hydraulically connected in parallel, as shown in Figure 14. Due to the hydraulically parallel electrolyte inlets and outlets, ionic circuits are formed between several anodes and cathodes of adjacent cells. These ionic circuits allow the oxidation of V^{2+} according to Eq. (1) and the reduction of VO_2^+ according to Eq. (2), leading to self-discharge in the stack and a consequent loss of charged vanadium species.[47,48,49]

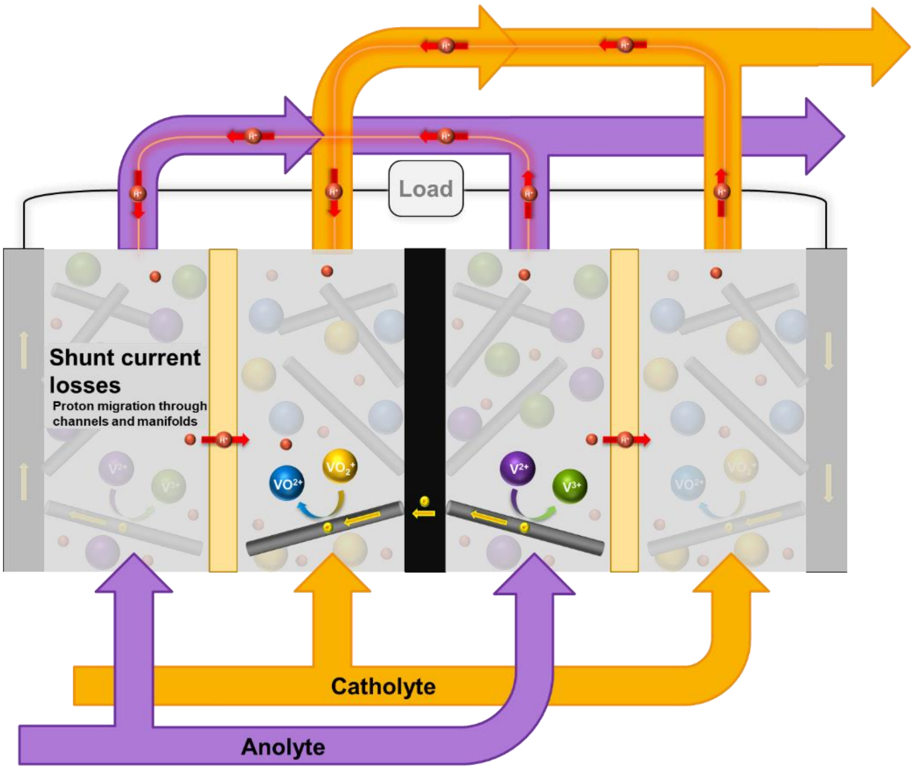

Figure 14: Shunt current losses upon proton transfer via the interconnection of two adjacent cells and across the membrane. The proton transfer allows for self-discharge reactions according to the oxidation of V^{2+} (see Eq. (1)) and the reduction of VO_2^+ (see Eq. (2)), leading to a loss of charged vanadium species. The graphic shows the proton circuit only for the cell outlet at the top. However, the processes apply also to the cell inlets at the bottom.

2.8.3. Side Reactions Losses

Besides vanadium cross-over losses, a small fraction of the current is due to side reactions at the respective anodic and cathodic equilibrium potentials. At the anode, potentials < 0 V vs. RHE prevail, allowing the hydrogen evolution reaction (*HER*) to occur (see also scheme in Figure 15a):

$$2H^+ + 2e^- \rightharpoonup H_2 \tag{47}$$

At the cathode, potentials of 0.9-1.1 V vs. RHE are present (Figure 4). At high *SoC* or high VO_2^+ concentrations, together with high charging overpotentials, potentials even > 1.23 V vs. RHE are possible. At these high anodic potentials, oxygen evolution can occur:

$$2H_2O \rightharpoonup O_2 + 4H^+ + 4e^- \tag{48}$$

In addition, at potentials significantly above 1 V vs. RHE, the oxidation of carbon and water to carbon dioxide can occur, leading to the corrosion of the graphite electrode.[50,51]

$$C + 2H_2O \rightharpoonup CO_2 + 4H^+ + 4e^- \tag{49}$$

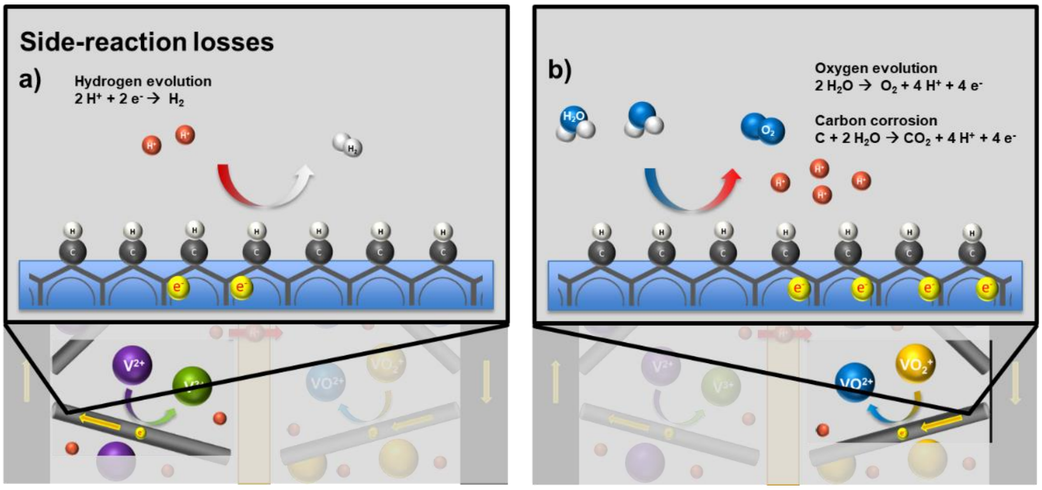

Figure 15: Coulombic losses due to side-reactions. a) At the anode, the reduction of H^+ leads to hydrogen evolution. b) At the cathode, the oxidation of H_2O leads to oxygen evolution and carbon corrosion.

2.9. Parasitic Loss Factors

The parasitic loss factors include the pumping losses, which are described by the pump power, P_{pump}. Here, the pump power required to circulate the electrolyte through the stack at a given volumetric flow rate, $\dot{V}$, a pump efficiency, η_{pump}, and for a given pressure drop, Δp, is:[36]

$$P_{\text{pump}} = \frac{\Delta p \dot{V}}{\eta_{\text{pump}}} \tag{50}$$

Other parasitic losses are the supply power of the battery management system, P_{BMS}, and the inverter, P_{inverter}. Together, all these necessary auxiliary power losses add up to the parasitic power, $P_{\text{parasitic}}$:

$$P_{\text{parasitic}} = P_{\text{pump}} + P_{\text{BMS}} + P_{\text{inverter}} \tag{51}$$

2.10. Battery Efficiencies

In order to evaluate and compare different battery designs, particular battery efficiency metrics are defined to evaluate different sub-aspects of the battery performance. These include energy efficiency, coulomb efficiency, voltage efficiency, and system efficiency, as described below.

2.10.1. Energy Efficiency

In general, the energy efficiency, η_{E}, during a charge-discharge cycle is defined as the fraction of energy discharged divided by the energy stored:

$$\eta_{\mathrm{E}} = \frac{\int U_{\mathrm{dis}}(t)|I_{\mathrm{dis}}(t)|dt_{\mathrm{dis}}}{\int U_{\mathrm{ch}}(t)|I_{\mathrm{ch}}(t)|dt_{\mathrm{ch}}} \tag{52}$$

2.10.2. Coulomb Efficiency

The coulomb efficiency, η_{C}, measures how much of a given amount of stored electrical charge can be discharged.

$$\eta_{\mathrm{C}} = \frac{\int dQ_{\mathrm{dis}}}{\int dQ_{\mathrm{ch}}} \tag{53}$$

2.10.3. Voltage Efficiency

The voltage efficiency, η_{V}, is defined as the ratio of the energy and the coulomb efficiency.

$$\eta_{\mathrm{V}} = \frac{\eta_{\mathrm{E}}}{\eta_{\mathrm{C}}} = \frac{\dfrac{\int U_{\mathrm{dis}}(t)|I_{\mathrm{dis}}(t)|dt_{\mathrm{dis}}}{\int U_{\mathrm{ch}}(t)|I_{\mathrm{ch}}(t)|dt_{\mathrm{ch}}}}{\dfrac{\int dQ_{\mathrm{dis}}}{\int dQ_{\mathrm{ch}}}} \tag{54}$$

If the battery is charging and discharging galvanostatically, the currents are constant and $I_{\mathrm{dis}}(t) = I_{\mathrm{dis}}$ and $I_{\mathrm{ch}}(t) = I_{\mathrm{ch}}$. With $\int dQ = \int I(t)dt$, the expression for the voltage efficiency is the ratio of the time average discharge and charge voltage:

$$\eta_{\mathrm{V}} = \frac{\eta_{\mathrm{E}}}{\eta_{\mathrm{C}}} = \frac{\dfrac{\int U_{\mathrm{dis}}(t)d\mathrm{t}}{\int d\mathrm{t}}}{\dfrac{\int U_{\mathrm{ch}}(t)d\mathrm{t}}{\int d\mathrm{t}}} \tag{55}$$

These average voltages can be extracted for each charge-discharge cycle using the respective data of battery voltage over measurement time, as for Figure 12.

2.10.4. System Efficiency

The system efficiency, η_{sys}, accounts for the parasitic losses due to the pumps, the BMS, and the inverter. Accordingly, the usable energy during discharge decreases by $P_{\mathrm{parasitic}}$, while the energy spent for charging the battery increases by $P_{\mathrm{parasitic}}$:

$$\eta_{sys} = \frac{\int U_{\mathrm{dis}}(t)i(t)dt_{\mathrm{dis}} - P_{\mathrm{parasitic}}}{\int U_{\mathrm{ch}}(t)i(t)dt_{\mathrm{ch}} + P_{\mathrm{parasitic}}} \tag{56}$$

2.11. Degradation Mechanisms

2.11.1. Degradation of Energy Storage Capacity

For storing the maximum energy capacity during battery charging, the amount of reducible V^{3+} in the anolyte must be equal to the amount of oxidizable VO^{2+} in the catholyte. Each V^{3+} that is not balanced by VO^{2+} cannot be reduced, and vice versa. In other words, the average valence of all vanadium ions must be 3.5 and their concentrations in the anolyte and catholyte must be equal. Otherwise, the usable energy storage capacity will be reduced. Apart from this obvious coulombic correlation, an ionic imbalance also increases the concentration and charge-transfer overvoltages, as explained in the previous sections. Increased overvoltages cause the maximum charge and discharge voltages to be reached earlier, again resulting in a decreased energy storage capacity. During extended battery operation, such undesired ionic imbalance reducing the usable energy storage capacity can evolve due to the following reasons:

The different vanadium ions have different diffusion coefficients in the electrolyte and within the membrane. As a result, some vanadium species move faster than others, leading to their directed transport across the membrane. Eventually, those faster ionic species will accumulate on one side of the membrane and shift the electrolyte's mean valence.[52]

The side reactions (*HER* and *OER*) have different rates. More transferred charge upon *HER* at the anode than upon *OER* at the cathode, for example, leads to less reduced V^{2+} than oxidized VO_2^+, shifting the mean valence from 3.5 toward higher values.

Oxygen intrusion from the air into the anolyte leads to the oxidation of V^{2+} species according to the following spontaneous reaction:

$$O_2 + 4V^{2+} + 4H^+ \rightharpoonup 2H_2O + 4V^{3+} \tag{57}$$

As a result, again, the mean valence will shift in positive direction.

There are different mitigation strategies to counteract electrolyte imbalance. One approach is mixing the anolyte and catholyte. As another approach, an electrolyzer cell can counteract a positive shift in mean valence.[53] The electrolytic cell connected to the positive electrolyte employs the following half-cell reactions:

$$VO_2^+ + 2H^+ + 2e^- \rightharpoonup VO^{2+} + H_2O \tag{58}$$

$$H_2O \rightharpoonup 1/2\, O_2 + 2H^+ + 2e^- \tag{59}$$

Also, electrolyte additives are used.[37] Since most frequently required, reducing agents are given to the electrolytes where they are oxidized by vanadium. Possible additives are ethanol, ethylene glycol, or oxalic acid, which are preferably entirely oxidized to water and CO_2. Being entirely converted, they would not introduce any impurities that may poison the electrodes and decrease their reaction kinetics. Exemplary, oxalic acid reacts with VO_2^+ in the catholyte as follows:

$$2VO_2^+ + H_2C_2O_4 + 2H^+ \rightharpoonup 2VO^{2+} + 2H_2O + 2CO_2 \tag{60}$$

2.11.2. Degradation of Voltage Efficiency

During extended cell operation, the voltage efficiencies decrease, which can have several reasons. As discussed above for the energy storage capacity degradation, an imbalance in ionic concentration and average valence leads to increased voltage losses and, thus, to the degradation of the voltage efficiency (c.f., Eq. (55)).

In addition, the electrode can be damaged by excessive charging voltages (corrosion), as shown in Figure 15. The oxidation of carbon from the electrode irreversibly forms CO_2. Due to this surface corrosion, part of the reaction surface is lost, resulting in higher kinetic overvoltages and thus lower voltage efficiencies.[25]

Curiously, it was observed that the kinetic overvoltages of the electrodes also increased during longer-term operation, even though balance in reactant concentration and valence was ensured.[25,26,27] This occurred even though the electrodes operated at mild conditions such as intermediate electrode potentials around 50% *SoC* and moderate electrolyte temperatures below 30°C. Previous attempts at finding an explanation such as the decrease in catalyzing surface oxygen groups could not be unambiguously confirmed experimentally.[54] Also, the authors could not explain various additional phenomena observed in the electrode behavior, such as the degradation's pronounced reversibility after cathodic electrode resting potentials or the inhibition of the *HER* in the presence of V^{2+}/V^{3+}-electrolyte.

The central part of this work elaborates an explanation for the observed, so far inconsistent electrode behavior (see chapter 4.2).

2.12. Materials and Components

2.12.1. Electrodes

The electrodes are among the most crucial components of the battery. Their essential function is to provide a catalytically active surface on which the reactions take place (Eq. (1) and (2)), lowering the activation energy of the reactions to facilitate the charge transfer. In addition, the electrodes have to conduct the electrons transferred during the reaction. The resulting partial resistances for charge transfer and electron conduction make a decisive contribution to the overall resistance of the battery. Moreover, the electrodes must be chemically and electrochemically stable in the acidic electrolytes within the potential range of $-0.3 < E < 1.1$ V vs. RHE (c.f., Figure 4). Homogeneous porosity is required for low pumping losses. Uniform thickness ensures that contact resistances between electrodes and bipolar plates are constant across the entire area.[55]

Commonly used are porous graphite felt, carbon felt, carbon paper, or carbon cloth electrodes, consisting of carbon or graphite fibers with a diameter of about 10 µm. Graphite or carbon felt electrodes are produced by needling a polyacrylonitrile (PAN) precursor and then pyrolyzing and annealing the fiber mats. Defect-rich amorphous carbon restructures and forms graphite crystallites during annealing, thereby increasing chemical and electrochemical stability and electronic conductivity. The annealing temperature thereby decides the degree of graphitization. Graphitization takes place at 1500-2000°C[71], while carbonization is realized at lower temperatures of < 1500°C[56], which is why graphite electrodes generally show higher conductivity than their carbon pendants. Alternative precursor materials are regenerated cellulose fibers, resulting in rayon-based carbon or graphite felts.[55]

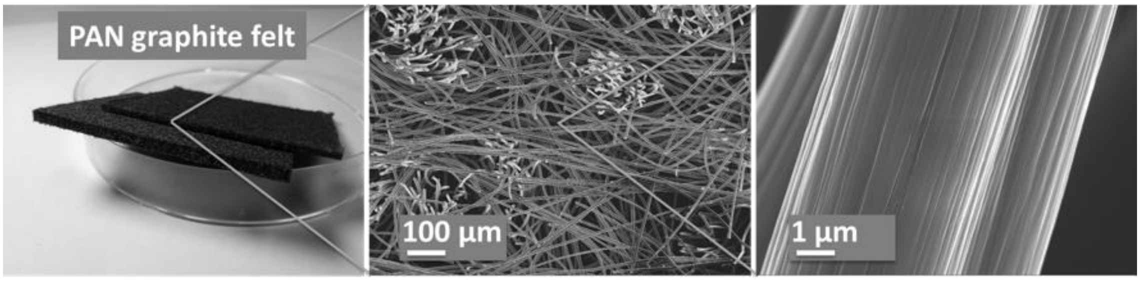

Figure 16: PAN-based graphite felt electrodes at different magnifications. Reproduced with permission from reference.[57]

In particular, improving the catalytic activity of the electrodes (e.g., by surface modification and surface area increase) in order to reduce the charge transfer resistance promises to drastically improve battery performance drastically.[15,16] Various treatment procedures have been suggested, including chemical,[58,59] electrochemical,[60,61,62,63] plasma,[24,64,65] or thermal treatment.[66,17,67] These studies observed that an increased number of oxygen functionalities would lead to improved kinetics. Also, some of these treatments increased the surface wettability and roughness, leading to an increased total surface area (*TSA*). Furthermore, the surface content of edge planes was discussed to be beneficial for electrode kinetics.

These effects were investigated in detail in the first part of the results of this thesis.[57] While the literature generally assumed surface oxides to be mainly responsible for improving the electrode kinetics, here, a rather minor effect of surface oxides was observed. Instead, carbon edge sites were identified to be decisive for the kinetics, agreeing with other recently published work.[68]

Besides the improved kinetics upon an initial oxidation of the electrode before its assembly in the cell, another phenomenon is observed upon electrode operation. While the electrodes generally exhibit slower kinetics for the V^{2+}/V^{3+} reaction than for the VO^{2+}/VO_2^+ reaction,[69,70,71] the V^{2+}/V^{3+} kinetics is shown to decrease with time of cell operation.[72,57,73,54] Moreover, the kinetics can be regenerated by maintaining the electrode at anodic potentials of > 0.8 V vs. RHE.[74,75] Previously, based on the assumption that surface oxygen functionalities are responsible for the activity, it was presumed that decreased kinetics must correspond to a decreased oxygen content. However, since the correlation between oxides and catalytic activity is not necessarily valid, another effect must be responsible for the degradation. Other explanations referred to the transition of ordered sp^2-carbon into disordered and less conductive sp^3-carbon.[76] However, the transition of sp^2- into sp^3-carbon is irreversible, contradicting the fact that the degraded kinetics can be regenerated reversibly. In the second part of the results of this thesis, a novel explanation for the anode kinetics degradation is presented: instead of ascribing it to a loss of active surface sites due to oxide reduction, it is shown that V^{2+} adsorbs on the surface of the anode electrode and thus inhibits active surface sites.[33]

Various electrode materials are suitable for use in VRFBs, comprising similar fiber properties but different geometric structures. Graphite felts, for example, whose fibers are needled, are available in thicknesses between 2-5 mm. On the other hand, carbon papers consist of fibers that lie unordered in a plane. Their thickness is only about one-tenth of that of graphite felts, i.e., in the range of 0.2-0.4 mm. Like carbon paper, carbon fabrics or cloth also have thicknesses in the range of 0.2-0.4 mm, and they have a woven structure.[55] Due to their small thickness and, thus, the short distance between the membrane and bipolar plate, carbon papers and carbon fabrics are also called zero-gap electrodes.[77]

One of the main differences between graphite felts, carbon papers, and graphite sheets is their electronic resistance due to their different geometric structures. The total resistance of the electrodes is composed of the material resistance due to through-plane conductance and the contact resistance between electrodes and bipolar plates. Both depend strongly on the electrode compression, so inhomogeneous thickness and density may lead to increased cell resistances and substantially limit the stack performance.[78] The thin carbon paper and fabric electrodes result in a shorter conduction path and, thus, lower electrical resistances. Moreover, such thin electrodes can also be compressed more strongly without fiber breakage, leading to lower contact resistances. Consequently, papers and fabrics show an overall electrode resistance about half as large as that of felts.

On the other hand, the different electrode types differ in their properties with regard to electrolyte flow. The Darcy-Weisbach equation describes the hydraulic pressure drop Δp_{porous}(Pa) of the electrolyte across a porous electrode in the stack for a given volumetric electrolyte flow rate $\dot{V}$ (in $\mathrm{m^3\ s^{-1}}$)[36]

$$\Delta p_{porous} = \frac{\mu \cdot l \cdot \dot{V}}{\kappa \cdot A} \tag{61}$$

where μ is the dynamic viscosity of the electrolyte ($\mathrm{Pa \cdot s}$), l the length of the porous electrode (m), κ the permeability ($\mathrm{m^2}$) and $A = b \cdot d$ the flow-through cross-sectional area of the electrode ($\mathrm{m^2}$), resulting from its width b (m) and thickness d (m). Compared to graphite felt electrodes, zero-gap electrodes would show a much higher pressure drop due to their smaller thickness (assuming the same permeability and flow rate). For this reason, zero-gap electrodes are combined with structured bipolar plates in the battery, which reduces the electrolyte flow-through length significantly.

The flow-through length also influences the local distribution of the areal current density within the electrode. Due to the continuous reactant consumption, the reactant concentration becomes increasingly depleted along the flow direction in the electrode. Due to this depletion, the concentration overvoltages increase along the flow-through length, decreasing the local current density.[79,80] Moreover, as the flow-through length increases, the depletion zone starting from the membrane widens. The reason for this is that the electronic conductivity of the electrodes ($\sigma_{\mathrm{el}} \approx 3\ \mathrm{S\ cm^{-1}}$) is about ten times greater than the ionic conductivity of the electrolyte ($\sigma_{\mathrm{ion}} \approx 0.3\ \mathrm{S\ cm^{-1}}$).[32] To minimize the unfavorable ionic conduction path, the reaction centers are located as close as possible to the membrane. A design variant by Battharai et al. takes the developing concentration profile into account and introduces narrow channels for the electrolyte in- and outlet into the electrode. Thereby, the in- and outlet channels have a width of 2-5 mm and are arranged in the interdigitated design, so that the electrolyte is forced to flow along a path from inlet to outlet channel through the electrode land (c.f., Figure 17a). The electrode land has typically a width of 20-50 mm, being much shorter than the usual electrode length of 100-300 mm. In this way, the shorter electrolyte flow paths lead to improved electrode utilization, smaller concentration overpotentials and smaller pressure losses.[81]

According to the proposed design, the channels must keep a distance to the ends of the electrode, matching the width of the electrode land, as indicated by the semicircles in Figure 17a. Otherwise, the electrolyte would favorize the shortest path through the electrolyte and, hence, would flow primarily through the upper and lower ends of the electrode. However, in the area at the electrode ends, the flow length is higher than in the mid of the electrode resulting in a non-uniform flow distribution and increasing the concentration overpotentials. As a possible solution, it is suggested to block the electrode ends with an adhesive, such as PVC-U mixed with the solvent tetrahydrofuran (THF). After the solvent has evaporated, the electrode fibers are coated by PVC-U rendering the electrode ends impermeable for electrolyte flow. This way, the channels can reach close to the electrode ends, increasing the flow uniformity and decreasing the concentration losses (c.f., Figure 17b). The proposed design was invented during this PhD thesis and a patent is filed for.[82]

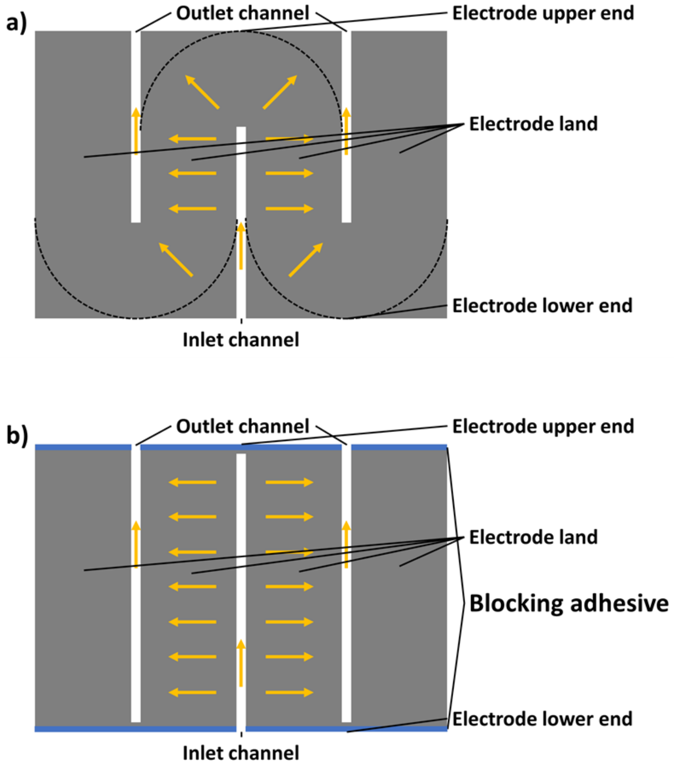

Figure 17: Electrode designs as alternatives to the flow-through design introducing interdigitated electrolyte flow channels decreasing concentration overpotentials and pressure losses. In a), the distance between channel ends and electrode ends is equal to the electrode land width leading to compromised electrolyte flow distribution.[81] In b), the electrode ends are blocked by an adhesive so the channels can reach closer to the electrode ends. This results in a more uniform flow distribution further decreasing the concentration overpotentials.[82]

A further advantage of the shorter flow paths is that, supposing constant electrolyte velocities, the electrolyte has a shorter retention time in the electrode. During this shorter time, at a given (areal) current density, the electrolyte will therefore suffer less educt depletion, and, as a consequence, the electrode can have a smaller thickness. Due to the complex manufacturing process of PAN graphite felts, unfortunately, it is not trivial to produce felts with smaller thickness, and, at the same time, ensure low thickness tolerances over the area. Therefore, within the framework of this thesis, a process for cutting strips or plates of felt elements was developed and approved, providing felt elements of < 1 mm thickness at a tolerance of < 0.05 mm. A corresponding device was proposed which employs several diamond band saws allowing the simultaneous production of the felt elements in an endless process, for which a patent has been granted.[83]

2.12.2. Membranes

The membrane separates the two half-cells and prevents the mixing and self-discharge of the anolyte and catholyte. At the same time, however, it is permeable to ions to guarantee charge neutrality between the two half-cells. The membrane should provide high ionic conductivity, low vanadium permeability, high mechanic resistivity, high chemical stability, and low production costs.[41]

Different categories of membranes are the ion exchange membranes (IEM) and the porous membranes. The IEMs consist of polymer chains with functional ends with ionic groups. These fixed ionic groups conduct counterions of opposite charges.[84] The counterions flow across the membrane and provide charge balance. The most commonly used types of IEMs include cation exchange membranes (CEMs), anion exchange membranes (AEMs), amphoteric, bipolar, and mosaic membranes.[85]

CEMs comprise negatively charged functional groups such as $-SO_3^-$ groups (sulfonic acid) that conduct cations such as H_3O^+. In contrast, AEMs contain ends such as $-NH^{3+}$ groups (quarternary ammonium), that are conducive for HSO_4^-.[86] Amphoteric membranes contain both types of conducting groups in their backbone, limiting the directed mass transport and electrolyte imbalance.[87,88,89]

Porous membranes are based on the principle of size exclusion, being permeable to H_3O^+ but not to vanadium ions.[90] Also called nanofiltration membranes, they require pore diameters between $2.5 - 6$ Å, larger than hydrated protons but smaller than hydrated vanadium ions.[91] Advantageous is their cost-effective synthesis, while still providing mechanical strength.

Also, combinations of CEMs (Nafion^{TM}) with porous nanofiltration membrane material (VanadION membranes) promise the advantages of both technologies: high ion conductivity, ion selectivity, mechanical strength, and low production costs.[92]

2.12.3. Electrolytes

In the electrolyte of VRFBs, the dissolved vanadium concentration determines the energy density.[93] While the anolyte contains V^{2+} and V^{3+}, the catholyte carries VO^{2+} and VO_2^+. The VO_2^+-solubility increases with sulfate concentration but decreases with temperature, limiting the maximum dissolvable V concentration. At 1.8 M, VO_2^+ readily precipitates as V_2O_5 above 50°C.[94] In contrast, the solubility of V^{2+}, V^{3+}, and VO^{2+} decreases with sulfate concentration and increases with temperature. Consequently, standard practical compositions are 1.6-2.0 M vanadium dissolved in 4-5 M total sulfate concentration,[37] suggesting an operating electrolyte temperature range between 10-40°C.

Another parameter defining the electrolyte physical characteristics is its viscosity, which depends on the electrolyte temperature and its *SoC*, i.e., the concentrations of different vanadium species.[32] For the anolyte at 25°C, the dynamic viscosity takes on values of $7.0\ \mathrm{mPa\ s}$ for $20\%\ SoC$ and $5.0\ \mathrm{mPa\ s}$ for $80\%\ SoC$. For the catholyte, the viscosity is 4.5 mPa s for 20% *SoC* and 4.0 mPa s for 80% *SoC*. Moreover, compared to 25°C, the viscosity decreases by ~1.5-fold at 40°C and it increases by ~1.5-fold at 10°C.

Within the *SoC* range of 20-80%, the ionic conductivities of anolyte and catholyte vary between 0.22-0.30 S cm^{-1} and 0.32-0.42 S cm^{-1}, respectively, due to a change of the proton concentrations.

The density at 25°C and 50% *SoC* is 1.39 g cm^{-3} and 1.36 g cm^{-3} for the anolyte and catholyte, respectively, and only slightly decreases with temperature $(0.08\ \mathrm{g\ cm^{-3}}/10\ \mathrm{K})$ or for a different *SoC* $(0.1\ \mathrm{g\ cm^{-3}}/100\%\ SoC)$.

Moreover, there are several electrolyte additives that improve the electrolyte properties. The addition of a small amount of phosphoric acid (H_3PO_4) prevents the V_2O_5 precipitation at elevated temperatures. In the absence of phosphoric acid, VO_2^+ can complex with water to $VO_2^+(H_2O)_2$, forming the intermediate $VO(OH)_3$ with the release of a proton, which precipitates as V_2O_5 by further deprotonation. The presence of H_3PO_4 leads to V-O-P bond-formation, which suppresses the deprotonation of $VO(OH)_3$ and the V_2O_5 precipitation at elevated temperatures of 40°C, thereby increasing the operating temperature window.[95,37]

Also, the addition of hydrochloric acid increases the VO_2^+ temperature stability.[96] A mixed-acid electrolyte consisting of 5 M hydrochloric and 2.5 M sulfuric acid increases the dissolvable vanadium concentration to 2.5 M (increasing the energy density by about 70%), and increases the temperature window to -10 to +50°C.[97,49,98]

Furthermore, the addition of glycerol and n-propyl alcohol leads to better VO^{2+}/VO_2^+ kinetics.[99] On the other hand, adding 5 mM Sb^{3+}[100] or 10 mM Bi^{3+}[101] to the electrolyte facilitates the formation of metallic Sb and Bi deposits on the anode during the charging process which are catalytically active for the V^{2+}/V^{3+} redox reaction but inactive for the *HER*.

2.12.4. Bipolar Plates and Flow Field Design

Bipolar plates electrically connect the electrodes and separate the anolyte and catholyte of two adjacent cells. Also, they reinforce the stack mechanically.[102,103] Therefore, the BPP should comprise a high electrical conductivity, electrochemical and mechanical stability, and should be impermeable for the electrolyte.[104]

As a material, carbon-polymer composites match all requirements. Conductive carbon black, fibers, or nanotubes are combined with binders such as polypropylene, polyethylene, fluoropolymers, or epoxy resin.[105,106] Manufacturing processes are extrusion, compression molding, injection molding, or injection compression molding.

A commonly used standard is TF6 from SGL Carbon. TF6 is an extruded 0.6 mm thick graphite-fluoropolymer composite sheet. The composite consists of 94% expanded graphite with 6% ethylene tetrafluoroethylene copolymer (ETFE) filler.[107] Due to the high graphite content, TF6 has a low electrical resistivity of $7.6 \cdot 10^{-4}\ \Omega\ \mathrm{cm}$, resulting in an area-specific resistance of $0.4\ \mathrm{m\Omega\ cm^2}$, which is negligible compared to the BPP’s contact resistance to the electrode.[108] To reduce the significant contact resistance between the bipolar plate and electrode, electrically conductive adhesive bonds between bipolar plates and electrodes have been successfully investigated.[109,110]

In addition to the flat flow-through design for graphite felt electrodes, the bipolar plates can also have a flow field integrated for zero-gap electrodes.[104] In this case, the electrolyte flows in channels in the bipolar plate, significantly reducing the pressure losses. In case of the flow-by design, the ends of the inflow and outflow channels are open. The electrolyte flows along one side of the electrode, which, however, entails large concentration overpotentials. Conversely, for the interdigitated flow field (IDFF) design where the flow channel ends are closed, the electrolyte is forced across the land and through the porous electrode, which substantially reduces concentration overpotentials but increases pressure losses compared to the flow-by design.[77] While the pressure losses with the IDFF design are still much smaller than with the flow-through design, decisive parameters are the channel and land width, the channel depth, and the electrode thickness and permeability. [111] Numerical modeling can help determine the optimum between pressure losses, mass transport, and flow distribution across the flow field.[112]

2.12.5. Flow Frames

Flow frames ensure that the electrolyte is led to and from the electrode and that parts of the electrolyte flow do not bypass the electrode. Also, their thickness sets the desired electrode compression. In addition, the flow frames contain meander channels that extend the length of the electrolyte connection between the cells to reduce the shunt currents.[113] The pressure drop in the channels is defined by the Darcy-Weisbach equation and depends quadratically on the flow rate rather than linearly as in the porous electrodes. Again, a trade-off between shunt current and pressure drop must be determined. Since the flow frame is a component in contact with the electrolyte, it must also be chemically resistant. Various sulfuric acid-resistant plastics such as polypropylene (PP), polyethylene (PE), or polyvinyl chloride (PVC-U, PVC-C) are suitable for this purpose. For reducing the complexity of the assembly process, the bipolar plate can be encapsulated with two flow frames, resulting in a compact and liquid-tight component.[114]

2.12.6. Current Collectors

The current collectors (CCs) contact the two BPPs at the outer ends of the stack (also referred to as monopolar plates (MPPs)) and conduct the current into the direction of the outer circuit. Due to the large currents, the material of the current collectors is required to be highly conductive, which is why often copper is used. Although copper comprises extraordinary conductivity and, consequently, offers low conduction resistance, after prolonged times of oxidation in the air, it is known to form an oxide layer responsible for undesired contact resistances between CC and MPP. For lab applications, the CCs are often gold-plated, which prevents the formation of an oxide layer ensuring low and reproducible contact resistances.[104] For industrial applications, costs are critical, and tin-plated copper plates can be used.[49]

Besides the physical surface properties, decisive for low contact resistances is a high contact pressure over the entire area. Tolerances in the planarity of the CCs, hence, can lead to areas with contact resistances drastically increased, inflicting issues such as a decreased stack performance and an uncontrolled heat generation. In order to compensate tolerances, carbon papers are added between CC and MPP, enabling areal uniform and low contact resistances.

During this thesis, a new approach for contacting the CC and the MPP was developed: A copper grid was pressed into the MPP, which is typically made of a relatively soft carbon-polymer composite material. After the application of 100 kg cm^{-2} in a hydraulic heavy-duty press, the copper grid (with a mesh size of 1 mm^2 and wire diameter of 0.3 mm^2) was fully embedded in the MPP. In a next step, the copper grid (facing out on one side of the MPP) was soldered with a copper CC plate. Due to the temperature sensitivity of the MPP, the solder metal was a low-melting solder alloy being Roses metal. The composite component of copper plate, copper grid and MPP showed unusually low total areal resistances of $< 5 \text{ m}\Omega \text{ cm}^2$ and offers to be a suitable combination of the CC and the MPP. A patent application was filed for the component and the method for producing it.[115]

2.12.7. Endplates

The endplates serve to fasten the stack plane-parallel and to apply a laterally even pressure. In particular, the contact pressure is essential for the electrodes and current collectors to ensure adequate electrical contact at every location.[116] The compression path of the electrodes must also be equal to ensure uniform electrolyte flow. Furthermore, a uniform pressure is critical for the functionality of the sealing.

The endplates are usually made of dimensionally stable materials with high stiffness in order to achieve the required homogeneous pressure distribution. In addition to selecting a material with a high elastic modulus, the plate thickness can also be increased. However, to ensure adequate handling, a compromise must be found between stiffness and weight, which is why the density of the material is also relevant.[117]

In addition to the choice of material, the plate geometry helps reducing weight. One method is to make the endplate in a ribbed design instead of a rectangular solid material, which makes it possible to reduce weight while maintaining good stiffness. Furthermore, a thin end plate can be supported by cross beams (e.g., solid or hollow stainless steel sections), increasing the pressure at critical plate areas.

Also, the connecting and tightening method bears design benefits. Commonly, tightening rods and nuts are used to compress the cell stack. However, other fastening principles such as tie-bands are possible for saving the plate area needed for the drill holes required for tightening rods, thereby decreasing dead stack volume.[118]

3. Experimental Methods

3.1. Three-electrode Half-cell Assembly for Rotating Disk Electrodes

Rotating disk electrodes (RDE) were employed in three-electrode half-cells to investigate the electrode-electrolyte interaction of model electrode materials, as illustrated in Figure 18. The half-cell was a glass compartment equipped with a mercury/mercurous sulfate (Hg/Hg_2SO_4) reference electrode (RE), a graphite felt counter electrode (CE), and a graphite disk working electrode (WE). The RE was sitting in a glass tube filled with vanadium-free 2 M sulfuric acid to protect it from vanadium ions that could change its standard potential. The glass tube functioning as an electrolyte bridge dipped in the vanadium electrolyte, ionically contacting it with the RE via a porous glass frit. The CE was a 2 cm^2 graphite felt impaled by a carbon composite stick of 1 mm diameter. The WE was a graphite disk made of glassy carbon (GC) or highly-oriented pyrolytic graphite (HOPG) in the basal or edge plane orientation. The disk was embedded into a PTFE body which rotated at a constant rotation rate, which ensured constant convection and, thus, continuous reactant mass transport towards the electrode surface. A constant N_2 gas flow passed over the electrolyte to protect it from the intrusion of oxygen from ambient air, which could potentially oxidize V^{2+}.

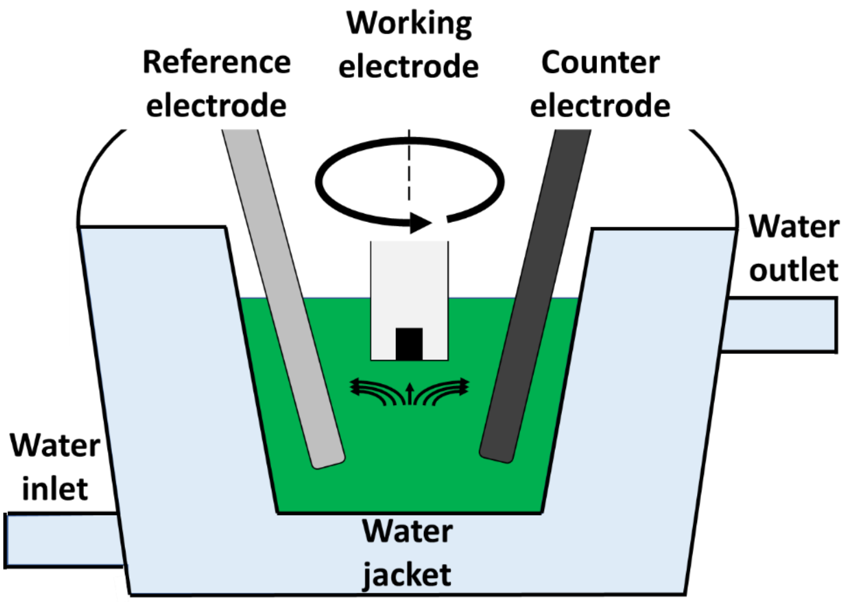

Figure 18: Schematics of a water-jacketed three-electrode half-cell comprising a reference, counter, and working electrode. The electrolyte temperature in the cell was controlled by thermostatted water flowing through the cell jacket via the water in- and outlet.

3.2. Cyclic Voltammetry with RDE Half-cells

Cyclic voltammetry (CV) is an experimental method for investigating redox reactions at electrode model surfaces. In this work, the material of the model surfaces was either glassy carbon (GC) or highly oriented pyrolytic graphite (HOPG) in basal plane and edge plane orientation. These GC and HOPG electrodes were rotating disk electrodes integrated in an RDE setup. The reactions investigated were the V^{2+}/V^{3+}-reaction and the HER. The electrode potential was scanned linearly within a selected voltage window at a constant scan rate typically in the range of 1-100 mV s^{-1}. At the same time, the current response is recorded, providing information on the reactants, the electrodes, and the electrolytes.[119,120, 121]

Figure 19 demonstrates a typical CV of a basal plane HOPG RDE in a 2 M H_2SO_4 electrolyte containing 1.6 M V^{2+}/V^{3+}. The electrode rotation rate was 200 rpm, and the electrolyte temperature was 25°C. In Figure 19a, the voltage is controlled between -1.8 V and 0.2 V vs. Hg/Hg_2SO_4 over time at a scan rate of 20 mV s^{-1}, in Figure 19b, the current response is measured over time, and in Figure 19c the measured current is plotted over the controlled voltage. The equilibrium potential in Figure 19 at -0.936 V vs. Hg/Hg_2SO_4

corresponds to -0.262 V vs. RHE,[122] being close to -0.255 V vs. RHE, the theoretical standard potential of the V^{2+}/V^{3+}-reaction. Accordingly, the V^{2+}/V^{3+}-ratio is close to 1/1.

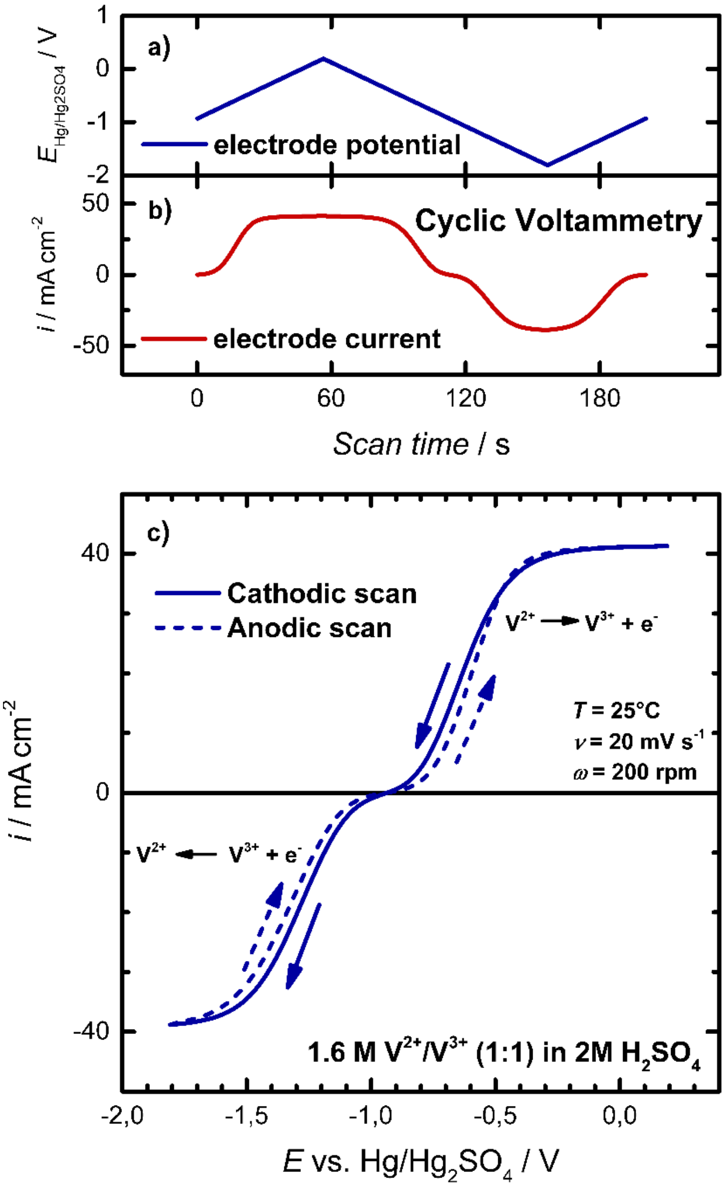

Figure 19: Experimental data of a CV with a basal plane HOPG RDE in a three-electrode half-cell. The electrode rotation rate was 200 rpm, and the electrolyte temperature was 25°C. a) Voltage vs. time, b) current vs. time, and c) current vs. voltage curve.

As can be seen, the current-voltage curve in Figure 19c precisely agrees with the modelled current-voltage-relationship in Figure 9, representing the characteristic voltage losses derived in Section 2.4. Between -1.3 V and -0.6 V, the current is kinetically controlled, following an exponential course described by the Butler-Volmer equation (c.f., Eq. (23)). At below -1.3 V and above -0.6 V, the current takes on a sigmoidal shape, approaching a constant limiting current of about $i_{\mathrm{lim}} = \pm\, 40\ \mathrm{mA\,cm^{-2}}$. In this region, the overpotentials are sufficient for the entire reactant to be consumed at the electrode surface. The amount of reactant reaching the surface is given by the Levich equation describing the mass transport of reactant from the bulk of the electrolyte towards electrode surface via convection and diffusion:

$$i_{lim} = 0.62 \cdot n \cdot F \cdot A \cdot D^{\frac{2}{3}} \left(\frac{2\pi}{60} \cdot \omega\right)^{\frac{1}{2}} \left(\frac{\tilde{\eta}}{\rho}\right)^{-\frac{1}{6}} C_0 \qquad \propto \quad \omega^{\frac{1}{2}} \tag{62}$$

In Eq. (62), 0.62 is a numeric constant (-), n the number of transferred electrons (-), F the Faraday constant $(\mathrm{C\,mol^{-1}})$, A the geometric electrode area $(\mathrm{cm^2})$, D the diffusion coefficient $(\mathrm{cm^2\ s^{-1}})$, ω the electrode rotation rate (rpm) and its conversion factor $2\pi/60$ to $(\mathrm{rad\,s^{-1}})$, $\tilde{\eta}$ the dynamic electrolyte viscosity $(\mathrm{g\,(cm\,s)^{-1}})$, ρ the electrolyte density $(\mathrm{g\,cm^{-3}})$, and C_0 the educt concentration $(\mathrm{mol\,cm^{-3}})$. As indicated in Eq. (62), i_{lim} increases linearly with the square root of the rotation rate, i.e., with $\omega^{1/2}$, which is confirmed in Figure 20 when varying the rotation rate between 100 rpm and 1600 rpm.

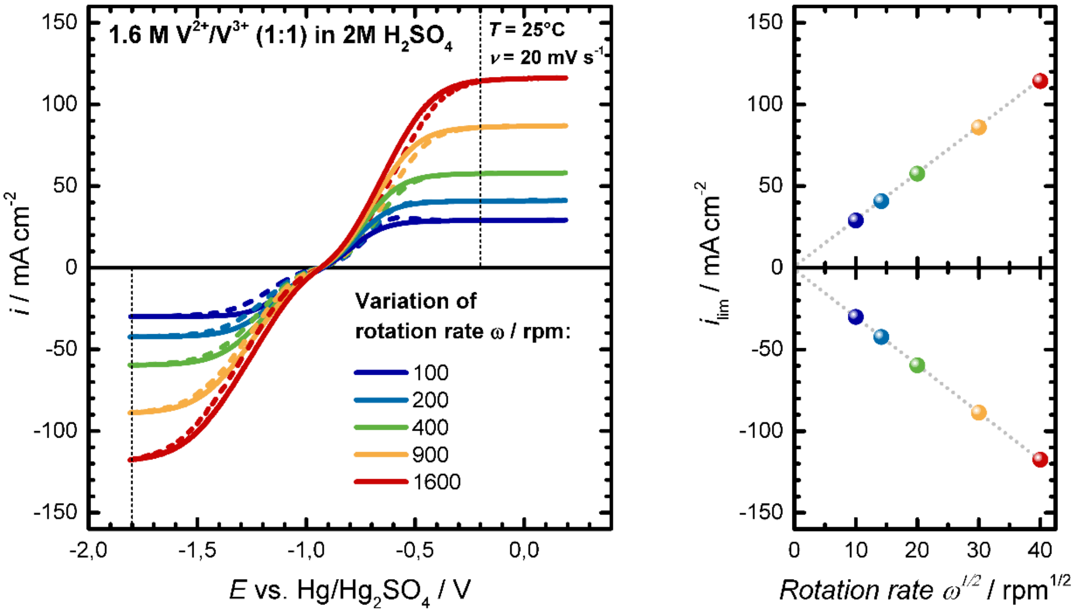

Figure 20: CVs with a basal plane HOPG RDE at rotation rates ω between 100 rpm and 1600 rpm (left). The limiting currents increase linearly with the square root of the rotation rate $\omega^{1/2}$ (right). Reproduced with permission from supporting information of reference.[33]

3.3. Full Single-cell Assembly for Graphite Felt Electrodes

Figure 21 shows a model drawing of the redox flow laboratory single cell assembly designed in-house and used in this work. The assembly is bolted together with ten M8 machine screws (c.f., (1) in Figure 21), each tightened to a torque of 10 Nm. The resulting contact pressure is distributed by aluminum endplates (c.f., (2) in Figure 21) with a thickness of 20 mm, compressing the cell evenly. Towards the endplates, PVC-U plates (c.f., (3) in Figure 21) are fixed by four M4 screws (c.f., (4) in Figure 21). The PVC-U plates electrically insulate the endplates from the gold-plated copper current collectors (c.f., (5) in Figure 21). Also, the PVC-U plates hold 4 mm PVC pins (c.f., (6) in Figure 21) that align the current collectors (5) with the monopolar plates (MPPs) (c.f., (7) in Figure 21). The MPPs are made of an injection-molded PPG86 graphite-polypropylene compound (Eisenhuth GmbH, Germany). Their high graphite content of 86% provides a very high electrical (material) conductivity of about $100\ \mathrm{S\ cm^{-1}}$, resulting in low contact resistances to the current collector of roughly $50\ \mathrm{m\Omega\ cm^{2}}$. At the same time, they hold inlets and outlets for the acidic electrolyte, realized via screw-in connections (c.f., (8) in Figure 21) bonded with epoxy resin (c.f., (9) in Figure 21) as a sealant. The MPPs conduct the electrolyte uniformly to and from the graphite felt (GF) electrodes (c.f., (10) in Figure 21) according to the flow-through design and via several 1 mm holes. Before assembly, the 4.6 mm thick GF electrodes are punched to $25\ \mathrm{cm^2}$ pieces using a die (Spahn GmbH, Germany). The electrodes are routinely compressed by 20% to their desired final thickness of 3.7 mm in the cell, adjusted by several stacked PTFE flow frames (c.f., (11) in Figure 21). The flow frames are aligned via 3 mm PVC pins (c.f., (12) in Figure 21) and also seal the cell by resting against both the MPPs (7) and the membrane (c.f., (13) in Figure 21). The membrane material is Nafion$^{\mathrm{TM}}$ (NF 212) with a thickness of 50.8 µm.

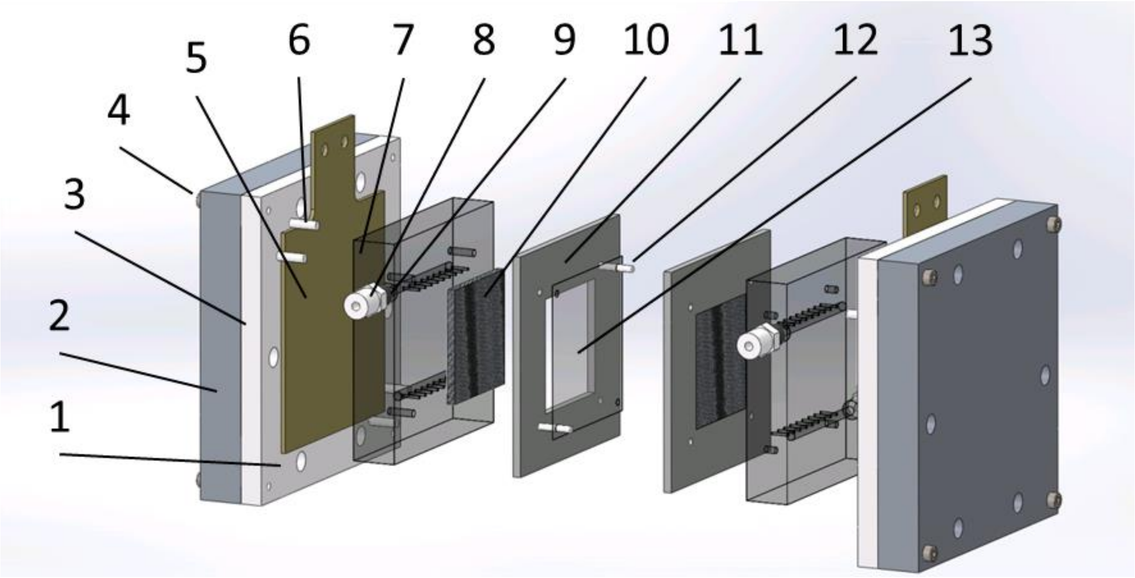

Figure 21: Schematic drawing of the single cell with 25 cm² active geometric electrode area: (1) M8x120 threaded holes for hexagon head screws, washers, and nuts, (2) 20 mm thick aluminum endplates, (3) PVC-U isolation plate, (4) M4x30 hexagon socket screws, (5) gold-plated Cu current collector, (6) 4 mm PVC-U pins, (7) 20 mm thick PPG86 monopolar plates, (8) G1/8” threaded screw-ins for DN04/06 tubings, (9) epoxy bonding, (10) 25 cm^2 GF4.6 graphite felt electrodes, (11) PTFE foil flow frames, (12) 3 mm PVC-U pins, and (13) 50 mm thick AEM (FAP450) or 50 mm thick CEM (NF212). Reproduced with permission from supporting information of reference.[33]

3.4. Full-cell Test Environment

Figure 22 represents the functional diagram of the test environment designed in-house. The test cell (c.f., (1) in Figure 22) receives its electrolyte from PTFE electrolyte lines which are linked by PP tubing connectors (EM-Technik GmbH, Germany). Since PTFE hoses have a small bending radius and high stiffness, a change of hose direction is possible via elbow fittings. Flexible hoses such as softened PVC contain plasticizers, so their use is not recommended, although they would simplify assembly. During prolonged operation, the electrolyte attacks plasticized PVC, partly dissolving it. While it is unclear whether the dissolved plasticizers contaminate the membranes and electrodes, it is best to avoid this potential problem. The electrolyte is fed by two NF60 diaphragm pumps (c.f., (2) in Figure 22) (KNF Neuberger GmbH, Germany). When selecting pumps and sensors, all wetted parts and seals must be made of corrosion resistant plastics. In some instances, PTFE-coated metal parts are installed. However, since the coating is prone to be damaged during operation, the metal parts might corrode. Consequently, all-plastic components are preferred. The electrolyte flow rate can be adjusted via a pump control voltage (0-5 V).

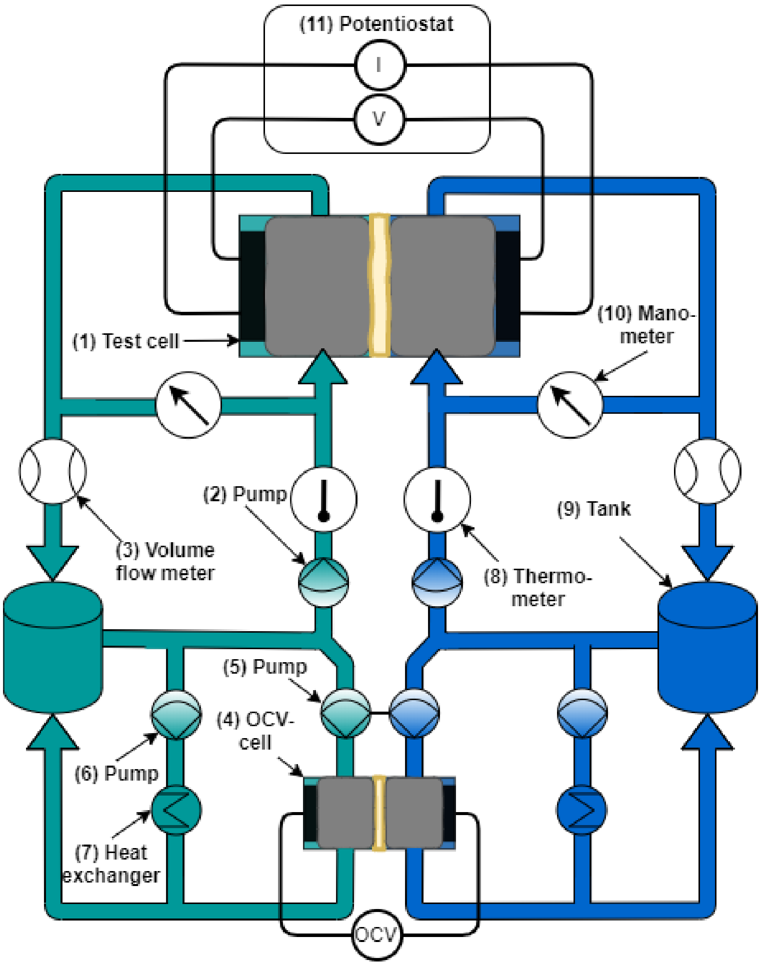

Figure 22: Functional diagram of the test environment for redox flow single-cell measurements with a flow diagram of the electrolyte and the measurement and control system. Reproduced with permission from supporting information of reference.[33]

3.4.1. Flow Rate Control

The flow rate is measured by two VZS005-PP oval wheel meters (c.f., (3) in Figure 22) (B.I.O.-TECH, e.K., Germany). The oval wheel counters provide a signal for each revolution of the oval wheels that corresponds to a defined electrolyte volume, independent of the viscosity of the electrolyte. An ICP DAS signal counter module (IPC2U GmbH, Germany) transmits these signals to a LabVIEW software environment, which calculates the flow rate and sends it to a PID controller. In a feedback loop, the PID controller compares the current flow rate with the intended flow rate and uses an ICP-DAS actuator module (IPC2U GmbH, Germany) to readjust the control voltage for the membrane pumps.

3.4.2. *SoC* Monitoring

A second parallel electrolyte circuit is used to evaluate the *SoC* of the vanadium electrolyte. An *OCV*-cell (BELLTEC, Germany) (c.f., (4) in Figure 22) was used to measure the *OCV* which can be translated to the *SoC* described by the *SoC*-*OCV* curve in Figure 5. A model drawing of the *OCV*-cell is shown in Figure 23. All parts are listed in the figure caption according to the numbers in the figure. Both electrolytes flow through the *OCV*-cell and past the voltage-sensing carbon rods inside. As a modification, the carbon rods were replaced by carbon fiber composite (CFC) rods (Carbon Composites, Germany), being mechanically more stable (c.f., (1) in Figure 23). The electrolyte flows at high velocity (approx. 3 cm s^{-1}), ensuring the *OCV*-cell reacts directly to *SoC* changes. For this purpose, an NFB25 double-head membrane pump (c.f., (5) in Figure 22) (KNF Neuberger GmbH, Germany) provides a constant 30 mL min^{-1} flow rate per electrolyte side. In addition, the carbon rods are epoxy-bonded to the PVC-U surrounding to avoid void volumes with residual electrolyte at different *SoC*, which would lead to an erroneous *OCV* value.

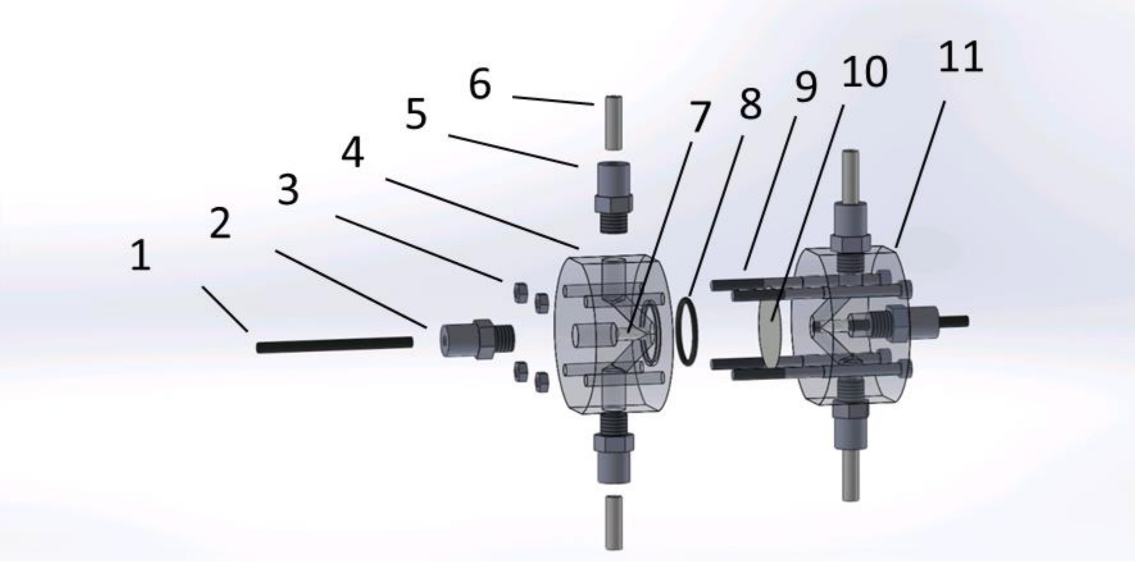

Figure 23: Schematic drawing of the *OCV*-cell for measuring the state of charge (*SoC*): (1) 4 mm carbon fiber composite (CFC) sticks, (2) threaded screw-in for CFC rods, (3) M4 V4A nuts, (4) PVC-U end plate, (5) threaded screw-ins for DN04/06 tubings, (6) DN04/06 PTFE-tubings, (7) epoxy bonding, (8) 2x22 FKM O-ring, (9) M4x65 V4A screws, (10) NF117 membrane with an open area between the compartments of ~1 cm^2, and (11) PVC-U end plate.

3.4.3. Temperature Control

A third parallel electrolyte circuit is used to control the temperature of the electrolyte. First, the electrolyte temperature is measured immediately before the electrolyte enters the test cell. The FEP-coated Pt100 resistance thermometers (c.f., (8) in Figure 22) are seated in PVC cylinders, as shown in Figure 24. All specific parts are listed in the figure caption referring to the numbers in the figure. For a length of 10 cm, electrolyte flows around the thermometers isolating their measuring tip (c.f., (3) in Figure 24) from external temperature fluctuations. The temperature is measured by an ICP-DAS sensor module and processed in a LabVIEW environment. A PID controller compares the measured with the target temperature. Depending on the offset, an ICP-DAS actuator module readjusts the control voltage of two additional NF60 membrane pumps (c.f., (6) in Figure 22) (KNF Neuberger GmbH, Germany). These pumps independently feed a plate heat exchanger (c.f., (7) in Figure 22) designed in-house and shown in Figure 25 with, again, all parts listed in the figure caption according to the descriptive numbers in the figure. The heat exchanger couples the heat to the water circuit of an A100 thermostat (Lauda GmbH, Germany) via heat exchanger plates made of TF6 (SGL Carbon) (c.f., (4) in Figure 25). Due to its high graphite content of > 90%, this graphite-polymer mixture has a high thermal conductivity of about 6 W $(m\ K)^{-1}$, about 20-30 times the thermal conductivity of conventional plastics. As a modification, 0.5 mm aluminum sheets mechanically support the TF6 plates against the water circuit to withstand the pressure from the electrolyte circuits (not shown).

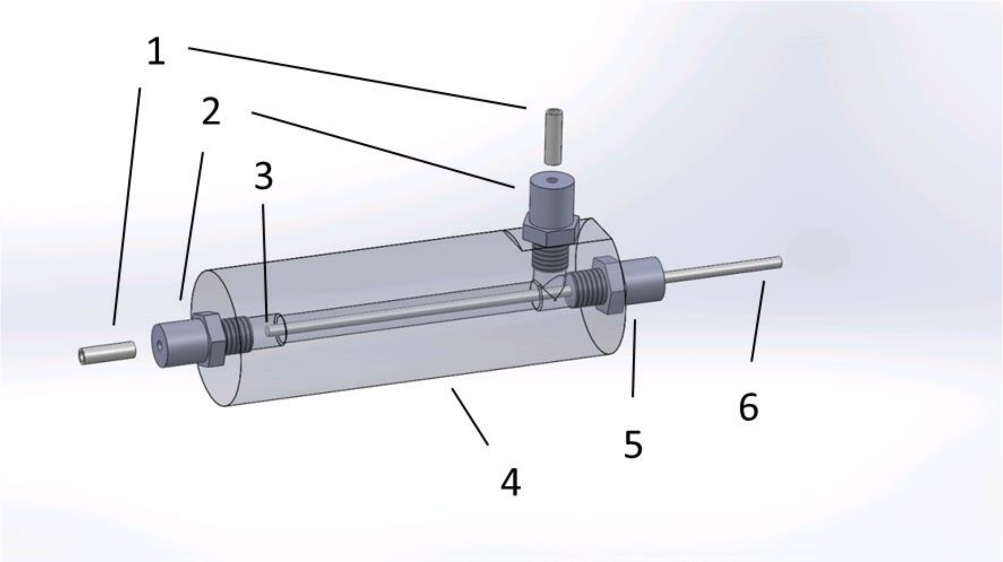

Figure 24: Schematic drawing of the Pt100 thermometer (FEP-coated) in a PVC-U-cylinder case: (1) DN04/06 PTFE-tubing, (2) G1/4” treaded screw-in for DN04/06 tubings, (3) FEP-coated Pt100 measuring

tip, (4) PVC-U body, (5) G1/4” treaded screw-in for Pt100 thermometer, and (6) FEP-coated Pt100 thermometer. Reproduced with permission from supporting information of reference.[57]

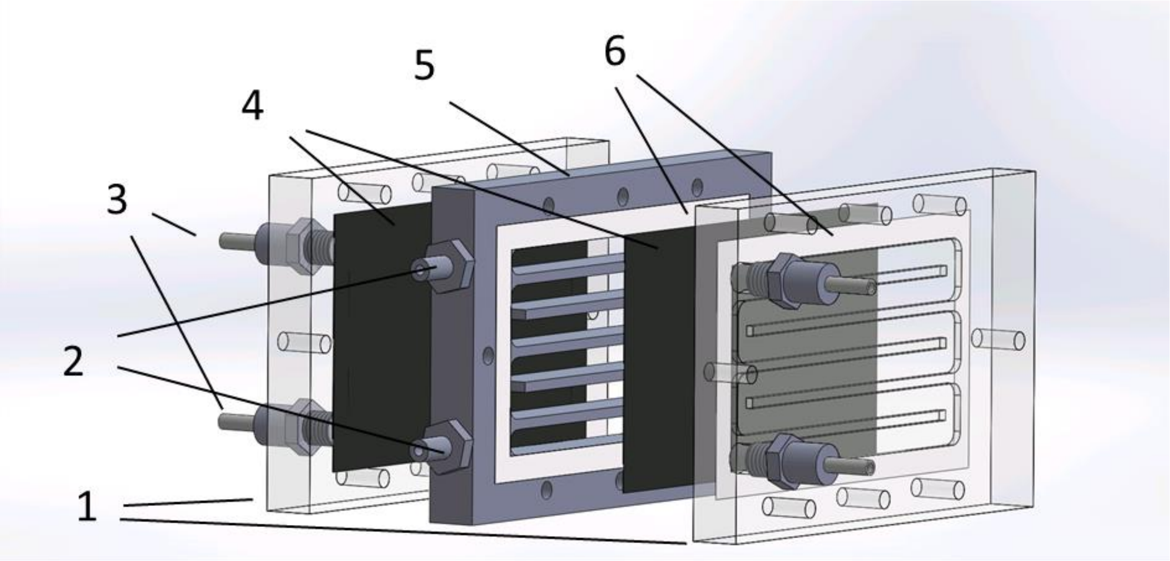

Figure 25: Schematic drawing of the plate heat exchanger for temperature control: (1) 20 mm PP-H heat exchanger side part, (2) G1/4” treaded screw-in 8 mm nozzle, (3) G1/4” treaded screw-in for DN04/06 tubings, (4) 0.3 mm carbon fiber composite (CFC) foil, (5) 20 mm PP-H heat exchanger mid part, and (6) epoxy bonding. Reproduced with permission from supporting information of reference.[57]

3.4.4. Electrolyte Tanks

The electrolyte tanks (c.f., (9) in Figure 22) are two containers consisting of a PMMA cylinder and a PVC-U lid and base part (c.f., Figure 26). The cylinder is sealed via two FKM O-rings sitting in grooves in the lid and base and pressing against the cylinder outside walls. This way, the construction holds overpressures of approx. 2 bar. The base part provides inlets and outlets for nitrogen gas (N_2) and electrolyte. During operation, both sides of the electrolyte can be gassed with N_2, flushing dissolved oxygen from the electrolyte to prevent oxidation of V^{2+}. For flushing, the lids are open.

In contrast, for a change of electrolyte, the lids are closed. Thereby, the N_2 pressure is used to press the electrolyte out of the tubing altogether. For this purpose, the tanks are closed at the lids by a locking screw and pressurized to about 0.5 bar. By means of 3-way valves (EM-Technik), the tanks and the various electrolyte circuits can be pneumatically drained of electrolyte.

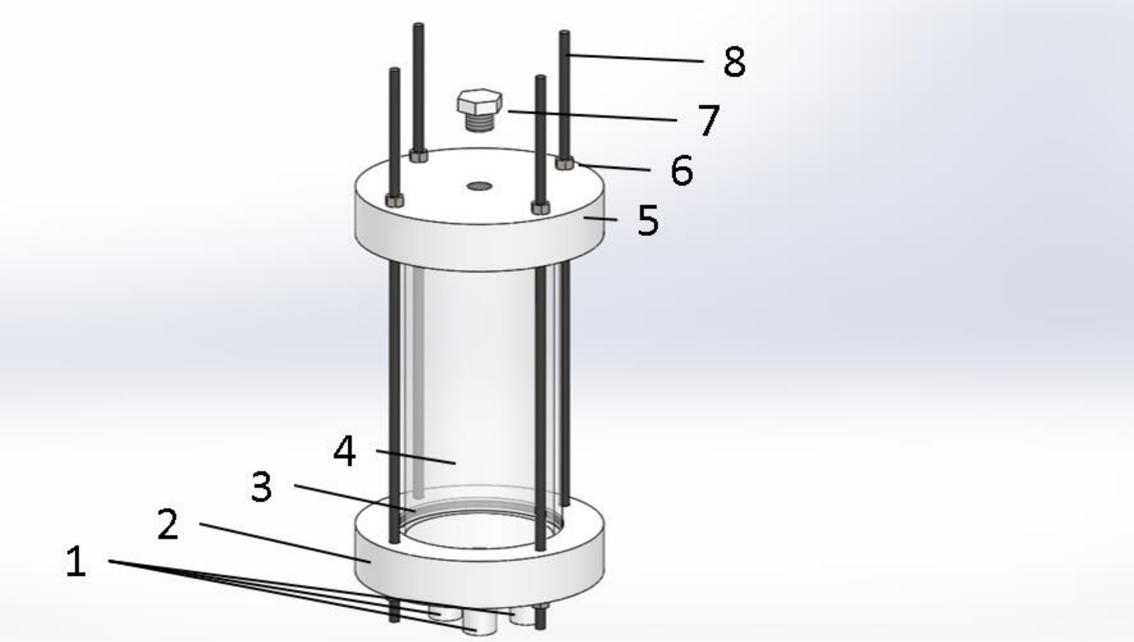

Figure 26: Schematic drawing of the electrolyte tank: (1) threaded screw-in for DN04/06 tubings, (2) PVC-U base part, (3) 3x50 FPM O-ring, (4) PMMA wall, (5) PVC-U lid part, (6) M6 nut, (7) PP locking screw, and (8) threaded M6 rod.

A pressure gauge (c.f., (10) in Figure 22) measures the differential pressure between the in- and outlet of the cell. The cell current-voltage characteristics and its impedance are measured by a PGSTAT potentiostat (c.f., (11) in Figure 22) (e.g., Metrohm Autolab).

3.4.5. Test Station Profile

The entire test environment is integrated into an in-house designed rollable construction of aluminum profiles (ITEM). In Figure 27, all central parts are described in the figure caption with respect to the numbers in the figure. The construction encloses all electrolyte-carrying components, which sit in a PVC-U tray that would contain any electrolyte leakage. At the top and at the sidewalls, transparent polycarbonate windows protect nearby personnel and equipment from damage that might be caused by the corrosive electrolyte.

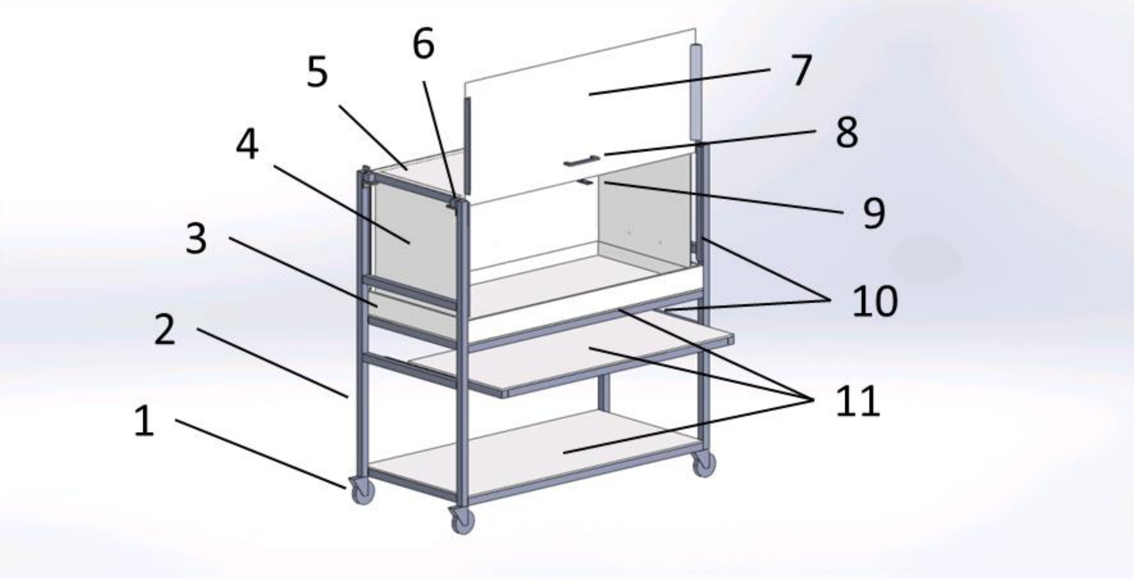

Figure 27: Test station profile construction with polycarbonate (PC) enclosure of all electrolyte-carrying components. The central parts are as follows: heavy-duty rollers (1), aluminum profile side braces (2), PVC-U drip tray (3), polycarbonate (PC) side walls (4), PC top wall (5), aluminum angle (6), PC front wall (7), aluminum handle (8), aluminum locking plate (9), telescopic slides (10), highly-pressurized laminate (HPL) boards (11).

3.5. Short Galvanostatic Cell Polarization with Full Single Cells

Short galvanostatic cell polarization (*short-GCP*) is a technique to measure the voltage response of a full single cell at constant charging or discharging currents. To illustrate the overvoltages for full-cells more clearly, Figure 28a shows experimental results of a controlled, alternating charge and discharge current density, with the corresponding cell voltages given in Figure 28b. The cell is charged and discharged galvanostatically at a continuous electrolyte flow rate of $100\ \mathrm{ml\,min^{-1}}$ at 50% *SoC* at different current densities. The resulting cell voltage is measured over time until a quasi-stationary cell voltage is obtained. The measurement intervals of 30-90 s are short enough so that the *OCV* (cyan line) does not change due to the continuous reactant transfer but remains at a constant level of 1.413 V, corresponding to 50% *SoC*. The cell voltage corresponds to the difference in electrode potentials modeled in Figure 10, including the Donnan potential (c.f., Eq. (18)).

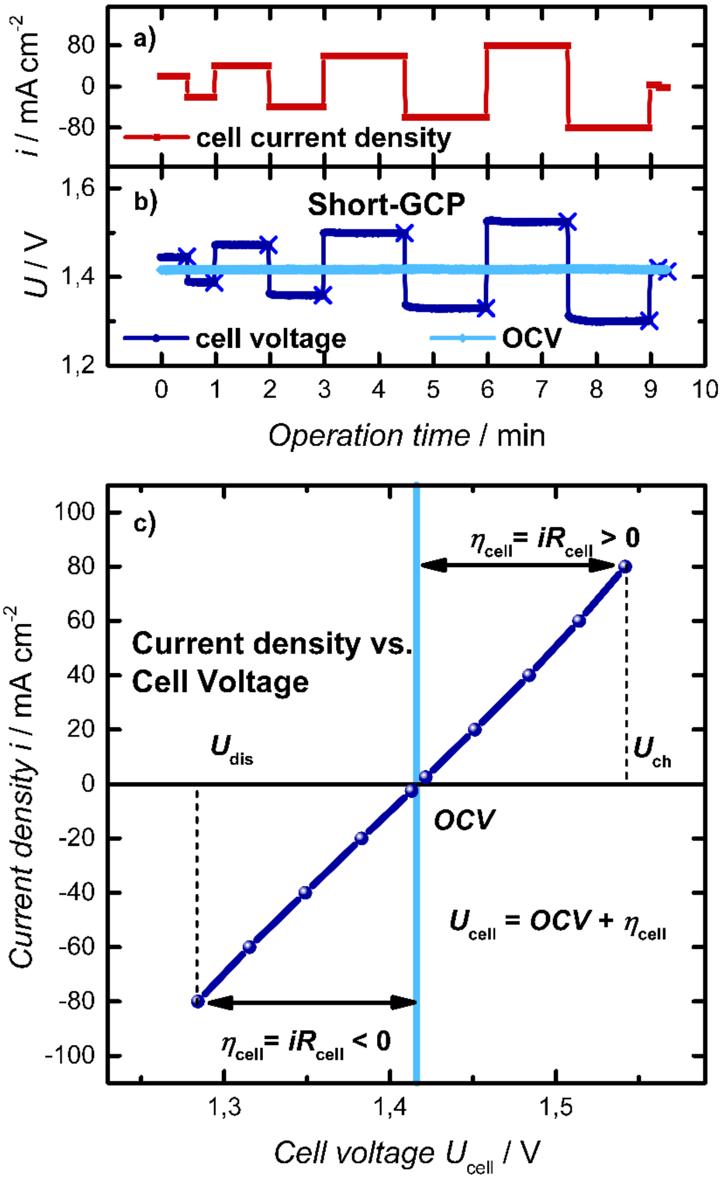

Figure 28: Experimental data of short galvanostatic cell polarization (*short-GCP*) of a typical VRFB full single cell with continuous electrolyte flow of 100 ml min^{-1} (1.6 M vanadium dissolved in 2.0 M aqueous sulfuric acid) at 50% *SoC*, an electrolyte temperature of 20°C: a) constant current charging and discharging at different current densities (red), and b) resulting cell voltages (blue). After 30-90 s, the cell voltage was constant and assumed quasi-stationary. The *OCV* of 1.41 V (light blue) indicated an *SoC* of 50%. c) Plot of the current densities vs. the quasi-stationary cell voltage as the ratio of discharge over charge voltage U_{dis} and U_{ch}. a) and b) reproduced with permission from reference.[57]

Figure 28c shows the quasi-stationary and constant cell voltages that are established after a few minutes at each given current density. The *OCV* is marked by a vertical line (cyan). For quasi-stationary charge and discharge voltages, Eq. (55) simplifies and the voltage efficiency η_V is derived as $\eta_V = U_{dis}/U_{ch}$, as shown in Figure 29. Consequently, *short-GCP* offers itself as a time-efficient method to extract voltage efficiencies to compare the performance of different combinations of cell components.

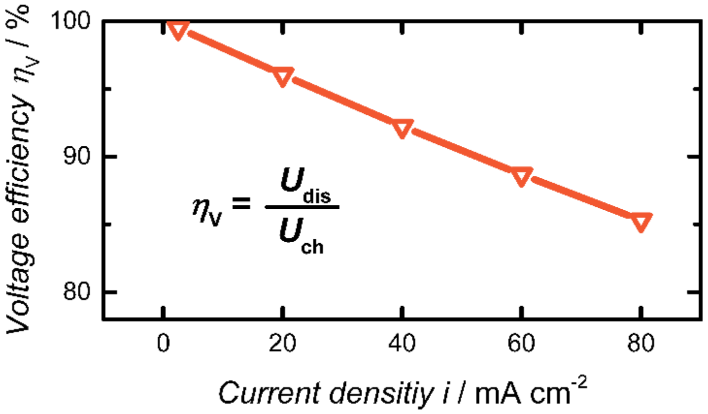

Figure 29: Voltage efficiency derived from short galvanostatic cell polarization (*short-GCP*) at charge-discharge current densities in the range of 0-80 mA cm^{-2}, determined from the data shown in Figure 28. Reproduced with permission from reference.[57]

3.6. Electrochemical Impedance Spectroscopy

Complementary to *short-GCP*, electrochemical impedance spectroscopy (*EIS*) can be used to identify the various cell resistances. *Short-GCP* probes the cell voltage U_{cell}, which is composed of the *OCV* and cell overvoltage η_{cell}:

$$U_{cell} = OCV + \eta_{cell} \tag{63}$$

Here, η_{cell} contains the partial contribution of the ohmic, kinetic, and concentration overpotentials at the anode and cathode, as well as the membrane overpotential:

$$\eta_{cell} = \eta_{\Omega,an} + \eta_{kin,an} + \eta_{c,an} + \eta_{\Omega,m} + \eta_{c,cat} + \eta_{kin,cat} + \eta_{\Omega,cat} \tag{64}$$

Similarly, the area-specific cell resistance is defined as $R_{cell} = \eta_{cell}/i$ and is the sum of its ohmic, charge-transfer and concentration partial resistances

$$R_{cell} = R_{\Omega,an} + R_{ct,an} + R_{c,an} + R_{\Omega,m} + R_{c,cat} + R_{ct,cat} + R_{\Omega,cat} \tag{65}$$

During *short-GCP*, the cell reveals its quasi-stationary current-voltage-dependence after a particular equilibration time.

In contrast, potential-controlled *EIS (PEIS)* measures the current response while sinusoidally perturbing the voltage around a constant value at a certain amplitude and frequency. From the transient current and voltage, the complex impedance Z can be determined. Plotting the real part *Re(Z)* of the impedance vs. its negative imaginary part *-Im(Z)* over the range of the applied perturbation frequencies results in the Nyquist plot shown in Figure 30. This Nyquist plot features two semi-circles. The greatest advantage of this representation is that the extrapolated intersections with the *Re(Z)*-axis indicate the partial cell resistances according to Eq. (65). The electronic and ionic conduction and transport processes occur in different characteristic frequency ranges. Thus, modulating the frequency allows discriminating the resistance for ohmic conduction R_{Ω}, kinetic charge transfer R_{ct}, and diffusive mass transport R_{c} separately.

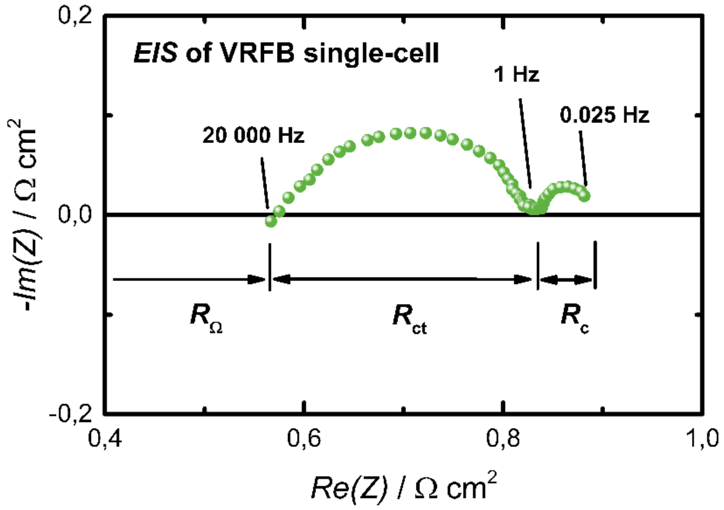

Figure 30: Nyquist plot for a typical potential-controlled electrochemical impedance spectroscopy *(PEIS)* measurement of a VRFB full single cell with continuous electrolyte flow of 100 ml min^{-1} (1.6 M vanadium dissolved in 2.0 M aqueous sulfuric acid) at 50% *SoC*, an electrolyte temperature of 20°C. The two semi-circles show intercepts with the real part impedance *Re(Z)* axis, indicating the partial resistances responsible for ohmic, kinetic, and concentration voltage losses. Reproduced with permission from reference.[57]

Figure 32 illustrates an equivalent circuit with capacitors and resistances accounting for the internal cell processes. The equivalent circuit features the same electrical characteristics as the battery cell and can be used to model the battery behavior. $R_{\Omega,\mathrm{an}}$, $R_{\Omega,\mathrm{cat}}$, and $R_{\Omega,\mathrm{m}}$ stand for the ohmic resistances in the anode, cathode, and membrane, respectively. The situation at the anode surface resembles the parallel connection of a capacitor $C_{\mathrm{dl,an}}$ and a resistor $R_{\mathrm{ct,an}}$; electrons move due to the formation of a capacitive double-layer and due to the resistive charge transfer upon the V^{2+}/V^{3+} redox reaction.

However, the double-layer does not behave like an ideal capacitor. Instead, it is found to be better described by a constant phase element (CPE), i.e., $Q_{\mathrm{dl,an}}$, accounting that the electrodes are to be seen as a multitude of parallel capacitors, all contributing simultaneously but to a different extent.[123] Accordingly, the cathode surface is represented by the parallel combination of $Q_{\mathrm{dl,cat}}$ and $R_{\mathrm{ct,cat}}$. As a third category, the dashed rectangles contain two parallel R-CPE elements on the anode and cathode sides characterized by $Q_{\mathrm{c,an}}$, $R_{\mathrm{c,an}}$, $Q_{\mathrm{c,cat}}$, and $R_{\mathrm{c,cat}}$. These elements account for the finite-length Warburg (FLW) impedance and mimic the diffusional mass transport due to concentration gradients from the electrolyte bulk to the electrode surface.[124,123]

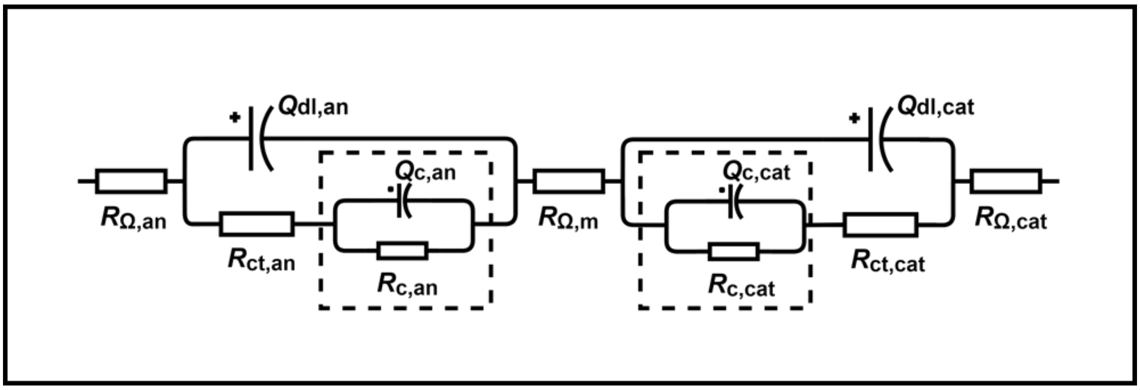

Figure 31: Equivalent circuit simulating the impedance of a VRFB single cell. Circuit elements are the ohmic conduction resistances ($R_{\Omega,\mathrm{an}}$, $R_{\Omega,\mathrm{cat}}$, and $R_{\Omega,\mathrm{m}}$), the charge-transfer resistances ($R_{\mathrm{ct,an}}$, and $R_{\mathrm{ct,cat}}$), concentration resistances ($R_{\mathrm{c,an}}$ and $R_{\mathrm{c,cat}}$) and CPEs ($Q_{\mathrm{c,an}}$ and $Q_{\mathrm{c,cat}}$) due to the concentration gradient of reactant from the bulk electrolyte to the electrode surface, and CPEs ($Q_{\mathrm{dl,an}}$ and $Q_{\mathrm{dl,cat}}$) accounting for the double-layer.

Depending on the *EIS* modulation frequency, different electronic and ionic current paths establish. At high frequencies around 20 000 Hz, the cell voltage modulation is so fast that the impedance of the capacitors goes towards zero. The resulting apparent cell resistance is the sum of all ohmic resistances $\sum R_{\Omega}$ highlighted in blue in Figure 32a. At frequencies around 1 Hz, the impedance of the double-layer capacitors become relatively large, so that they approach the behavior of an insulator. However, the charge transfer from the redox reactions contribute to the current through anode and cathode, which is characterized by the charge transfer resistances $\sum R_{\mathrm{ct}}$ highlighted in green in Figure 32b. At frequencies smaller than 0.025 Hz, the continuous charge transfer leads to reactant depletion at the electrode surface. The resulting diffusive mass transport across the Nernst diffusion layer from the electrolyte bulk to the anode and cathode surfaces causes additional concentration resistances $\sum R_{\mathrm{c}}$ highlighted in red in Figure 32c.

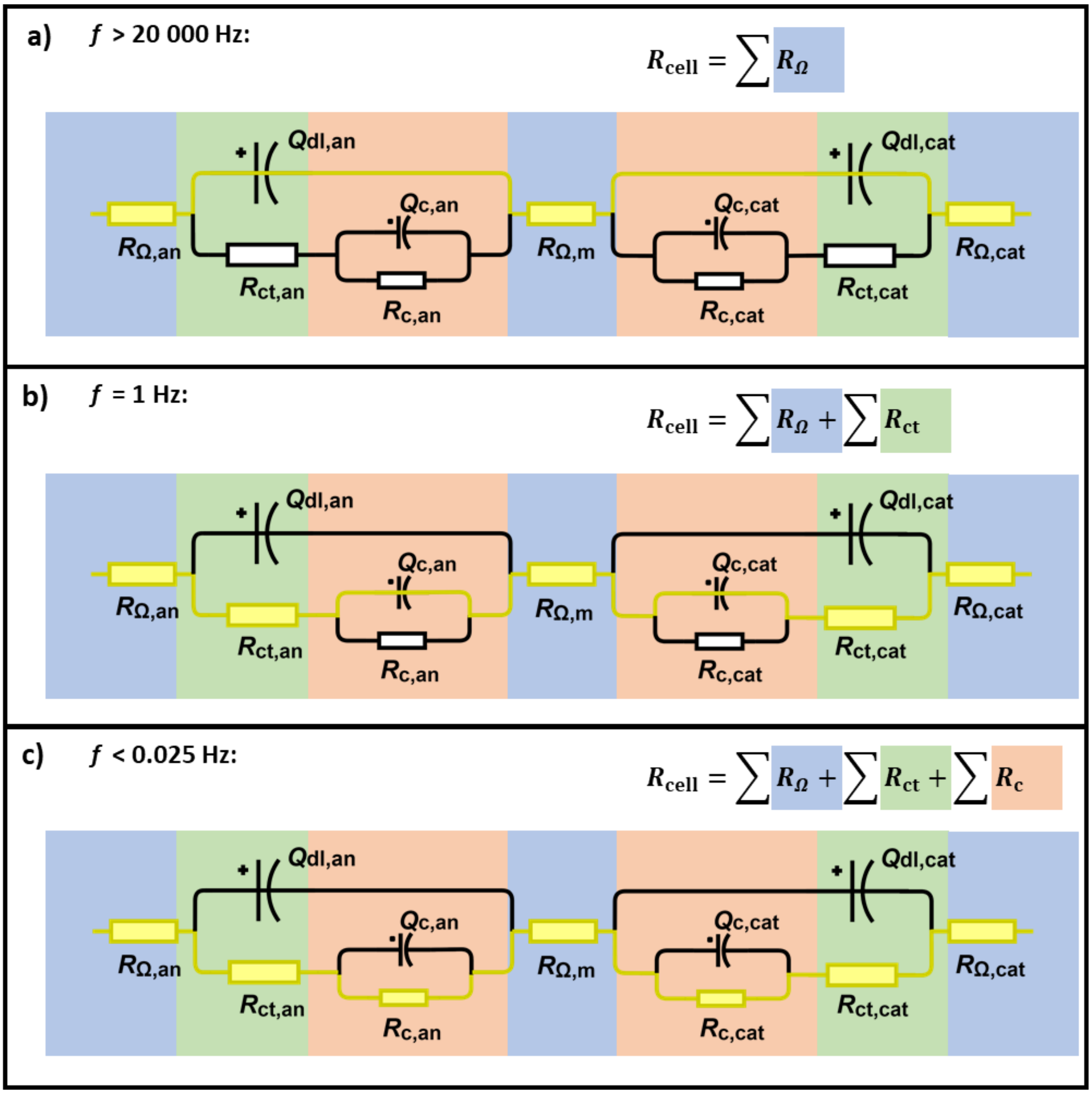

Figure 32: Frequency-dependent charge transport paths, illustrating the partial resistances for ohmic conduction, kinetic charge transfer, and diffusive mass transport. The three layers represent the electronic and ionic current paths for different *EIS* frequencies. a) At high frequencies around 20 000 Hz, the cell resistance contains only ohmic contributions (blue) from electrons moving through the anode and cathode $R_{\Omega,\mathrm{an}}$ and $R_{\Omega,\mathrm{cat}}$, and from ions moving through the membrane $R_{\Omega,\mathrm{m}}$. b) At moderate frequencies around 1 Hz, the resistance includes the charge-transfer resistances (green) for the anode and cathode reactions $R_{\mathrm{ct,an}}$ and $R_{\mathrm{ct,cat}}$. c) At low frequencies around 0.025 Hz, the voltage modulation is slow enough for the development of a concentration profile from the electrolyte bulk to the electrode surface. Consequently, in addition to ohmic and charge-transfer resistances, the cell comprises the concentration resistances $R_{\mathrm{c,an}}$ and $R_{\mathrm{c,cat}}$ (red).

3.7. Scanning Electron Microscopy

Scanning electron microscopy (*SEM*) was used to study the surface structure of the graphite fiber electrodes (c.f., Figure 16). Thereby, electrons are focused in a beam and accelerated in an electric field to kinetic energies of 10-12 keV. When hitting the sample under investigation, the electrons interact with the atoms of the sample and release secondary electrons, analyzed by an electron detector. The detected electron intensity provides information about the topography of the sample, providing a magnification of 10^5.[125]

3.8. X-Ray Photoelectron Spectroscopy

X-ray photoelectron spectroscopy (*XPS*) was used to investigate the surface atomic composition, which primarily referred to the surface amount of oxygen (O) and carbon (C). As a working principle, a monochromatic Al K_α-source is used to direct X-rays with known energy ($\mathrm{E}_{\mathrm{photon}} = 1486.7\ \mathrm{eV}$) towards the sample. The X-rays excite photoelectrons from atoms in the sample within a penetration depth of several µm, which is, however, much higher than the escape depth of the generated photoelectrons. Consequently, only photoelectrons released from surface atoms within a depth of 1-3 nm reach the outside of the sample, where they are probed by an electron energy analyzer and an electron detector.[126] For this reason, *XPS* is, in general, sensitive to the bonding relations of atoms on the surface and, thus, is employed to analyze the type of oxygen surface group, such as carbonyls (CO), carboxyls (COOH), or hydroxyls (COH).[54] However, this analysis strongly depends on line shape and background used for fitting the *XPS* data. Moreover, the spectra of the samples assayed in this work appeared almost identical. As a result, the *XPS* analysis in this work focused not on individual oxygen species but on the integral O/C ratios.[57]

3.9. Krypton and Nitrogen Adsorption Analysis

The two techniques of nitrogen and krypton adsorption were used to determine the specific surface area of the graphite felt electrodes. Both techniques refer to the Brunauer-Emmett-Teller (*BET*) theory and are based on the same principle, namely that a probing gas is brought in contact with the sample. At the N_2 boiling temperature of 77 K, being below the saturation vapor pressure p_0, the molecules of the probing gas, i.e., N_2 or Kr, are allowed to adsorb physically to the surface of the solid sample material. When decreasing the pressure, the adsorbed gas is partly desorbing from the surface. Within the relative pressure $p/p_0 = 0.05 - 0.35$, the amount of desorbing gas, thereby, is proportional to the surface area.[127] In this work, nitrogen adsorption was unsuitable, as it comprised too low sensitivity for small inner surfaces around 1 m^2 g^{-1}. Instead, krypton adsorption proved to be by far more efficient in precisely resolving the low inner surface areas of the carbon electrodes.

4. Results

This chapter presents the journal articles written over the course of this PhD thesis. The first article in Section 4.1 systematically investigated how thermal treatment in air at 400°C enhances the performance of graphite felt electrodes – and why. This study revealed that all electrodes showed the commonly observed phenomenon of performance degradation, even though the effect was less pronounced for electrodes with a larger electrochemically active surface area (*ECSA*). The second article in Section 4.2 proposes a new surface reaction mechanism, explaining the performance degradation and implying operational strategies to improve the long-term electrode performance.

4.1. Impact of Plasma and Thermal Treatment on the Long-term Performance of Vanadium Redox Flow Electrodes – Significance of Surface Structure vs Oxygen Functionalities

The article "Impact of Plasma and Thermal Treatment on the Long-term Performance of Vanadium Redox Flow Electrodes – Significance of Surface Structure vs Oxygen Functionalities"[57] was submitted in April 2021 and published as an open-access article in the peer-reviewed *Journal of the Electrochemical Society* in June 2021. The article was distributed under the terms of the Creative Commons Attribution 4.0 License (CC BY), which permits unrestricted reuse of the work in any medium, provided the original work is properly cited. The permanent weblink to the article is https://doi.org/10.1149/1945-7111/ac163e.

Typically, graphite felt electrodes comprise a large charge-transfer resistance for the V^{2+}/V^{3+} redox reaction that is compromising the cell voltage efficiency. Several different surface modification strategies are suggested in the literature. Surface oxides are claimed to lead to a high electrode wettability and provide a high catalytic activity for the performance-critical V^{2+}/V^{3+} reaction. For this publication, a 25cm^2 single-cell design was developed, as well as a testing environment that enabled stable system operating conditions with respect to electrolyte flow rate, temperature, and *OCV* (c.f., Section 3.4). With the reproducible single-cell assembly procedure and the highly stable system operating conditions, the performance of the GFD4.6 graphite felt electrode material from SGL could be investigated precisely and systematically. We applied a low-pressure plasma treatment to form surface oxides on the electrode, thereby giving it a good wettability and presumably an improved catalytic activity. Successively, the electrodes were exposed to thermal treatments of different durations at 400°C in an air atmosphere. Repetitive in-situ *EIS* and *short-GCP* diagnostics were used to compare the electrochemical performance during the first 20 hours of steady-state cell operation. The data were expressed in terms of the charge-transfer resistance R_{ct} as well as the voltage efficiency η_{V}. The study revealed that plasma treatment and the resulting high concentration of surface oxides, confirmed by *XPS*, did not lead to significant electrode performance improvements. Instead, the additional thermal activation in air enhanced the VRFB electrode performance significantly, which strongly corresponded with the treatment duration. Over time, the surface structure roughened, and its surface area increased, as was shown by *SEM* and krypton adsorption measurements. In conclusion, the thermal treatment is not effective because of generating surface oxides, but rather because of inducing surface corrosion, forming electrochemically active carbon edge sites.

Moreover, over 24 h of idle operation of the battery, the performance degradation due to deteriorating anode kinetics decreased drastically with increasing thermal treatment times. GFD-HT, i.e., a heat-treated, commercially available, and high-performing GFD4.6 material, comprised the highest surface activity and high apparent performance stability. Consequently, GFD-HT was monitored during extended idle battery operation of 400 h. Due to the stable measurement conditions, over the 400 h, a pronounced performance degradation could be determined, manifesting in an increased charge-transfer resistance from 0.1 to 0.4 $\Omega\,\mathrm{cm}^2$. The yet unclear reason for the kinetics degradation was the subject of the second article described below.

Author contributions

T.G. developed the VRFB single-cell design and the cell test environment. T.G. prepared the plasma and thermal electrode treatment, performed the electrochemical investigation and validation, and evaluated the experimental results. T.G. developed the concept, the methodology, and visualization and wrote the manuscript. P.T. performed the *XPS* measurements and data analysis and edited the manuscript. D.M. performed the

Kr adsorption measurements and data analysis. M.W. performed the *SEM* measurements. T.G., P.T., D.M., P.D., M.W., and G.D. discussed the experimental results and revised the manuscript.

Journal of The Electrochemical Society, 2021 **168** 070554

Impact of Plasma and Thermal Treatment on the Long-term Performance of Vanadium Redox Flow Electrodes – Significance of Surface Structure vs Oxygen Functionalities

Tobias Greese,[1,*,z] **Paulette A. Loichet Torres,**[2,*] **Davide Menga,**[2,*] **Petra Dotzauer,**[1] **Matthias Wiener,**[3] **and Gudrun Reichenauer**[3]

[1] *ZAE Bayern, Electrochemical Energy Storage, 85748 Garching, Germany*
[2] *Chair of Technical Electrochemistry, Department of Chemistry and Catalysis Research Center, Technical University of Munich, 85748 Garching, Germany*
[3] *ZAE Bayern, Nanomaterials, 97074 Würzburg, Germany*

Graphite felt (GF) electrodes of vanadium redox flow batteries show enhanced performance when thermally treated before their assembly. Thermal treatment works by simultaneously increasing electrode wettability, kinetic activity, and total surface area (TSA). This study examines these performance determining yet inseparable effects, especially considering the electrodes' long-term operation. We exposed GF electrodes to 5 min plasma treatment, ensuring equal wettability, and thermally treated them in air at 400 °C for different durations. We then linked the resulting GF surface structure with the electrode performance, monitored with a high temporal resolution, and controlled electrolyte conditions. The performance, expressed in charge-transfer resistances and voltage efficiencies, correlated accurately with the thermal treatment times. According to XPS, against expectation, the thermal treatment decreased the number of surface oxygen functionalities. Instead, SEM and krypton adsorption revealed that the surface had become rougher, and the TSA increased. Upon corrosion, the surface presumably exposed more carbon edge sites being catalytically active, explaining the improved performance. Therefore, compared with the commonly suggested surface oxygen enrichment, increasing the GF surface roughness and TSA may be the more promising strategy to enhance and stabilize the long-term VRF electrode performance.

[DOI: 10.1149/1945-7111/ac163e]

Manuscript submitted April 7, 2021; revised manuscript received June 24, 2021. Published July 28, 2021.

Supplementary material for this article is available online

Vanadium redox flow (VRF) batteries store electrical energy environmentally friendly since they employ sustainable materials and promise a long lifetime. For finding widespread use, the batteries must prevail in a competitive market having minimum investment costs. However, realized are minimum investment costs only with an optimized battery cell performance. The cell performance strongly depends on the carbon electrodes, which commonly consist of graphite felt (GF) material. Hence, modifying this GF material bears immense improvement potential for the cell and battery performance.[1–3] Many different modification techniques have evolved, typically oxidizing the electrode material relying on chemical,[4,5] electrochemical,[6–9] plasma,[10–12] or thermal treatment.[13–16] Upon oxidation, the electrodes present a substantially enhanced charge-transfer kinetics for the V^{2+}/V^{3+}-reaction, which is the dominating cause for the charge-transfer cell resistance, as opposed to the VO^{2+}/VO_2^{+}-reaction.[17–19]

The thermal treatment proved to be the most feasible technique with the least processing expenditure, having multiple benefits for the electrode performance. The high temperatures paired with the atmospheric oxygen lead to partial oxidation of the graphite fibers, introducing oxygen-containing surface functional groups. Li et al. attributed the improved V^{2+}/V^{3+}-kinetics to oxygen-containing C–OH groups increasing upon thermal treatment in air at 400 °C for 30 h.[20] Similarly, Dixon et al. compared thermally–with plasma-treated graphite electrodes. Low-pressure oxygen plasma treatment (4 min at 60 W generator power) resulted in a higher V^{2+}/V^{3+}-activity than the thermal treatment at 400 °C, reached by a 5 °C min^{-1} heating rate. Their N_2-*BET* analysis revealed no increased surface area, so they concluded that the enhanced activity must have resulted from the increased C–OH surface functional groups.[10]

Moreover, thermal treatment increases the electrode wettability. Thereby, oxygen functionalities render the fiber surface polar, so the electrode can better saturate with the aqueous electrolyte. Releasing air pockets otherwise enclosed,[21] the electrode-to-electrolyte contact area increases, leading to a larger electrochemically active surface area (ECSA).[22,23] Furthermore, the atmospheric oxygen the treatment involves partially leads to carbon combustion corroding the surface. While the enhanced surface roughness further increases the ECSA, Chu et al. observed that graphite fiber corrosion induced by air oxidation increases the EC surface activity disproportionally with ECSA. Accordingly, this is due to the introduction of carbon edge plane sites. As opposed to carbon basal plane sites, edge plane sites comprise a much higher catalytic activity for EC reactions. Consequently, the surface provides more EC-active sites, implicating both a larger and more active ECSA.[24]

The trends toward oxygen groups, wettability, surface roughness, and carbon edge sites coincide. Consequently, it has not been possible to identify the thermal treatment's primary benefit for the performance. Providing that the electrodes comprised complete wettability, we pursued this issue, asking *'How is the surface of the carbon fibers affecting the electrode performance, especially in the long-term operation?'*.

Long-term performance is of particular interest since the GF electrode activity continuously degrades, leading to increased cell overpotentials. In specific, responsible for the increased overpotentials is the electrode sustaining the V^{2+}/V^{3+}-reaction, showing deteriorating reaction kinetics leading to increasing charge-transfer resistance (R_{ct}).[25–29] In a recent study, we proposed a degradation mechanism being in line with the observed electrode behavior and explaining how the kinetics could decrease over a given time of operation. In short, V^{2+} is assumed to adsorb onto the anode surface during operation with a V^{2+}/V^{3+}-electrolyte, leading to the suggested kinetics deterioration and observed performance degradation.[30] In previous research of different groups, identified drivers for degradation are the charging terminal voltage,[25] electrolyte temperature,[27] electrolyte state-of-charge, and (geometric) electrode current density.[28] However, only a few selective studies assayed treatment techniques,[25,29,31] concluding that electrodes degrade less when thermally treated than in their original form.

---

[*] Electrochemical Society Student Member.
[z] E-mail: Tobias.greese@zae-bayern.de

Accordingly, for systematically modified electrode surfaces, the long-term performance has not yet been under examination.

Consequently, this study investigates how thermal treatment influences electrode activity degradation. The evaluated GF electrodes were pre-treated with plasma before the thermal treatments. This pre-treatment ensured complete electrode wettability, minimizing air inclusions compromising the electrode ECSA. Consequently, in focus is how thermal treatment alters the surface structure, enhancing and stabilizing the electrode performance. Accounting for the continuous performance degradation, we studied the performance not at a given point in time but repetitively over cell operation. For a high temporal resolution of the performance evolution, we required electrochemical techniques that are suitably fast and reliable. Therefore, we repeatedly performed short galvanostatic cell polarization (*short-GCP*). At constant charging and discharging currents at 50% state-of-charge (*SoC*), we measured the cell voltages and derived the corresponding temporary voltage efficiencies. Also, for resolving the altering R_{ct} over time, we employed repetitive potentiostatic electrochemical impedance spectroscopy (*PEIS*). Complementary, we examined the fiber surface structure qualitatively using scanning electron microscopy (*SEM*). Additionally, we used X-ray photoemission spectroscopy to determine the concentration of oxygen groups on the carbon surface, commonly expected to be primarily responsible for catalyzing the vanadium reactions. Moreover, we probed the fiber *TSA* quantitatively using krypton adsorption.

We demonstrate that plasma treatment resulting in a complete electrode wettability and high surface oxygen concentration will not deploy a cell performance for a technical application. Moreover, due to the preceding plasma treatment, the additional thermal treatment did not introduce but instead decrease the oxygen-containing functional groups. After all, the missing correlation of surface activity and oxygen groups questions the general concept that oxygen functionalities are primarily responsible for catalyzing the V^{2+}/V^{3+}-reaction. Instead, the commonly observed increase in functionalities during thermal treatment may only coincide with the concomitant activity increase. In this study, despite decreased oxygen functional groups, the yet enhanced surface activity instead correlated with increased surface roughness and *TSA*, indicating an increase in EC-active carbon edge sites. The resulting *TSA* was decisive not only for enhancing the electrode performance but also for stabilizing it in the long-term cell operation.

Experimental

Electrode modification.—We established equal electrode wettability to investigate how the electrode performance responded exclusively to surface structure alteration. Figure 1 outlines how the electrodes were modified. The electrode material GFD4.6 (SGL Carbon, Germany) is a graphite felt resulting from graphitizing a poly-acrylonitrile (PAN) precursor and consists of 99% graphitic carbon. Figure 1a illustrates the felt material in different magnifications. It reveals its porous structure defined by graphite fibers with a diameter from 8–10 μm. Natively, the graphite fiber surface is non-polar and hydrophobic.

Consequently, when the aqueous, polar electrolyte flows through the electrode, gas inclusions may be trapped[21] and cause the ECSA to differ randomly from electrode to electrode.[23] Mazur et al. reported graphitic electrodes inhomogeneously wettable even after being thermally treated in air at 400 °C for 9 h.[24] As a result, with insufficiently wettable electrodes, it was impossible to reliably correlate the surface structure with the resulting cell performance. Therefore, we pre-treated all GFD4.6 electrodes for 5 min in a PlasmaFlecto 10 low-pressure plasma chamber (Plasma Technologies GmbH, Germany). The chamber was operated with an air atmosphere at 0.3 mbar pressure and 300 W generator power. After the plasma treatment, the electrodes absorbed the electrolyte completely, proving their comprehensive wettability. In the next step, we transferred the electrodes to a preheated KDF-75 box-type furnace (DENKEN-HIGHDENTAL Co., Ltd., Japan) and thermally treated them in air at 400 °C for defined durations of 0, 3, 6, 12, 18, and 24 h. Figure 1b gives an overview of all electrode samples and their modification procedure. In addition to the in-house modified samples (GF-0h to −24h), we examined the electrode material GF-HT (SGL Carbon, Germany) as a reference. GF-HT is a commercially available variant of GFD4.6 thermally treated by the supplier (not further specified) and used as received throughout this study.

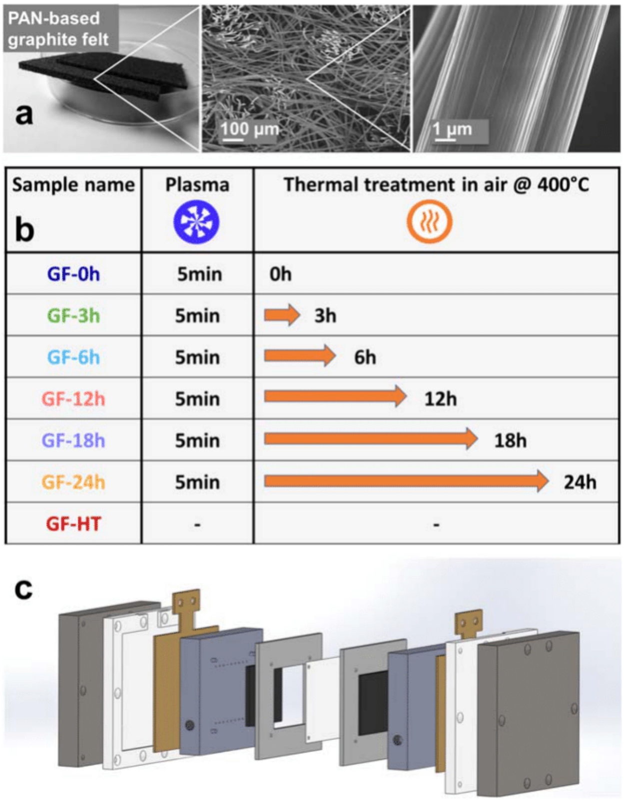

Sample name	Plasma	Thermal treatment in air @ 400°C
GF-0h	5min	0h
GF-3h	5min	3h
GF-6h	5min	6h
GF-12h	5min	12h
GF-18h	5min	18h
GF-24h	5min	24h
GF-HT	-	-

Figure 1. (a) Unmodified PAN-based graphite felt electrode appearing at different length scales. (b) A chart summarizing the performed electrode modifications and the respective sample denotation. For instance, the label GF-24h refers to the graphite felt GFD4.6 that was plasma-treated for 5 min and thermally treated in air at 400 °C for 24 h. (c) Single-cell assembly used for electrode performance tests.

Single-cell assembly.—For probing the electrochemical performance of the modified electrodes, we employed a VRF single-cell depicted in Fig. 1c. The cell applied the flow-through design with a geometric electrode area of 25 cm^2. The membrane material was $\text{Nafion}^{\text{TM}}$ NF212, and monopolar plates were made from an injection-molded graphite-polypropylene composite being chemically inert. The current collectors were gold-coated copper plates. A detailed description of all cell components is available in the supporting information (SI) in Fig. SI 1 (available online at stacks.iop.org/JES/168/070554/mmedia).

Test environment.—As we intended to study how the cell performance changed with the electrode properties rather than the electrolyte, we designed the test environment to keep the electrolyte parameters as stable as possible. Thus, we avoided any possible degradation caused by the electrolyte, eventually affecting the cell performance otherwise. Essential parameters were the electrolyte *SoC*, flow rate, and temperature. We monitored the *SoC* using the open-circuit voltage (*OCV*) by an *OCV* cell (BELLTEC, Germany). Moreover, we automatically adjusted the electrolyte flow rate and the electrolyte temperature. Unless stated otherwise, we recorded all measurements at an electrolyte temperature of $T = 20 \pm 0.2$ °C and a flow rate of $FR = 100 \pm 2\ \text{ml min}^{-1}$. A schematic of the hardware and a detailed functional description is also available in the SI in Fig. SI 2. The setup involved VZS005-PP in-line oval-wheel flowmeters (B.I.O.-TECH, Germany), in-line fluor-ethylene-propylene (FEP)-coated Pt100 thermometers (Fig. SI 3a), and an in-house designed plate heat exchanger (Fig. SI 3b). In addition, several NF60 membrane pumps (KNF Neuberger, Germany) were PID-controlled by a customized LabView logic.

Electrolyte preparation and measurement procedure.—The vanadium (V) electrolyte (GfE GmbH, Germany) was at a concentration of 1.6 M V dissolved in 2.0 M aqueous sulfuric acid (H_2SO_4) and ready for use in its uncharged form, referred to as $V^{+III/+IV}$. We pre-charged 500 ml of $V^{+III/+IV}$ to an *SoC* of 50%, corresponding to an *OCV* of 1.413 V[32] using a conditioning cell (with an arrangement identical to the test cell). After replacing the conditioning cell with the test cell, the measurement program started immediately after the electrolyte filled the electrodes within 30 s.

The program was a sequence of short galvanostatic cell polarization (*Short-GCP*) and potentio-electrochemical impedance spectroscopy (*PEIS*), represented in Fig. 2a as blue and red bars, respectively. The green periods in between mark the time defined as idle cell operation. During this time, the cell voltage was sustained at 1.42 V, so the cell counteracted the slow electrolyte self-discharge across the membrane.

In the *short-GCP*, we probed the cell voltage during a sequence of interchanging charging and discharging current densities $i = \pm$ 2.5, 20, 40, 60, and 80 mA cm^{-2}, as shown in Fig. 2b. The cell voltage U reached constant values for each current density after a settling time of 30–90 s. Meanwhile, the simultaneously recorded *OCV* did not change traceably, so the cell entered a quasi-stationary state. We used the respective last constant voltage value to calculate the round-trip voltage efficiency η_V of a short charge-discharge cycle (cf, Fig. 2c). The voltage efficiency, defined as the ratio of energy efficiency (η_E) over coulomb efficiency (η_C), corresponds to

$$\eta_V = \frac{\eta_E}{\eta_C} = \frac{\dfrac{\int U_{dis}(t)\, i(t)\, dt_{dis}}{\int U_{ch}(t)\, i(t)\, dt_{ch}}}{\dfrac{\int dQ_{dis}}{\int dQ_{ch}}} \qquad [1]$$

At a constant cell voltage and with $\int i(t)\,dt = \int dQ$, the voltage efficiency is the ratio of discharging (U_{dis}) over the charging voltage (U_{ch}).

$$\eta_V = \frac{\dfrac{U_{dis}\int dQ_{dis}}{U_{ch}\int dQ_{ch}}}{\dfrac{\int dQ_{dis}}{\int dQ_{ch}}} = \frac{U_{dis}}{U_{ch}} \qquad [2]$$

For reference, in Fig. SI 4, we plotted the *E*-*i*-curves from all of the cell voltages (U_{dis} and U_{ch}) measured throughout 20 h vs their current density.[1,33]

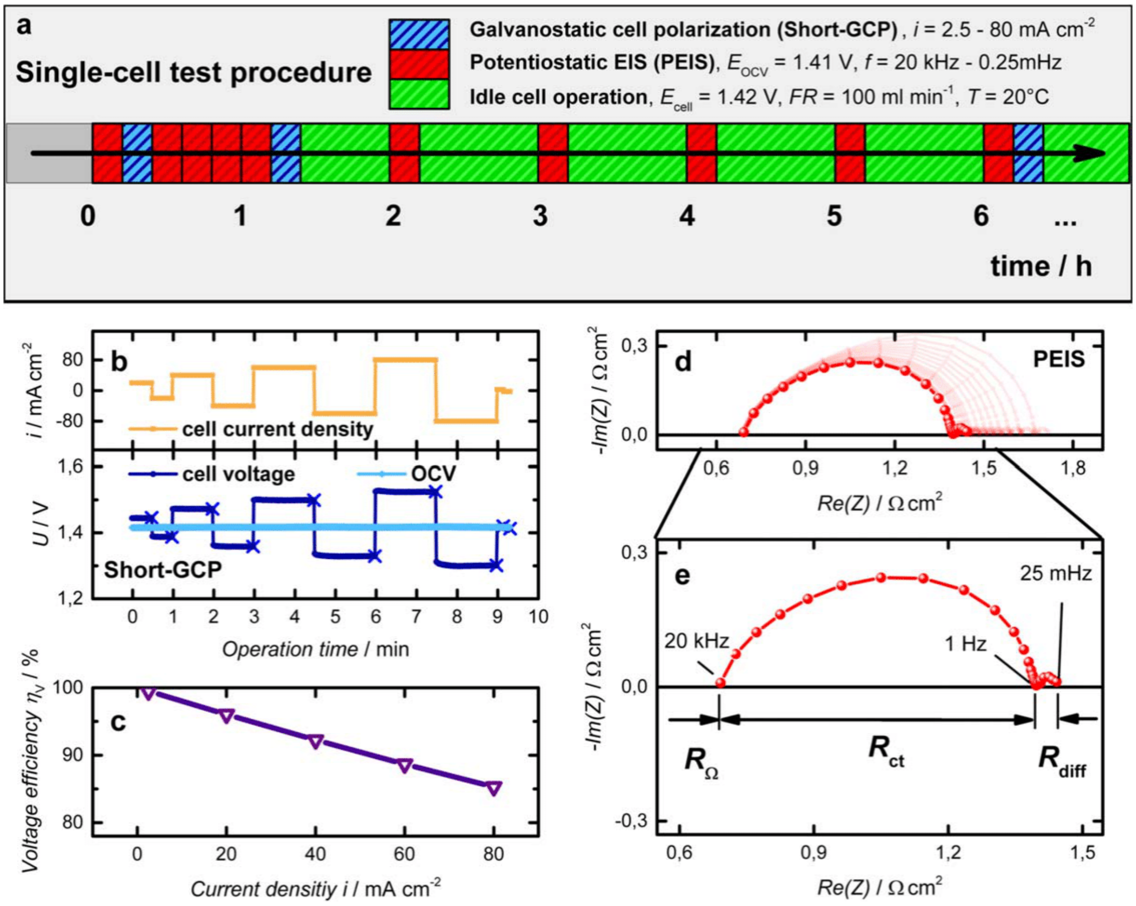

Figure 2. (a) Schematic visualization of the subsequent steps of the measurement procedure applied. (b) *Short-GCP* curves at current densities of i = ± 2.5, 20, 40, 60, 80 mA cm^{-2}. (c) Voltage efficiency derived from *short-GCP* cell voltages recorded for different current densities, according to Eq. 2. (d) Nyquist plots of an exemplary sequence of repetitive *PEIS* recorded throughout 20 h of idle cell operation. (e) For better inspection, the Nyquist plot of the first recorded *PEIS*. The voltage oscillated at an amplitude of 30 mV around *OCV* at frequencies ranging from 20 kHz - 25 mHz. The semi-circle intercepts with the Re(Z) axis illustrate how the partial resistances R_{Ω}, R_{ct}, and R_{diff} were derived.

Using *PEIS*, we analyzed the overall cell resistance, distinguishing the kinetic charge transfer from the ohmic and diffusional resistances. During *PEIS,* the voltage oscillated by 30 mV around *OCV* within the frequency ranging from 20 kHz to 25 mHz. One *PEIS* lasted about 10 min. Figure 2d shows the Nyquist plot of all *PEIS* measurements recorded over 20 h. In Fig. 2e, the first of these *PEIS* serves to illustrate the characteristic features used for analysis. The plot features two semi-circles. The first one showed intercepts with the real-part axis at 20 kHz and 1 Hz, while the second one formed between 1 Hz and 25 mHz. We tested in detail how the semi-circles responded to changed system settings, such as the electrolyte temperature ranging between 10 °C–35 °C (Figs. SI 5–7). The first semi-circle appears highly sensitive to temperature changes, while the second semi-circle mainly remained unaltered. Conversely, changing the electrolyte flow rate from 100–25 ml $\min^{-1}$ did not affect the first semi-circle. In contrast, the second semi-circle increased notably (Fig. SI 8). Also, we validated measurement settings such as the *PEIS* voltage oscillation amplitude (Fig. SI 9), ensuring to stay in the linear current-potential region.

On this basis, we identified the intercept of the first semi-circle with the real-part impedance axis at 20 kHz in Fig. 2e to indicate the partial resistance for ohmic conductance (R_Ω). At lower frequencies, the first semi-circle diameter between 20 kHz and 1 Hz shows the reaction kinetics resistance R_{ct}. Finally, at the lowest frequencies between 1 Hz and 25 mHz, the diffusional mass transport resistance R_{diff} appears.[34] Therefore, in the context of this research, we determined R_Ω, $R_{ct,}$ and R_{diff} by linearly extrapolating the semi-circles to the real-part impedance axis. Indeed, the measured resistance data included additional factors. For instance, the inductance of the circuit influenced the resistance at high frequencies $>$ 10 kHz. Moreover, the electronic and ionic conductance contributed to the resistance at medium frequencies $20\,\text{kHz} > f > 1\,\text{Hz}$, according to the transmission line model.[35] However, since these factors were invariant over time, we consider them not to interfere with the present research results.

Scanning electron microscopy (SEM) and krypton adsorption analysis.—We investigated the electrode surface for its microscopic appearance using a Zeiss Ultra 55 plus instrument. We analyzed the samples (without special preparation) using the Inlens-detector at an acceleration voltage of 10 to 12 keV.

Additionally, we examined the specific surface area with krypton adsorption at 77.4 K performed with an Autosorb iQ2 (Quantachrome Instruments, USA). The area was calculated using the Brunauer–Emmett–Teller (*BET*) method. Before analysis, we degassed the samples at 300 °C for at least 24 h. Due to the relatively small surface area, in order to obtained reliable results, about 1 g of sample was used for each analysis.

X-ray photoelectron spectroscopy.—X-ray photoelectron spectroscopy (*XPS*) was employed to monitor the changes in the oxygen groups present at the surface of the evaluated GF electrodes, focusing on the C 1 s and O 1 s regions. The GF electrodes were cut into 25 mm^2 samples and mounted conducting on a stainless steel sample holder. All *XPS* spectra were recorded at 40 eV pass energy, a 0.1 eV step size, and a 1000 ms dwell time with an Axis Supra system (Kratos, UK) using a monochromatic Al Kα source (1486.6 eV). For each sample, an initial survey scan was recorded, followed by a high-resolution spectrum of the elements of interest. Each spectra's binding energies were corrected based on the adventitious carbon signal from the C 1 s spectrum at 284.4 eV. The O/C ratio was calculated from the relevant peak areas, integrated using a Shirley background for the O 1 s region and a 2 U Tougard background for the C 1 s region using the CasaXPS software (Version 2.3.22PR1.0). All areas were normalized by the corresponding atomic subshell photoionization cross-section[36] and the escape depth, predicted using the NIST Electron Effective-Attenuation-Length Database.[37]

Results and Discussion

Nyquist plots and voltage efficiencies throughout the first 20 h of idle operation.—Figure 3a shows the Nyquist plots of the repetitive *PEIS* of a VRF single-cell with the differently modified GF electrodes (see Fig. 1b for the electrode modification). From top to bottom, the duration of thermal treatment in air at 400 °C is increasing. The bottom plot represents the commercial reference electrode GF-HT thermally treated by the supplier. Each graph represents one electrode modification monitored over their first 20 h after initial contact with the 50%-charged vanadium electrolyte. All Nyquist plots comprise two characteristic semi-circles, the first pronounced ones representing R_{ct} and the second smaller ones R_{diff}. With all GF electrodes, we observed that the first R_{ct} semi-circle increased with the idle operation time. We plotted the R_{ct} values for each GF electrode as a function of the idle operation time in Fig. 3b. R_{ct} increased continuously, regardless of the electrode modification applied previously. However, in absolute terms, both the initial R_{ct} and the rate of increase $\Delta R_{ct}/\Delta t$ became smaller for longer thermal treatment times.

The GF-0h serves here as a control sample since it has only been treated with plasma to increase the electrode wettability, as seen in Fig. 1b. In Fig. 3c, we normalized each R_{ct} to the respective R_{ct} of sample GF-0h to disregard any contribution from the plasma treatment. The resulting ratios indicate that thermal treatment further enhanced the absolute electrode activity distinctly. After just three hours of heat treatment, R_{ct} decreased by 50% (green in Fig. 3c) and by 78% after 24 h of heat treatment. GF-HT as a commercially available GF variant showed the lowest R_{ct} of the evaluated samples being only 15% of the value of GF-0h.

Additionally, we normalized each series of R_{ct} to its respective first measured value at the beginning of each repetitive *PEIS* sequence in Fig. 3d. Indeed, the tested samples differed significantly by their absolute R_{ct}. However, in relative measures, their R_{ct} increased similarly, by a factor of 1.5 ± 0.2 over the first 20 h of operation. Moreover, GF-HT showed a similar degradation with a 1.5-time increase, as did the in-house plasma- and thermally treated samples. Thus, the similar degradation of GF-HT lacking the plasma treatment indicates no correlation between performance degradation and plasma treatment. Instead, it suggests that degradation as a general phenomenon is independent of electrode modification.

Using the *short-GCP* technique complementary to *PEIS*, we analyzed the voltage efficiency η_V. In Fig. 4a, we show the η_V for GF-0h, GF-3h, and GF-24h at current densities ranging from 0–80 mA cm^{-2}. Additionally, in Fig. 4b, we plotted them over the elapsed time of idle operation from 0–20 h. The trends observed in Fig. 4 reflect the features already noticed in the *PEIS* measurements. As these features became most evident for high current densities, we will focus on the analysis of the η_V at 80 mA cm^{-2}. As expected from the R_{ct} trends, the η_V of GF-0h started at a lower value of 85.3%, whereas GF-24h began at 91.0%, which accounts for a 5.7% higher efficiency. Regarding the idle operation time, agreeing with the R_{ct} trends, we observed that the η_V decreased with time on the three electrodes evaluated. However, between the electrodes with different treatment times, the extent of η_V decrease varied, being less pronounced on the electrodes subject to longer treatments. Accordingly, η_V of GF-0h shows a marked drop of 2.1% (i.e., from initially 85.3% at 0 h to 83.2% at 20 h). In contrast, the η_V of GF-24h decreased by only 0.3% (i.e., from initially 91.0% at 0 h to 90.7% at 20 h). The η_V of the GF-3h electrode estimated at 80 mA cm^{-2} falls between the η_V of GF-0h and GF-24h, reflecting the trends in R_{ct}. In general terms, the longer the thermal oxidation lasted, the smaller the decrease in η_V was over idle operation time.

Given all of the analogies between *PEIS* and *short-GCP* identified, one might conclude that both techniques assess the cell performance and reveal quantitative data likewise. However, the perspective of these two sets of performance data is different. On the one hand, *short-GCP* showed how internal processes in the cell intervene in the performance overall and translate into a practical

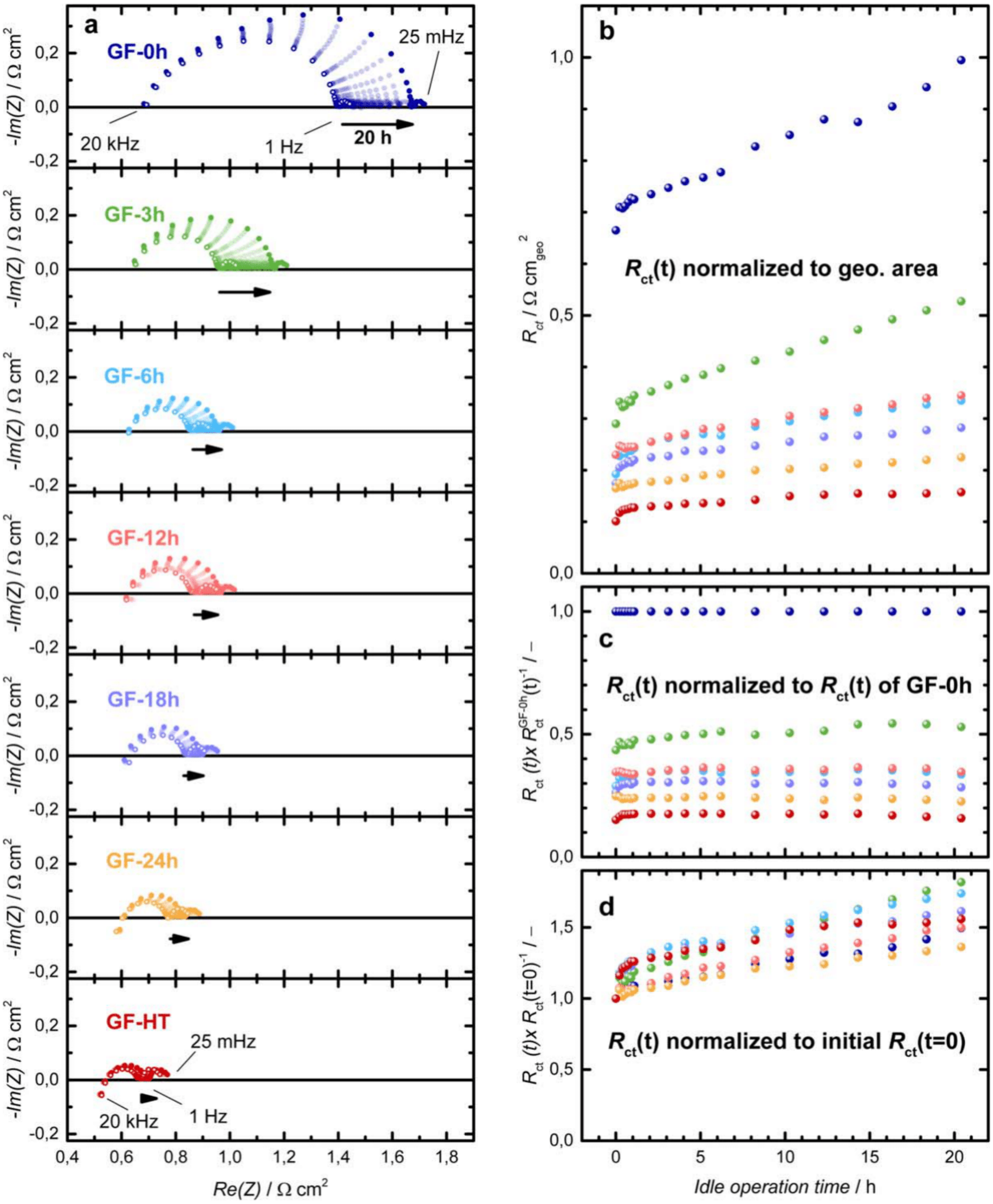

Figure 3. (a) Nyquist plots of repetitive *PEIS* over 20 h of initial idle operation for all modifications of the graphite felt electrodes investigated. From top to bottom: Electrodes were thermally treated in-house for increasing durations at 400 °C (GF-0h - GF-24h) and thermally treated by the supplier (GF-HT). (b) charge-transfer resistances R_{ct} over 20 h of idle cell operation, normalized to the geometric electrode area of 25 cm^2. (c) R_{ct} over idle operation time, each point in time normalized to the respective value for the GF-0h sample, relating the different electrodes to each other. (d) R_{ct} over idle operation time, normalized to its initial value at t = 0, showing each relative R_{ct} increase ratio.

meaning for technical applications. For instance, the only plasma-treated electrodes showed low efficiency from the beginning, which continued to degrade fast. Thus, particularly when considering a long-term operation, we conclude that their economic viability for technical purposes is questionable. On the other hand, *PEIS* provided a greater depth of information when distinguishing between partial resistances. In the present study, this distinction revealed that the change in performance was due to a changing R_{ct}, which, in turn, implies changes on the electrode surface.

We learned that the electrode performance improved dramatically upon thermal treatment. *However, since the plasma pretreatment resolved the wettability problem, why did the thermal treatment enhance the performance, corresponding so strictly with the treatment duration? Is the performance improvement dominated by a change in surface structure or an increase in surface oxide groups?* Addressing these questions, in the next section, we will investigate how the surface structure and its TSA changed as a result of thermal treatment for different treatment times.

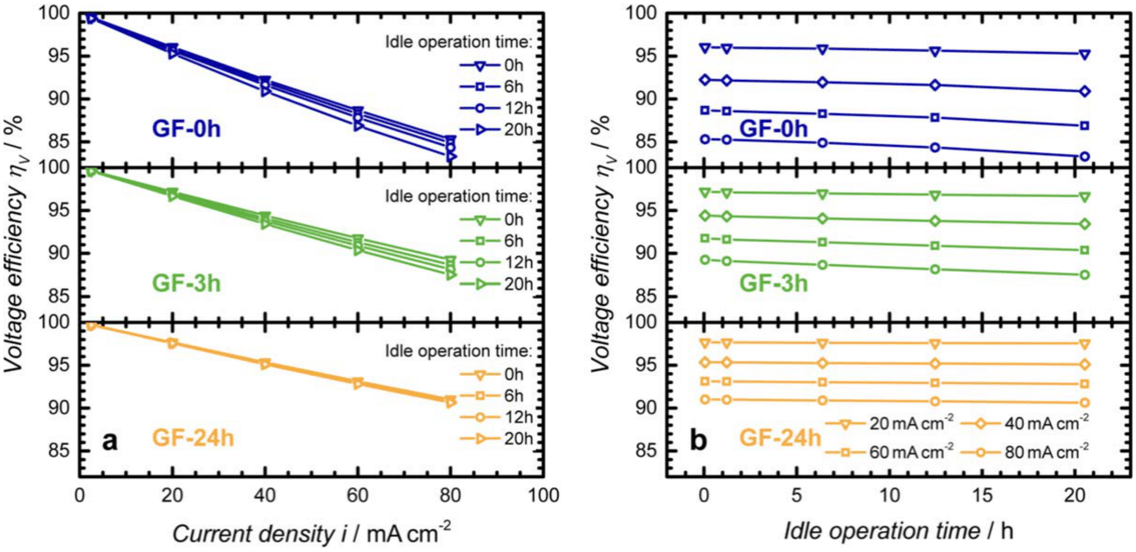

Figure 4. Voltage efficiencies from repetitive *short-GCP* single-cell measurements of GFD4.6 graphite felt electrodes after plasma and subsequent heat treatment at 400 °C for the duration of 0 h (blue), 3 h (yellow), and 24 h (green) in idle cell operation at an SoC of 50%. (a) Voltage efficiency vs current density at different points in time (after 0, 6, 12, and 20 h of idle operation). (b) Voltage efficiencies vs idle operation time over 20 h.

Scanning electron microscopy (SEM).—We examined the surface structure of single fibers of the different electrode modifications using SEM micrographs. Figure 5 compares the images of four treated electrodes. The three upper rows show GF-0h, GF-12h, and GF-24h, which we modified in-house; the lower row depicts GF-HT modified commercially. The left images represent a 4.000-fold magnification (Figs. 5a, 5c, 5e, and 5g). For better inspection, the images on the right zoom with 40.000-fold magnification (Figs. 5b, 5d, 5f, and 5h).

In this context, GF-0h served as a reference material that was only plasma-treated but did not experience any corrosive thermal treatment (Figs. 5a and 5b). Consequently, disregarding the native rills and grooves with smooth edges, no defects can be found on its surface. Surprisingly, GF-12h thermally treated in air at 400 °C for 12 h showed no visible change (Figs. 5c and 5d). Eventually, the situation appeared different for GF-24h (Figs. 5e and 5f). The previously smooth edges seem nibbled, thus receiving a fringed structure visible with the 40.000-fold magnification. Finally, the trend culminates for GF-HT. While already recognizable in Fig. 5g on the left, it is eye-catching at 40.000-fold magnification in Fig. 5h. The surface resembled a cratered landscape, and the former grooves were only vaguely retraceable. Instead, an array of adjacent surface pores appeared, with pore sizes in the order of 50 nm. Given this evident increase in surface roughness, we also expected the specific surface area to increase.

Krypton adsorption and BET analysis assessing the total surface area (TSA).—To quantify these *SEM* observations, we assessed the electrode surface areas by krypton adsorption and calculated the corresponding *BET* surface area (S_{BET}), interpreted as the *TSA* and summarized in Fig. 6a. The thermal treatment increased the *TSA* with time. While the *TSA* of the as-received felts (GF-ar) increased only marginally by 4% from 0.49 to 0.51 m^2 g^{-1} (± 0.03 m^2 g^{-1}) after the plasma pre-treatment, the subsequent thermal treatment had a more substantial effect on the *TSA*. After the first three hours of thermal treatment (GF-3h), the surface area increased by 8% to 0.55 ± 0.03 m^2 g^{-1}. A longer treatment duration caused a continuous increase in *TSA* by 0.02 (m^2 g^{-1}) h^{-1} until, after 24 h, the *TSA* had doubled. The increased *TSA* of the GF-24h sample agreed with the *SEM* images showing a higher surface roughness due to the apparent fringed structure. While the *SEM* images for the GF-12h sample failed to visualize any structural changes, krypton adsorption resolved a significant surface area increase for treatment durations shorter than 24 h. For the GF-HT sample, the situation is even more distinct. According to the *SEM* images, this sample displayed the roughest surface (cf, Figs. 5g and 5h). In agreement with this observation, the S_{BET} of the GF-HT sample was 6.11 ± 0.03 m^2 g

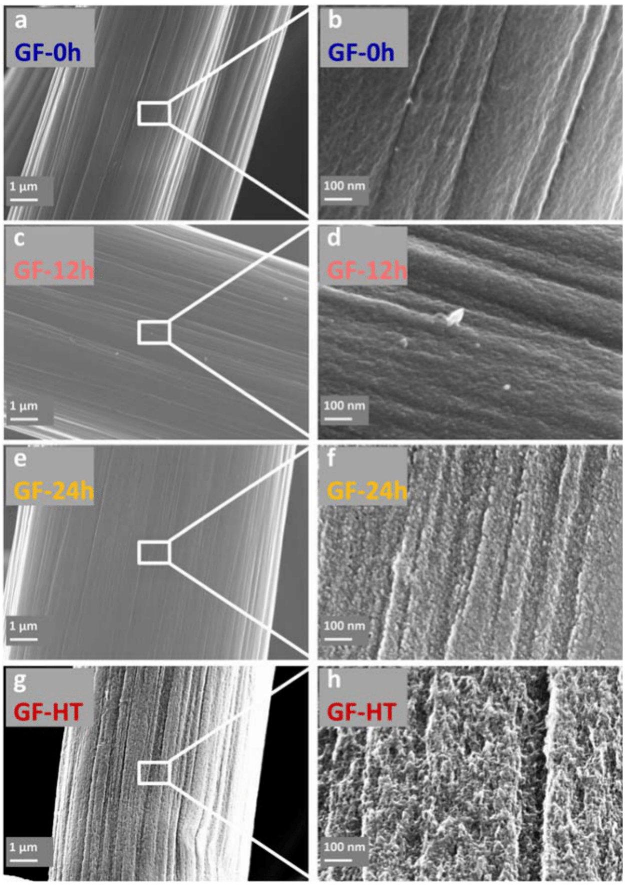

Figure 5. *SEM* micrographs of GF-0h (a), (b), GF-12h (c), (d), GF-24h (e), (f), and GF-HT electrodes (g), (h), with 4.000-fold magnification shown on the left, and 40.000-fold magnification on the right, respectively.

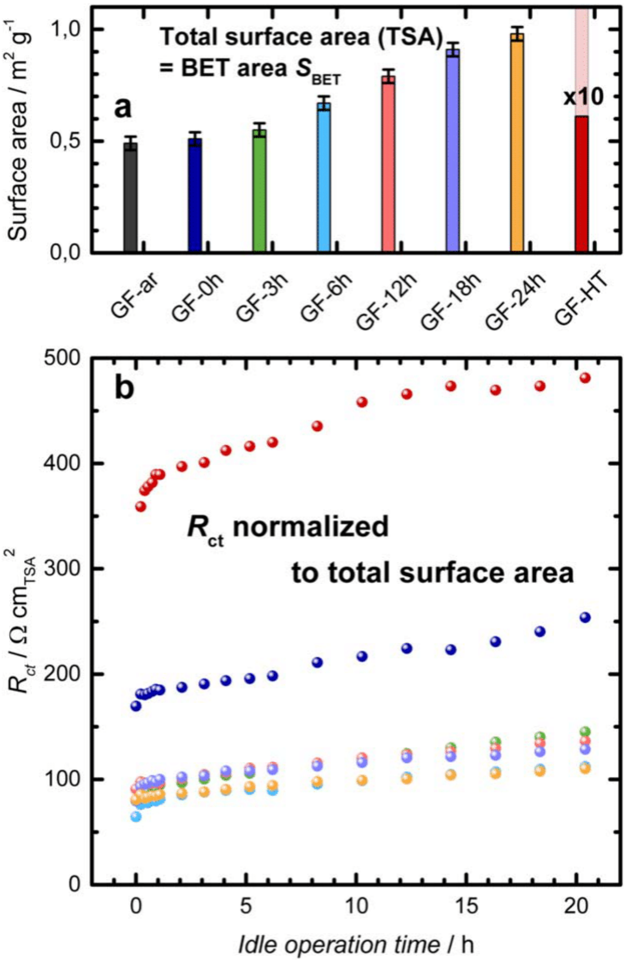

Figure 6. (a) Surface areas calculated from the *BET* analysis of krypton adsorption, interpreted as total surface areas (*TSA*). (b) R_{ct} normalized to the *TSA* derived from krypton-*BET* analysis.

$^{-1}$. This value corresponds to an increase in *TSA* of 520% compared to the sample GF-24h.

To test how the electrode kinetics relates to the actual carbon surface area, we normalized the R_{ct} from Fig. 3 to the *TSA* (see Fig. 6b). Interestingly, the GF-0h and GF-HT electrodes presented higher R_{ct} normalized to the carbon area than the other electrodes. GF-0h comprised twice the R_{ct} of GF-3h to −24h, whereas GF-HT showed even four times higher values, which will be discussed in the next section. All the other electrodes (GF-3h to −24h) showed comparably equal R_{ct} being around 100 Ω cm^2 during the first 20 h of operation, confirming the EC performance to correlate with surface structure.

Other than structure, the surface composition remained to be examined. Not least accounting for the deviating GF-0h and GF-HT, the observed kinetics may have resulted from the accumulation of surface functionalities. The most prominent are surface oxides commonly attributed to a high catalytic activity, which we will examine below.

X-ray photoelectron spectroscopy (XPS) assessing the oxygen surface content.—We used XPS to examine how the carbon surface's atomic composition changed following the electrode modifications. Figures 7a–7c present exemplary spectra taken from the C 1 s and O 1 s regions. Figure 7a shows the O 1 s region normalized by the maximum intensity of the respective C 1 s peak (284.4 eV) for each sample. This comparison is done only for a selected set of treated GFs, to illustrate the differences in oxygen content on each of the GF samples. Figures 7b and 6c show another type of normalization for both the C 1 s and O 1 s regions. The C 1 s and O1s peak intensities were normalized by the C 1 s and O 1s regions' maximum intensity. The aim was to get a qualitative comparison of the overall peak shape and evaluate the possibility of different oxygen species present on each modified electrode. In Fig. 7a–7c, we selected the GF-ar, GF-0h, and GF-HT as reference electrodes to be compared with GF-24h, the electrode with the most prolonged thermal treatment done for 24 h. At first glance, the spectra suggested evident differences in the oxygen content between reference and thermally treated electrodes. We quantified this difference by the ratio of the individual C 1 s and O 1 s peak areas, known as the O/C-ratio, measuring the electrode surface's oxygen content (Fig. 7d). A comparison of GF-0h with GF-ar in Fig. 7a clearly shows that the sole plasma treatment extensively enriched the surface with oxygen. This enrichment is also evident in Fig. 7d in the O/C ratio, which increased from 2.4% (GF-ar) to 16.0% (GF-0h). This increase confirmed that the electrodes became more wettable after the plasma treatment because the number of oxygen surface groups increased.

The O/C-ratios for the electrodes thermally treated in air at 400 °C were different than expected. Reports in the literature suggest that a more aggressive (500 °C)[17] or prolonged (30 h)[20,29] thermal treatment increases the surface oxides. However, Eifert et al. reported that this was not the case for the evaluated treatment (in air at 400 °C for 25 h).[38] Our data also showed that further thermal treatment combined with preceding plasma treatment did not increase the oxide concentration but had the opposite effect. After only three hours (GF-3h), the surface oxide groups decreased to less than half of the value for GF-0h, from 16% down to 7%. No clear trend emerged for the electrodes with more prolonged treatment time, and their O/C ratio remained at 8 ± 2%, at about half the level than GF-0h.

The O 1 s peaks represent many different surface oxide groups, including hydroxyl, carbonyl, or carboxyl functionalities.[39] Thereby, each species may catalyze the presumably inner-sphere V2+/V3+-reaction to different extents characterized by its site-specific rate constant. Consequently, some distinct oxides may be responsible for the gross activity. There are many opinions in the literature on how the XPS technique can identify specific surface species catalyzing the vanadium reactions. This variety resulted in many different interpretations of the XPS spectra, attributing the increased electrode performance to different species such as C–OH[4,10,20,40,41] C=O,[7,40,42] and COOH groups.[7,11,41] However, this interpretation is susceptible to the type of line shape and background used to fit the XPS spectra. Thus, we opted for just a qualitative comparison of the spectra focussing on the integral O/C ratios rather than on individual oxygen species potentially influencing the electrode performance. Thereby, the O 1 s peak shape in Fig. 7b did not qualitatively vary among the presented samples, suggesting that the composition of oxygen surface groups remained the same. Similarly, the C 1 s peak comparison between the GF-24h and GF-HT electrode in Fig. 7c showed almost identical peak shapes, a trend persisting for all the thermally treated electrodes GF-3h—GF-24h. As a result, the identical peak shapes did not identify specific surface groups responsible for the performance improvement.

When accounting for the *BET* results, the GF-24h electrode surface comprised two times the *TSA* but only half the O/C ratio, compared to GF-ar, suggesting that its total oxide amount remained constant. Hence, for the evaluated thermally treated GF electrodes, a surface oxide increase cannot explain the simultaneous fivefold increase in EC activity (cf, Fig. 3c). Instead, some other surface property must be associated with the reduced R_{ct}. Judging from the observed R_{ct} correlation with *TSA*, this property is most likely related to the surface structure.

Resolving changes in surface structure with *SEM* was difficult for GF-3h - GF-12h. However, GF-24h eventually revealed a change in surface appearance. Its fringy form proved that the mild treatment at 400 °C corroded the topmost carbon layers. In an idealized picture,

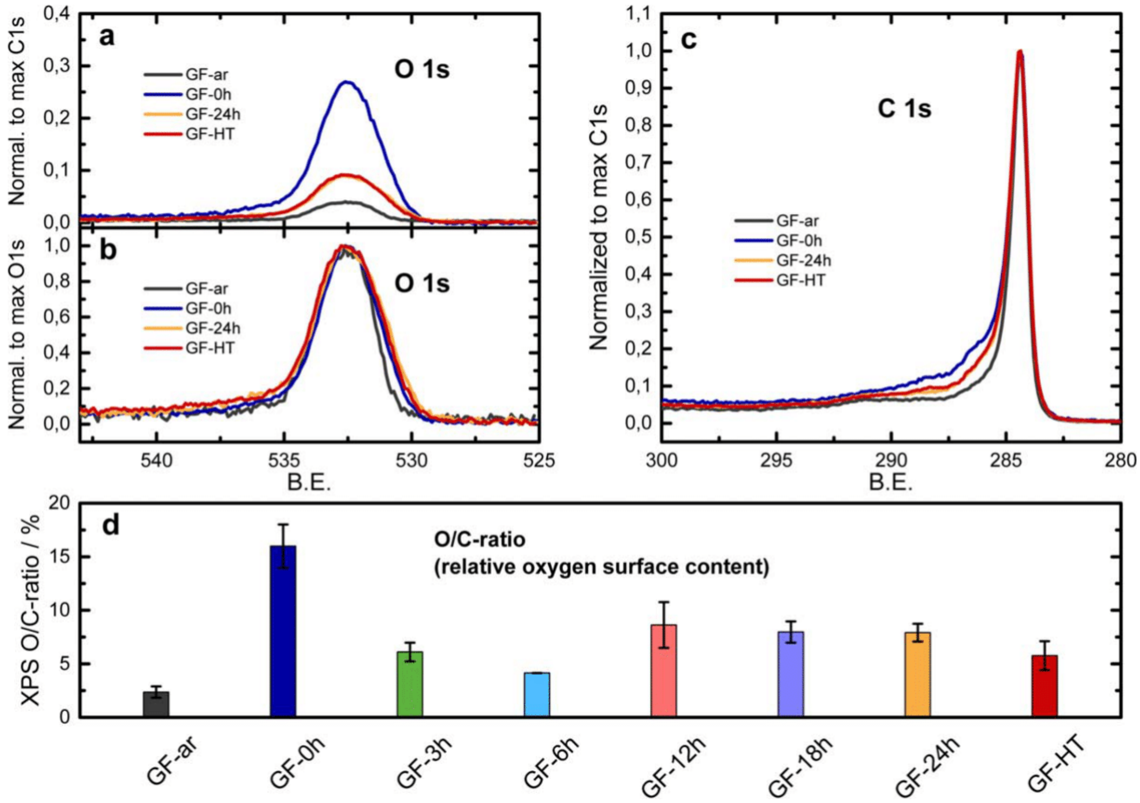

Figure 7. (a) O 1 s *XPS* spectrum normalized by the maximum intensity of the respective C 1 s peak (284.4 eV) of the reference samples GF-ar, GF-0h, and GF-HT, and the thermally treated electrode GF-24h. (b) O 1 s and (c) C 1 s *XPS* spectra normalized by the maximum intensity of the individual O 1 s (532.5 eV) and C 1 s (284.4 eV) regions presented for the reference electrode GF-ar, GF-0h, and GF-HT and the thermally treated electrode GF-24h. (d) O/C ratio obtained from peak areas of the individual C 1 s and O 1 s regions for the reference and thermally treated GF electrodes.

the top layers constitute ordered and electrochemically inactive basal planes.[43] When thermal treatment sets in, these basal planes start to corrode. Over time, at defects, edges, and corners, corrosion proceeds to "eat away" carbon after carbon along the basal plane, leaving behind more and more edge sites instead.[24,44,45] Compared to basal sites, edge sites comprise much higher catalytic activity for inner-sphere reactions,[46,47] including the V^{2+}/V^{3+}-reaction.[48,49] This higher activity may explain the disproportionate performance improvement observed with *TSA*.

However, krypton adsorption does not differentiate between basal and edge sites. Consequently, considering the sites' diverging specific activity, we cannot expect a linear correlation between R_{ct} and *TSA*. Instead, R_{ct} may be linearly proportional to the surface area constituting only graphitic edge sites. As proposed by Rabbow and Whitehead, this edge site area is accessible by deconvoluting the electrochemical double-layer capacitance (*EDLC*).[50] The *EDLC* consists of contributions from relatively inactive basal carbon planes and edge planes accounting for the active surface area (*ASA*). Thereby, the edge planes contribute much more to the *EDLC* than basal planes (cf, 1–3 μF cm^{-2} from basal planes vs 50–100 μF cm^{-2} from edge planes).[51–53] Rabbow et al. have demonstrated that the knowledge of the *TSA* and the *EDLC* generally suffices to determine the size of the *ASA*. By describing the basal plane surface as the difference *TSA-ASA*, the *EDLC* is an expression of the edge and basal plane contributions corresponding to

$$EDLC = (TSA - ASA)\cdot c_{basal} + ASA\cdot c_{edge} \tag{3}$$

The carbon surface-specific capacitances were determined to $c_{basal} = 3.2\,\mu F\ cm_{carbon}^{-2}$ and $c_{edge} = 47.8\,\mu F\ cm_{carbon}^{-2}$. Solving Eq. 3 yields the ASA as

$$ASA = \frac{EDLC - TSA\cdot c_{basal}}{c_{edge} - c_{basal}}. \tag{4}$$

Consequently, we sought to assay the electrodes' *EDLC* by cyclic voltammetry (*CV*) and *PEIS* (cf, Fig. SI 10). For doing so, we vacuum-infiltrated the electrodes at low pressure < 3 mbar for 3 min each. The gravimetric capacitance values derived by *PEIS* at 0.15 V vs Hg/Hg_2SO_4 match the range of the ones measured by Rabbow et al., with GF-0h and GF-HT presenting 33 mF g^{-1} and 298 mF g^{-1}, respectively. Unfortunately, the plasma and thermally treated electrodes showed no unambiguous trend with thermal treatment time, so we assessed the results as not reliable enough for further conclusions. Presumably, the different amounts of surface oxides concentrations causing pseudo-capacitance by faradaic reactions superimposed the double-layer capacitance. This assumption derives from the following observation. When exposed to a second plasma treatment, the thermally treated electrodes exhibited an up to 60% increase in capacitance, illustrating the significant capacitance variation due to additional surface oxides. Accordingly, it deemed not reasonable to derive any robust conclusions from the capacitance data, e.g., to derive the *ASA* and correlate it with performance.

The relative effect from pseudo-capacitance is presumably low for the two samples GF-0h and GF-HT, differing substantially in *TSA*. For those electrodes, the *ASA,* according to Eq. 4, was at 380 $cm_{edge}^{-2}\,g^{-1}$ and 2300 $cm_{edge}^{-2}\,g^{-1}$, respectively, being again in good agreement with the data of Rabbow et al. These values of *ASA* correlate much closer with the R_{ct} than the ones for the *TSA*. This relation explains why the *TSA*-specific R_{ct} in Fig. 6b showed much higher values than those of the other modifications. The increased *TSA* may predominantly comprise basal carbon planes contributing

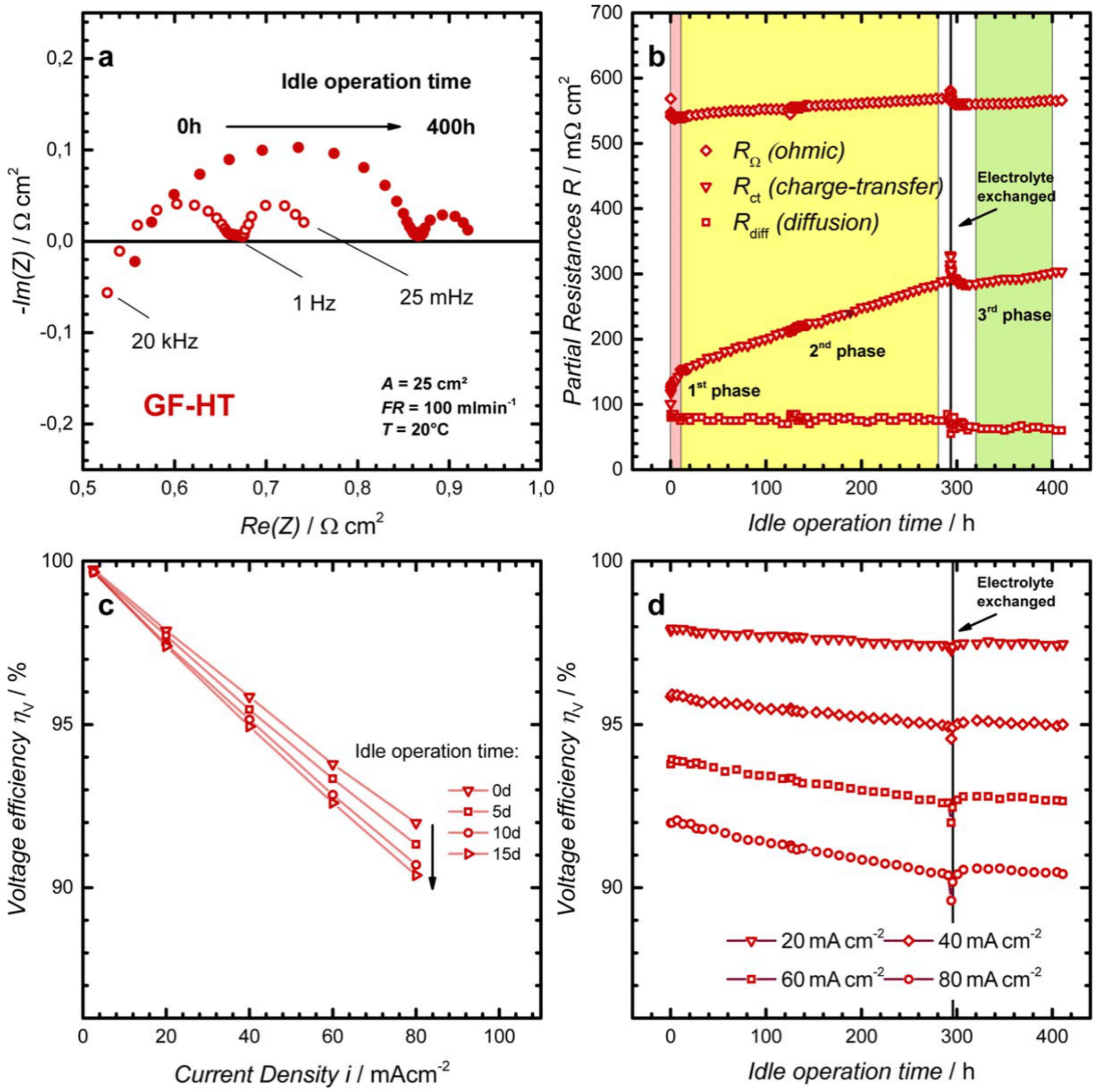

Figure 8. (a) Nyquist plots of repetitive *PEIS* single-cell measurements for commercially available GF-HT electrodes (SGL Carbon) for a duration of 400 h (16.7 d) in idle cell operation at an *SoC* of 50%. The open circles represent the first *PEIS* recorded right after initial electrolyte contact (0 h). In contrast, the filled circles are the *PEIS* recorded after 400 h of idle operation. (b) Respective separated partial resistances vs idle operation time over 400 h. (c) Voltage efficiency vs. current density at different points in time (after 0, 5, 10, and 15 d of idle operation). (d) Voltage efficiencies vs idle operation time over 400 h.

to the kinetics enhancement less than the edge planes do. This situation demonstrates that the performance differences might be solely explainable by differences in carbon edge planes.

Although the *ASA* is hard to estimate, the proposed surface transition can explain why the R_{ct} halved after only 3 h of thermal treatment compared to sample GF-0h. The basal plane corrosion may have led to a substantial edge site formation.[23,24,45] On the atomic scale < 1 nm, corrosion would have continuously accumulated more and more edge sites, contributing a disproportionally large share to the surface-specific catalytic activity. Therefore, thermal treatment is effectively altering the surface structure, long before becoming visible by *SEM* and only implicated by krypton adsorption analysis. The resulting increase in edge sites could be responsible for the observed pronounced enhancement in EC surface activity.

Due to the small absolute R_{ct} of sample GF-HT, its performance appeared almost stable throughout the short-term operation of 20 h. Therefore, the GF-HT was selected to evaluate the performance trends for long-term operation. To do so, we measured the GF-HT performance for a more extended operation period of 400 h. Again, all system settings such as temperature, flow rate, and SoC were constant throughout this period.

Monitoring commercial GF-HT electrodes over 400 h of idle operation.—We investigated the graphite felt GF-HT for its long-term electrode performance. GF-HT is another modification variant of GFD4.6, thermally treated by its supplier SGL Carbon. Possibly adjusted treatment parameters were the temperature and duration.[13] Also, the treatment atmosphere can have a significant impact, more specifically, the atmosphere's content of water[54] and oxygen.[14] Although the modification procedure was not specified, the electrode presented a specific *TSA* of 6 $m^2\ g^{-1}$, the highest *TSA* evaluated. Consequently, as a commercially available material with an optimized surface area and a superior 20 h performance, GF-HT attracted interest to be studied for a more extended period of 400 h.

Throughout 400 h, we continuously pumped the electrolytes at 100 ml min^{-1} flow rate, 50% *SoC,* and 20 °C temperature through the 25 cm^2 GF-HT electrodes mounted in the single-cell. During this time, we intermittently probed the cell with repetitive *PEIS* and *short-GCP*. Figure 8a represents Nyquist plots of the first and the last *PEIS*, while Fig. 8b illustrates the three partial resistances R_Ω, $R_{ct,}$ and R_{diff} separately over the idle operation time. Overall, the familiar trend of increasing R_{ct} appears. By comparison, R_Ω and R_{diff} remained constant, but R_{ct} increased steadily, from 120 mΩ cm^2 to 300 mΩ cm^2.

Interestingly, the rate of increase $\Delta R_{ct}/\Delta t$ took on distinctly different values associated with three phases. The first phase emerged during hours 0–10 (light red area in Fig. 8b), where R_{ct} rose with a steep slope from 120 mΩ cm^2 to 150 mΩ cm^2, and the increase rate amounted to 3.0 mΩ cm^2 h^{-1}. The second phase followed between hours 10–290 (yellow area in Fig. 8b); R_{ct} grew linearly from 150 mΩ cm^2 to 290 mΩ cm^2 but at a much slower rate of 0.5 mΩ cm^2 h^{-1} being a sixth of that during the first phase. Finally, in a third phase (green area in Fig. 8b), the inclination became low between hours 320–400, elevating from 285 mΩ cm^2 to 300 mΩ cm^2. The rate of increase in this last phase was 0.2 mΩ cm^2 h^{-1}, which was only a fifteenth of the pace during the first 10 h.

During the first and second phases up to hour 290, the cell operated on the same original electrolyte. Eventually, the tank filling levels differed by 20%, pointing at a directed electrolyte transport. Pezeshki et al. found that the accompanying vanadium crossover leads to a shift in reactant concentrations, causing the electrolyte to be increasingly imbalanced.[28] Moreover, oxygen diffusion via the tubing adds to this effect.[55] This electrolyte imbalance may have contributed to the linear R_{ct} increase in the second phase. Therefore, after 290 h, we exchanged the potentially imbalanced electrolyte. With N_2 overpressure, we flushed the electrolyte out of the tanks, the tubing, and the measuring cell. We then replaced the measuring cell with the conditioning cell, refilled the system with fresh V^{+III}/V^{+IV}, and pre-charged the new electrolyte to 50% *SoC*. Finally, we returned the measuring cell, re-flooded the electrodes, and continued the performance test. From hour 320 on, the trajectory of R_{ct} followed a flatter course, reflecting the fresh, balanced electrolyte.

However, before, between hours 290–320, a pronounced peak in R_{ct} appeared, with R_{ct} jumping from 290 to 330 mΩ cm^2 and dropping back to about 285 mΩ cm^2 during the next 30 h. We attribute the feature to entrapped gas remaining in the electrodes after the electrolyte exchange, temporarily compromising the ECSA. Presumably, during hours 290–320, the continuous electrolyte flow dragged out the gas inclusions, explaining that R_{ct} resumed its previous course of a slow increase. Accordingly, the R_{ct} drops from 330 mΩ cm^2 to 285 mΩ cm^2 due to improving electrode saturation accounting for 45 mΩ cm^2 of additional R_{ct}. In relative measures, this corresponds to **45/285 = 16**% of electrode volume that was not contacting the electrolyte after the system refill. This figure is consistent with the observations of Bevilacqua et al., where the electrolyte saturation of graphite felt electrodes showed to increase from 73% to 78% after the first few minutes of electrolyte flow-through.[21] As a remark, the heat-treated electrodes from the previous section might have faced a similar, slight constriction in *ECSA* upon initial electrolyte saturation. Indeed, the *ECSA* and, in specific, the *ASA* proved hard to estimate. However, the strong correlation of the electrodes' respective R_{ct} with treatment time and *TSA* suggests that the deviations in electrolyte saturation were very comparable to each other. Interestingly, this effect of progressive *ECSA* increase with electrolyte saturation counteracts the observed initial R_{ct} increase due to kinetic degradation. The situation where both effects balance each other explains why the initial kinetic degradation may be unnoticeable in some studies found in the literature.

In the third phase, between hours 320 and 400, notably, R_{ct} was now at slightly smaller values, 10 mΩ cm^2 less, reflecting the new, balanced electrolyte. Moreover, R_{ct} rose distinctly slower than in the first 10 h, at a fifteenth growth rate. The decelerating rate agrees with studies observing the degradation to slow down over eight days of operation (168 h).[27] If continuing, this trend may predict that the R_{ct} increase will become insignificant at some point, or R_{ct} even converges to a constant value.

The observed trend of decelerating degradation agrees well with the concept of an adsorbant leading to the degradation, as we proposed in a previous study.[30] Accordingly, V^{2+} adsorbs to the reaction surface, covering it and, thus, inhibiting the further V^{2+}/V^{3+}-reaction. Over time of operation and contact to V^{2+}, an equilibrium coverage will form, leaving behind an uncovered ECSA (A_{ECSA}). Then, the temporal evolution of the A_{ECSA} being not yet covered and deactivated by an adsorbent can be expressed as

$$A_{ECSA} = A_{ECSA,0}\left((1-\theta) + \sum_i \theta\cdot e^{-k_i\cdot t}\right) \qquad [5]$$

Here, $A_{ECSA,0}$ stands for the initial fully uncovered ECSA before in contact with V^{2+}/V^{3+}-electrolyte. Moreover, θ is the relative equilibrium coverage, k_i the decay constants, and t the idle operation time. With R_{ct} being inversely proportional to A_{ECSA}

$$R_{ct} \propto (A_{ECSA})^{-1}, \qquad [6]$$

the trajectory of R_{ct} can be fitted by Eq. 5 with two decay constants (i = 2). This perception of an equilibrium coverage explains why the observed degradation process decelerates and provides another strong argument for a converging R_{ct}.

For practical purposes, *short-GCP* (Fig. 2) allowed translating the corresponding performance into voltage efficiencies (η_V) according to Eq. 2. In Fig. 8c, we plotted η_V vs the current density measured after selected idle operation times. Figure 8d shows η_V over the idle operation time measured at 20, 40, 60, and 80 mA cm^{-2}. As expected, η_V revealed very slight degradation. Only evident throughout the prolonged 400 h operation time, the efficiency at 80 mA cm^{-2} decreased by 1.5%. Moreover, the deceleration from above implies that the degradation only shows in the first days and weeks of operation, suggesting that the battery will ultimately run at nearly constant performance in the long term.

In Fig. 8, the efficiency degradation was only resolvable under highly constant electrolyte conditions since R_{ct} was highly sensitive to temperature changes, as demonstrated in Figs. SI 6 and SI 7. Another supporting factor was the moderate electrolyte temperature of 20 °C. If measured at 30 °C instead of 20 °C, R_{ct} would have contributed 27% less to the overall cell resistance. Consequently, changes of R_{ct} would have been less evident, and the overall efficiency would have appeared even more stable over time. These observations may explain findings in the literature, reporting stable performance for activated GFD electrodes.[29] Conclusively, when assessing electrodes with sufficient *TSA*, the efficiency may indeed appear stable within given cell operation times.

In summary, although we were able to resolve the degradation of GF-HT, the drop in efficiency throughout 400 h was minor, being likely a result of the large *TSA*. Moreover, as the already low degradation decelerated, high and stable cell performance is in prospect for long-term operation.

Conclusions

We studied the effects of thermal treatment on VRF graphite felt electrodes after they were plasma-treated to ensure complete wettability. Compared to the sole plasma treatment, additional thermal treatment enhanced the electrode performance progressively, primarily due to surface corrosion increasing its roughness and total surface area (*TSA*). The corrosion presumably increased the number of carbon edge-plane surface sites catalyzing the V^{2+}/V^{3+}-reaction. The content of surface oxygen functionalities played no significant role.

Sole plasma treatment equipped the surface with the most oxygen functionalities. However, these electrodes showed the highest initial R_{ct} of 0.7 Ω cm^2, further suffering degradation by a 50% R_{ct} increase over 20 h idle cell operation. Additional to plasma, thermal treatment enhanced the performance significantly, evident in an R_{ct} eventually decreased by 78% after 24 h treatment. Simultaneously, the thermal treatment decreased the surface content of oxygen functionalities from 16% to 8%, opposed to findings in the literature reporting the electrode performance to correlate with oxygen functionalities.

Instead, *SEM* imaging of the GF electrode surface indicated a roughening of the fiber surface. Krypton *BET* analysis revealed the *TSA* incrementally increased from 0.5 m^2 g^{-1} to 1.0 m^2 g^{-1}. However, the *TSA* increase could still not explain the R_{ct} decrease in absolute measures. Therefore, we presume that the carbon surface corrosion causing the increased *TSA* and roughness had created carbon edge sites increasing the catalytic surface activity.

Addressing the performance degradation, we found that electrodes with a higher *TSA* showed a minor R_{ct} increase in absolute measures. However, in relative measures, the R_{ct} of each examined electrode increased similarly by 50% over the initial 20 h of operation, disregarding the *TSA*. Consequently, we examined the GF variant with the highest *TSA* of 6 m^2 g^{-1} for its long-term cell operation. Over 400 h, the R_{ct} increased by 300% from 0.1 to 0.3 Ω cm^2, resulting in a cell voltage efficiency decrease from 92% to 90% at 80 mA cm^{-2}. The degradation rate decelerated significantly, indicating that the decreasing efficiency aims for eventually stable values. A recently proposed mechanism explaining the observed degradation due to V^{2+} surface adsorption supports this observation. Thereby, the formation of an equilibrium surface coverage by adsorbent suggests stable kinetics and constant long-term performance. Consequently, enlarging the *TSA* enhances the electrode performance at any time of cell operation.

In general, future studies on modifying electrode material should thoroughly investigate the changed surface properties. In particular, critical assessment should focus on whether the main improvement results from accumulated surface oxygen functionalities, improved wettability, increased *TSA*, or altered surface structure. Instead of surface oxygen enrichment, in our case, surface corrosion and concomitant *TSA* enlargement proved as the more effective strategy to exploit the full electrode performance potential. This strategy may lead the way to bring VRF batteries closer to their ultimate goal of finding their widespread use, contributing to an energy-rich but sustainable future.

Acknowledgments

This work was funded by the Bavarian Ministry of Economic Affairs and Media, Energy, and Technology through the project ZAE-ST (storage technologies). We thank Tobias Graf for his support with the electrochemical measurements and Hubert A. Gasteiger and Thomas J. Rabbow for valuable discussions.

ORCID

Tobias Greese https://orcid.org/0000-0002-7119-1647
Paulette A. Loichet Torres https://orcid.org/0000-0001-7304-9110

References

1. D. Aaron, Z. Tang, A. B. Papandrew, and T. A. Zawodzinski, "Polarization curve analysis of all-vanadium redox flow batteries." *J. Appl. Electrochem.*, **41**, 1175 (2011).
2. M. L. Perry and A. Z. Weber, "Advanced redox-flow batteries: a perspective." *J. Electrochem. Soc.*, **163**, A5064 (2015).
3. M. Ulaganathan, V. Aravindan, Q. Yan, S. Madhavi, M. Skyllas-Kazacos, and T. M. Lim, "Recent advancements in all-vanadium redox flow batteries." *Adv. Mater. Interfaces*, **3**, 1500309 (2016).
4. L. Yue, W. Li, F. Sun, L. Zhao, and L. Xing, "Highly hydroxylated carbon fibres as electrode materials of all-vanadium redox flow battery." *Carbon*, **48**, 3079 (2010).
5. B. Sun and M. Skyllas-Kazacos, "Chemical modification of graphite electrode materials for vanadium redox flow battery application—part II. Acid treatments." *Electrochim. Acta*, **37**, 2459 (1992).
6. H. Kabir, I. O. Gyan, and I. F. Cheng, "Electrochemical modification of a pyrolytic graphite sheet for improved negative electrode performance in the vanadium redox flow battery." *J. Power Sources*, **342**, 31 (2017).
7. H. Liu, L. Yang, Q. Xu, and C. Yan, "An electrochemically activated graphite electrode with excellent kinetics for electrode processes of V (II)/V (III) and V (IV)/ V (V) couples in a vanadium redox flow battery." *RSC Adv.*, **4**, 55666 (2014).
8. W. Zhang, J. Xi, Z. Li, H. Zhou, L. Liu, Z. Wu, and X. Qiu, "Electrochemical activation of graphite felt electrode for VO2+/VO2 + redox couple application." *Electrochim. Acta*, **89**, 429 (2013).
9. X. G. Li, K. L. Huang, S. Q. Liu, T. A. N. Ning, and L. Q. Chen, "Characteristics of graphite felt electrode electrochemically oxidized for vanadium redox battery application." *Transactions of Nonferrous Metals Society of China*, **17**, 195 (2007).
10. D. Dixon, D. J. Babu, J. Langner, M. Bruns, L. Pfaffmann, A. Bhaskar, and H. Ehrenberg, "Effect of oxygen plasma treatment on the electrochemical performance of the rayon and polyacrylonitrile based carbon felt for the vanadium redox flow battery application." *J. Power Sources*, **332**, 240 (2016).
11. L. Estevez, D. Reed, Z. Nie, A. M. Schwarz, M. I. Nandasiri, J. P. Kizewski, and B. Li, "Tunable oxygen functional groups as electrocatalysts on graphite felt surfaces for all-vanadium flow batteries." *ChemSusChem*, **9**, 1455 (2016).
12. K. J. Kim, Y. J. Kim, J. H. Kim, and M. S. Park, "The effects of surface modification on carbon felt electrodes for use in vanadium redox flow batteries." *Mater. Chem. Phys.*, **131**, 547 (2011).
13. P. C. Ghimire, R. Schweiss, G. G. Scherer, T. M. Lim, N. Wai, A. Bhattarai, and Q. Yan, "Optimization of thermal oxidation of electrodes for the performance enhancement in all-vanadium redox flow betteries." *Carbon*, **155**, 176 (2019).
14. A. M. Pezeshki, J. T. Clement, G. M. Veith, T. A. Zawodzinski, and M. M. Mench, "High performance electrodes in vanadium redox flow batteries through oxygen-enriched thermal activation." *J. Power Sources*, **294**, 333 (2015).
15. B. Sun and M. Skyllas-Kazacos, "Modification of graphite electrode materials for vanadium redox flow battery application—I. Thermal treatment." *Electrochim. Acta*, **37**, 1253 (1992).
16. Q. H. Liu, G. M. Grim, A. B. Papandrew, A. Turhan, T. A. Zawodzinski, and M. M. Mench, "High performance vanadium redox flow batteries with optimized electrode configuration and membrane selection." *J. Electrochem. Soc.*, **159**, A1246 (2012).
17. P. Mazúr, J. Mrlík, J. Beneš, J. Pocedič, J. Vrána, J. Dundálek, and J. Kosek, "Performance evaluation of thermally treated graphite felt electrodes for vanadium redox flow battery and their four-point single cell characterization." *J. Power Sources*, **380**, 105 (2018).
18. R. Schweiss, C. Meiser, and F. W. T. Goh, "Steady-state measurements of vanadium redox-flow batteries to study particular influences of carbon felt properties." *ChemElectroChem*, **4**, 1969 (2017).
19. M. A. Miller, A. Bourke, N. Quill, J. S. Wainright, R. P. Lynch, D. N. Buckley, and R. F. Savinell, "Kinetic study of electrochemical treatment of carbon fiber microelectrodes leading to in situ enhancement of vanadium flow battery efficiency." *J. Electrochem. Soc.*, **163**, A2095 (2016).
20. Y. Li, J. Parrondo, S. Sankarasubramanian, and V. Ramani, "Impact of surface carbonyl-and hydroxyl-group concentrations on electrode kinetics in an all-vanadium redox flow battery." *The Journal of Physical Chemistry C*, **123**, 6370 (2019).
21. N. Bevilacqua, L. Eifert, R. Banerjee, K. Köble, T. Faragó, M. Zuber, and R. Zeis, "Visualization of electrolyte flow in vanadium redox flow batteries using synchrotron X-ray radiography and tomography–Impact of electrolyte species and electrode compression." *J. Power Sources*, **439**, 227071 (2019).
22. T. J. Rabbow, M. Trampert, P. Pokorny, P. Binder, and A. H. Whitehead, "Variability within a single type of polyacrylonitrile-based graphite felt after thermal treatment. Part I: physical properties.." *Electrochimica Acta*, **173**, 17 (2015).
23. T. J. Rabbow, M. Trampert, P. Pokorny, P. Binder, and A. H. Whitehead, "Variability within a single type of polyacrylonitrile-based graphite felt after thermal treatment. Part II: chemical properties." *Electrochim. Acta*, **173**, 24 (2015).
24. X. Chu and K. Kinoshita, "Surface modification of carbons for enhanced electrochemical activity." *Materials Science and Engineering: B*, **49**, 53 (1997).
25. P. Mazúr, J. Mrlik, J. Pocedic, J. Vrána, J. Dundálek, J. Kosek, and T. Bystron, "Effect of graphite felt properties on the long-term durability of negative electrode in vanadium redox flow battery." *J. Power Sources*, **414**, 354 (2019).
26. I. Derr, A. Fetyan, K. Schutjajew, and C. Roth, "Electrochemical analysis of the performance loss in all vanadium redox flow batteries using different cut-off voltages." *Electrochim. Acta*, **224**, 9 (2017).
27. I. Derr, D. Przyrembel, J. Schweer, A. Fetyan, J. Langner, J. Melke, and C. Roth, "Electroless chemical aging of carbon felt electrodes for the all-vanadium redox flow battery (VRFB) investigated by electrochemical impedance and X-ray photoelectron spectroscopy." *Electrochim. Acta*, **246**, 783 (2017).
28. A. M. Pezeshki, R. L. Sacci, G. M. Veith, T. A. Zawodzinski, and M. M. Mench, "The cell-in-series method: A technique for accelerated electrode degradation in redox flow batteries." *J. Electrochem. Soc.*, **163**, A5202 (2015).
29. O. Nibel, S. M. Taylor, A. Pătru, E. Fabbri, L. Gubler, and T. J. Schmidt, "Performance of different carbon electrode materials: insights into stability and degradation under real vanadium redox flow battery operating conditions." *J. Electrochem. Soc.*, **164**, A1608 (2017).
30. T. Greese and G. Reichenauer, "Anode kinetics degradation in vanadium redox flow batteries–Reversible inhibition of the V2+/V3+-reaction due to V (II)-adsorption." *J. Power Sources*, **500**, 229958 (2021).
31. P. Mazúr, J. Mrlík, J. Beneš, J. Pocedič, J. Vrána, J. Dundálek, and J. Kosek, "Performance evaluation of thermally treated graphite felt electrodes for vanadium redox flow battery and their four-point single cell characterization." *J. Power Sources*, **380**, 105 (2018).
32. H. Fink, *Untersuchung von Verlustmechanismen in Vanadium-Flussbatterien*, Technische Universität München (2019), Doctoral dissertation https://mediatum.ub.tum.de/doc/1471866/1471866.pdf.
33. J. Langner, J. Melke, H. Ehrenberg, and C. Roth, "Determination of overpotentials in all vanadium redox flow batteries." *ECS Trans.*, **58**, 1 (2014).
34. C. N. Sun, F. M. Delnick, D. S. Aaron, A. B. Papandrew, M. M. Mench, and T. A. Zawodzinski Jr, "Resolving losses at the negative electrode in all-vanadium

redox flow batteries using electrochemical impedance spectroscopy." *J. Electrochem. Soc.*, **161**, A981 (2014).

35. J. Landesfeind, D. Pritzl, and H. A. Gasteiger, "An analysis protocol for three-electrode li-ion battery impedance spectra: Part I. analysis of a high-voltage positive electrode." *J. Electrochem. Soc.*, **164**, A1773 (2017).
36. J. H. Scofield, "Hartree-Slater subshell photoionization cross-sections at 1254 and 1487 eV." *J. Electron. Spectrosc. Relat. Phenom.*, **8**, 129 (1976).
37. A. Jablonski and C. J. Powell, *NIST Electron Effective-Attenuation-Length Database*, National Institute of Standards and Technology (2011), Doctoral Dissertation https://www.nist.gov/system/files/documents/srd/SRD82UsersGuideV1-3.pdf.
38. L. Eifert, R. Banerjee, Z. Jusys, and R. Zeis, "Characterization of carbon felt electrodes for vanadium redox flow batteries: Impact of treatment methods." *J. Electrochem. Soc.*, **165**, A2577 (2018).
39. J. L. Figueiredo, M. F. R. Pereira, M. M. A. Freitas, and J. J. M. Orfao, "Modification of the surface chemistry of activated carbons." *Carbon*, **37**, 1379 (1999).
40. B. Sun and M. Skyllas-Kazacos, "Modification of graphite electrode materials for vanadium redox flow battery application—I. Thermal treatment." *Electrochim. Acta*, **37**, 1253 (1992).
41. O. Di Blasi, N. Briguglio, C. Busacca, M. Ferraro, V. Antonucci, and A. Di Blasi, "Electrochemical investigation of thermically treated graphene oxides as electrode materials for vanadium redox flow battery." *Appl. Energy*, **147**, 74 (2015).
42. P. Chen, M. A. Fryling, and R. L. McCreery, "Electron transfer kinetics at modified carbon electrode surfaces: the role of specific surface sites." *Anal. Chem.*, **67**, 3115 (1995).
43. D. J. Johnson, "Structure and properties of carbon fibres." *In Carbon Fibers Filaments and Composites.* (Springer, Berlin: Dordrecht) 119 (1990).
44. S. Maass, F. Finsterwalder, G. Frank, R. Hartmann, and C. Merten, "Carbon support oxidation in PEM fuel cell cathodes." *J. Power Sources*, **176**, 444 (2008).
45. J. Langner, M. Bruns, D. Dixon, A. Nefedov, C. Wöll, F. Scheiba, and J. Melke, "Surface properties and graphitization of polyacrylonitrile based fiber electrodes affecting the negative half-cell reaction in vanadium redox flow batteries." *J. Power Sources*, **321**, 210 (2016).
46. C. E. Banks, T. J. Davies, G. G. Wildgoose, and R. G. Compton, "Electrocatalysis at graphite and carbon nanotube modified electrodes: edge-plane sites and tube ends are the reactive sites." *Chem. Commun.*, **7**, 829 (2005).
47. W. Yuan, Y. Zhou, Y. Li, C. Li, H. Peng, J. Zhang, and G. Shi, "The edge-and basal-plane-specific electrochemistry of a single-layer graphene sheet." *Sci. Rep.*, **3**, 1 (2013).
48. G. Wei, M. Jing, X. Fan, J. Liu, and C. Yan, "A new electrocatalyst and its application method for vanadium redox flow battery." *J. Power Sources*, **287**, 81 (2015).
49. N. Pour, D. G. Kwabi, T. Carney, R. M. Darling, M. L. Perry, and Y. Shao-Horn, "Influence of edge-and basal-plane sites on the vanadium redox kinetics for flow batteries." *The Journal of Physical Chemistry C*, **119**, 5311 (2015).
50. T. J. Rabbow and A. H. Whitehead, "Deconvolution of electrochemical double layer capacitance between fractions of active and total surface area of graphite felts." *Carbon*, **111**, 782 (2017).
51. J.-P. Randin and E. Yeager, "Differential capacitance study of stress-annealed pyrolytic graphite electrodes." *J. Electrochem. Soc.*, **118**, 711 (1971).
52. J. P. Randin and E. Yeager, "Differential capacitance study on the basal plane of stress-annealed pyrolytic graphite." *J. Electroanal. Chem. Interfacial Electrochem.*, **36**, 257 (1972).
53. J. P. Randin and E. Yeager, "Differential capacitance study on the edge orientation of pyrolytic graphite and glassy carbon electrodes." *J. Electroanal. Chem. Interfacial Electrochem.*, **58**, 313 (1975).
54. D. M. Kabtamu, J. Y. Chen, Y. C. Chang, and C. H. Wang, "Water-activated graphite felt as a high-performance electrode for vanadium redox flow batteries." *J. Power Sources*, **341**, 270 (2017).
55. I. Derr, M. Bruns, J. Langner, A. Fetyan, J. Melke, and C. Roth, "Degradation of all-vanadium redox flow batteries (VRFB) investigated by electrochemical impedance and X-ray photoelectron spectroscopy: Part 2 electrochemical degradation." *J. Power Sources*, **325**, 351 (2016).

4.2. Anode Kinetics Degradation in Vanadium Redox Flow Batteries – Reversible Inhibition of the V^{2+}/V^{3+}-Reaction due to V(II)-Adsorption

The article "Anode Kinetics Degradation in Vanadium Redox Flow Batteries – Reversible Inhibition of the V^{2+}/V^{3+}-Reaction due to V(II)-Adsorption"[33] was submitted in December 2020 and published in the peer-reviewed *Journal of Power Sources* in March 2021. The article was distributed under the terms of the Elsevier subscription model, which permits authors to include the article in their dissertation, provided it is not published commercially and the original work is properly cited. The permanent weblink to the article is https://doi.org/10.1016/j.jpowsour.2021.229958.

This publication suggests an explanation for the commonly observed VRFB anode kinetics degradation. It shows that the degradation results from the adsorption of V^{2+} accumulating on the electrode surface until an equilibrium coverage is established. As a result, the inhibiting V(II)-adsorption explains several features of electrode behavior that hitherto appeared inconsistent but now provide a coherent picture. In RDE half-cells, it was observed that the kinetics of graphitic anodes decreased when contacting vanadium-containing aqueous sulfuric acid electrolyte at potentials < -0.2 V vs. RHE. In contrast, resting at anodic potentials of 1.0 V vs. RHE regenerated the anode kinetics. Moreover, especially the presence of bi-valent vanadium (V(II)) led to the inhibition of the hydrogen evolution reaction (*HER*) in sulfuric acid. The new concept of an adsorption mechanism was transferred to VRFB symmetric and regular full-cells. Here, the rate of the increase of R_{ct} became slower over time, confirming the formation of a V(II)-equilibrium coverage. Moreover, resting at oxidative electrode potentials caused reversible anode kinetics regeneration. Especially the latter reversibility implies that reversing the electrode polarity in regular cells will restore the degraded electrode performance to its initial levels. Such regenerating operating strategies can increase the average anode kinetics and ensure reversibly high VRFB performance over the battery lifetime.

Author contributions

T.G. developed the VRFB single-cell design and the cell test environment enabling stable system operating parameters. T.G. performed the electrochemical investigation and validation and evaluated the experimental results. T.G. developed the concept, the methodology, the visualization and wrote the manuscript. G.R. revised and edited the manuscript.

Journal of Power Sources 500 (2021) 229958

Contents lists available at ScienceDirect

Journal of Power Sources

journal homepage: www.elsevier.com/locate/jpowsour

Anode kinetics degradation in vanadium redox flow batteries – Reversible inhibition of the V^{2+}/V^{3+}-reaction due to V(II)-adsorption

Tobias Greese [a,*], Gudrun Reichenauer [b]

[a] *Bayerisches Zentrum für Angewandte Energieforschung, Division Energy Storage, Walther-Meissner-Str. 6, 85748, Garching, Germany*
[b] *Bayerisches Zentrum für Angewandte Energieforschung, Division Energy Efficiency, Magdalene-Schoch-Straße 3, 97074, Würzburg, Germany*

HIGHLIGHTS

- New mechanism for anode degradation in vanadium redox flow batteries proposed.
- V(II) adsorbs to carbon surface inhibiting hydrogen evolution and V^{2+}/V^{3+}-reaction.
- Adsorbed V(II) reversibly oxidizable leading to recovered surface activity.
- VRFB performance restored by polarity reverse in symmetric and regular full-cells.

GRAPHICAL ABSTRACT

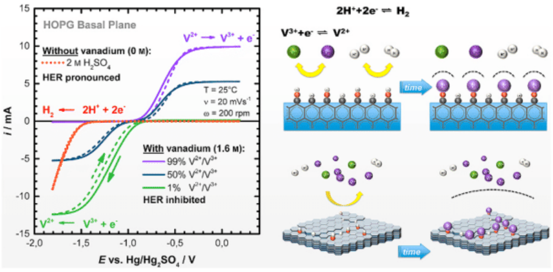

ARTICLE INFO

Keywords:
V(II)-Adsorption
Hydrogen evolution reaction (HER)
V^{2+}/V^{3+}-reaction inhibition
Highly-oriented pyrolytic graphite (HOPG)
Carbon anode kinetics degradation
Vanadium redox flow batteries (VRFB)

ABSTRACT

Vanadium redox flow batteries (VRFB) typically show performance degradation due to V^{2+}/V^{3+}-reaction activity deterioration on their carbon anodes. The reason for the deterioration has not yet been identified. Employing different graphite rotating-disk electrodes, we demonstrate that V^{2+} inhibits the hydrogen evolution reaction (HER). Our findings suggest that V^{2+} adsorbs at cathodic potentials and deactivates the HER. Analogously, the V^{2+}-adsorption deteriorates the V^{2+}/V^{3+}-activity, causing the VRFB performance degradation. With graphite felts in symmetric and full-cells, we demonstrate that the slowly degrading anode activity reflects an inhibiting V^{2+}-coverage formation. As the rate of degradation decelerates, the coverage approaches equilibrium. We restored the V^{2+}/V^{3+}-activity by reversing the electrode polarity, representing V^{2+}-desorption. At anodic potentials, the adsorbed V^{2+} liberates the surface, which we also confirmed in half-cells. Here, in vanadium-free sulfuric acid, the HER and V^{2+}/V^{3+}-activity recovered already below −0.26 V vs. NHE due to the Nernst shift. Our findings facilitate the understanding of several features of VRFB electrode behavior. Moreover, they promote operational strategies upon which the VRFB performance can be entirely restored and considerably increased.

1. Introduction

Vanadium redox-flow batteries (VRFB) promise an environmentally-friendly way for stationary energy storage. Their broad economic acceptance depends on low manufacturing and operating costs requiring the battery to function at high voltage efficiency over its whole lifetime.

---

[*] Corresponding author.
E-mail addresses: tobias.greese@zae-bayern.de, tobias.greese@gmx.de (T. Greese).

https://doi.org/10.1016/j.jpowsour.2021.229958
Received 10 December 2020; Received in revised form 31 March 2021; Accepted 21 April 2021

Indeed, after prolonged battery operation, the voltage efficiency appears nearly stable. However, especially within the first weeks of operation, the efficiency decreases by several percent [1–3]. Although the rate of decrease decelerates with operation time, it is difficult to estimate the final value upon which the efficiency will ultimately drop [1,2,4]. Monitoring the anode and cathode reaction kinetics independently showed that the efficiency decreases due to a slowly increasing anode charge-transfer resistance (R_{ct}) for the V^{2+}/V^{3+}-reaction [2,5]. Although the increasing R_{ct} indicates a deterioration in catalytic anode activity, the search for its cause has been unsuccessful [6].

Bourke et al. showed that the activity depends strongly on the electrode treatment potential. When alternately exposed to anodic and cathodic potentials (+2.1 V and −1.4 V vs. NHE), the V^{2+}/V^{3+}-activity toggled reversibly on and off [7,8]. The activity increase was assigned to surface oxides formed at the anodic potentials catalyzing the V^{2+}/V^{3+}-reaction [9,10]. Correspondingly, cathodic potentials may have caused a surface reduction and destruction of the oxides. Indeed, x-ray photoemission spectroscopy (XPS) revealed fewer surface oxides present after the cathodic treatment [11,12]. The electrochemical (EC) anode potential is typically in the reducing regime between −0.4 and −0.1V vs. NHE. At these potentials, it is conceivable that, during continuous VRFB operation, the surface oxides are reduced to water and leave the surface. Consequently, a loss of oxides would explain the observed VRFB anode activity deterioration.

However, recent studies employing XPS on degraded VRFB anodes could not confirm a loss of surface oxides. Instead, the concentration of surface keto (C=O) and phenol groups (C–OH) slightly increased [1,4,5,13]. Besides, no loss in carbon material was detected. Only the amount of sp^3-hybridized carbon increased in exchange for sp^2-carbon. Hence, sp^3-carbon was a primary candidate decreasing the activity, as it is associated with a lower surface layer conductivity [1,5]. However, the conversion of ordered sp^2-into disordered sp^3-carbon is irreversible. In contrast, the activity varies reversibly with potential, which argues strongly against sp^3-carbon as the leading cause for activity deterioration. Therefore, the search for the cause of degradation remained opened.

Another intriguing detail attracts attention. Several studies observed that the reduction of V^{3+} on graphite electrodes competes with and partially inhibits the hydrogen evolution reaction (HER), showing most on oxidized surfaces [3,10,14]. However, the feature was perceived beneficial only in restricting the parasitic HER. So far, no study has considered that the latter and all yet described features are related.

This study identifies V^{2+} to cause the HER inhibition. By employing glassy carbon (GC) and highly-oriented pyrolytic graphite (HOPG) in basal and edge orientation as rotating-disk electrodes (RDE) in three-electrode half-cells, we correlate V^{2+} with the HER inhibition and the V^{2+}/V^{3+}-activity deterioration. A newly proposed degradation mechanism combines multiple features of characteristic electrode behavior. Accordingly, V^{2+} binds to carbon reaction sites and thus inhibits the HER and the V^{2+}/V^{3+}-reaction. This adsorbant ultimately explains the slowly degrading but restorable VRFB cell performance. Using graphite felt electrodes in VRFB full-cells, we illustrate the mechanism and its practical relevance, combining the cell-in-series technique [4] with symmetric cells [15]. Finally, we demonstrate operating strategies for liberating the surface from the inhibiting V^{2+}, thus restoring the original battery performance.

2. Materials and methods

2.1. Half-cell measurements – three-electrode setup

VRFB graphitic anode kinetics suffers upon contact with V^{2+}/V^{3+}-electrolyte. Using V^{2+}-, V^{3+}-, and VO^{2+}-electrolyte, we examined RDE model surfaces being GC and basal- and edge-plane oriented HOPG. As potentiostat, we used an SP-240 (Bio-Logic, France) to perform cyclic voltammetry (CV) and electrochemical impedance spectroscopy (*EIS*).

The half-cell was a glass compartment comprising three electrodes. A Hg/Hg_2SO_4 reference electrode (SI Analytics, Mettler-Toledo) referred to 0.674 V vs. the normal hydrogen electrode (NHE) as a reference potential. Working electrodes (WE) were cast-in graphite disks mounted in RDE tips. The RDE tips, disks, and associated equipment (rotating shaft, rotator, and control module) were all supplied by PINE Instruments, USA. The graphite disks were HOPG in basal plane and HOPG in edge plane orientation with 4-mm-diameter each, accounting for an active area of 0.126 cm^2. The GC disk was a 5-mm-disk, providing for 0.196 cm^2. The counter electrode was graphite felt with a 2 cm^2 geometric area, impaled by a carbon fiber composite stick. With a gravimetric carbon surface area of 0.5 m^2_{carbon} g^{-1} and a geometric areal weight of 500 g m^{-2}_{geo}, the counter electrode provided about 500 cm^2_{carbon}, which far exceeded the areas of the three WE types.

Before each experiment, we polished the GC by 50 nm Al_2O_3 polishing paste and cleaned it with 5 min ultrasonication in Milli-Q® water (Merck, Germany). However, the polishing paste might have introduced contaminants inferring with the experimental results. Therefore, we employed HOPG in basal plane orientation, the surface of which we renewed by exfoliation with adhesive tape. This method provided reproducible and pristine surfaces. We submitted the RDE tip to a 5 min plasma treatment in a PlasmaFlecto 10 low-pressure plasma chamber (Plasma Technologies GmbH, Germany) if not stated otherwise (Fig. 7). The plasma treatment enhanced the graphite surface activity for the V^{2+}/V^{3+}-reaction [16,17]. With enhanced activity, smaller overpotentials were sufficient to reach the diffusion-limited currents, which helped distinguish between the HER and V^{2+}/V^{3+}-reaction.

2.2. Half-cell measurements – electrolyte preparation

We prepared the 2 M aqueous sulfuric acid electrolyte by diluting 95.0–98.0% sulfuric acid (ACS reagent, Merck KGaA, Germany) with Milli-Q® water (18.2 MΩ cm, Merck KGaA, Germany). The vanadium (V) electrolyte (GfE GmbH, Germany) was 1.6 M $[V(III)]_2(SO_4)_3/[VO(IV)](SO_4)$ (1:1) in 2 M aqueous sulfuric acid with 30–50 mM phosphoric acid (H_3PO_4), hereafter referred as to V^{3+}/VO^{2+}-electrolyte. The phosphoric acid (30–50 mM) serves as a precipitation inhibitor for V^{3+} and VO^{2+} at elevated temperatures > 40 °C [6]. Using a conditioning VRFB full-cell (assembled as described below), we charged the 1.6 M V^{3+}/VO^{2+}-electrolyte close to 100% state-of-charge (SoC), generating a nearly pure V^{2+}-electrolyte. For adjusting different V^{2+}/V^{3+}-ratios and concentrations, we added small amounts of charged and uncharged electrolytes. The glass cell had a water-jacket connected to an A100 bath thermostat (Thermo Fisher Scientific, Germany). Before each experiment, the electrolyte was purged with N_2 gas for 20 min to remove residual O_2. During the experiment, a blanketing N_2 stream covered the electrolyte at a constant flow of 30 ml min^{-1}.

2.3. Full-cell measurements – cell assembly

For demonstrating the practical relevance of the variable electrode kinetics in V^{2+}/V^{3+} and VO^{2+}/VO_2^+ electrolyte, we employed a VRFB full-cell assembly (Fig. SI 1) with 25 cm^2 GFD4.6 electrodes (SGL Carbon, Germany). We plasma-treated the electrodes for 5 min (as described above), improving their electrolyte saturation. Otherwise, untreated electrodes occasionally showed reduced electrode-electrolyte contact area due to gas inclusions, compromising experimental reproducibility [18,19]. We then assembled the yet dry electrodes to monitor the electrode kinetics, starting from the first electrolyte contact.

2.4. Full-cell measurements – test setup and procedure

The measurement procedure was a sequence of repetitive *EIS* throughout 24 h. As a potentiostat, we used a PGSTAT302 N with 20A Booster (Metrohm Autolab, Germany). We fitted the *EIS* Nyquist diagrams with the EC-Lab Z Fit software (Bio-Logic, France).

Before connecting the test cell to the system, we used an identical conditioning cell to precharge the electrolyte to a state-of-charge (SoC) of 50%. The SoC correlates with the open-circuit-voltage (*OCV*) (Fig. SI 2), which we monitored in-operando using an *OCV*-cell [20]. N_2 gas purge removed O_2 from both electrolyte compartments continuously throughout all experiments. Fig. SI 3 depicts a functional diagram of the test environment representing the electrolyte flow and the measurement and control system. The electrolyte passed through a customized plate heat exchanger coupled to an A100 bath thermostat (Thermo Fisher Scientific, Germany). Fluor-ethylene-propylene(FEP)-coated Pt100 thermometers (TC GmbH, Germany) measured the electrolyte temperature in-line, mounted in customized PVC-tubes. Corresponding to the measured temperature, PID controllers in a LabView logic adjusted NF60 membrane pumps (KNF Neuberger, Germany) pumping through the heat exchanger. This way, the electrolyte temperature stayed at a constant temperature of 20 ± 0.2 °C throughout all experiments. VZS005-PP in-line oval-wheel flowmeters (B.I.O.-TECH, Germany) measured the electrolyte flow entering the test cell. Similar to the temperature, the flow rate was set constant by PID-controlled NF60 membrane pumps.

3. Results and discussion

3.1. Half-cell measurements – 1.6 M V^{2+}/V^{3+} at SoC 50%

We investigated the CV response of a HOPG RDE in a half-cell containing 1.6 M V^{2+}/V^{3+} electrolyte at a V^{2+}/V^{3+}-ratio of 1/1. In Fig. 1a, we cycled the potential between −1.8 V and 0.2 V at a scan rate of 20 mV s^{-1}. The electrolyte temperature was 25 °C and the rotation rate 200 rpm. The mercury/mercurous sulfate (Hg/Hg_2SO_4) reference electrode, filled with 1.0 M aq. sulfuric acid (H_2SO_4), has its standard potential at $E^0\ (Hg/Hg_2SO_4) = 0.674$ V vs. NHE [21]. Consequently, we expected the standard potential of the V^{2+}/V^{3+} reaction $E^0\ (V^{2+}/V^{3+})$ at −0.255–0.674 V = −0.929 V vs. Hg/Hg_2SO_4. We measured an open-circuit-potential (*OCP*) of −0.936 V, implicating a V^{2+}/V^{3+}-ratio close to 1/1.

In Fig. 1a, at potentials $E < -1.3$ V and $E > -0.6$ V, the currents follow a sigmoidal wave entering the diffusion-limited regime. Here, the currents i_{lim} are constant, indicating complete conversion of educts (V^{2+} or V^{3+}) transferred to the electrode surface. The height of i_{lim} corresponds to the educt flux reaching the surface. First, upon constant RDE rotation ensuring steady mass transport, the educt enters the electrode surface vicinity due to forced convection. Subsequently, the educt crosses the diffusion layer, with its thickness attuned by the rotation rate. The interplay between forced convection and diffusion leading to i_{lim} is described by the Levich equation [22]. Accordingly, i_{lim} is proportional to the square root of the rotation rate. In Fig. SI 4, this behavior is experimentally observed when varying the rotation rate between 100 rpm and 1600 rpm.

At potentials $-1.3\text{ V} < E < -0.6$ V, the currents show an exponential characteristic, mainly representing the charge-transfer kinetic current i_{kin} described by the Butler-Volmer equation [20].

$$i_{\text{kin}} = i_0 \left\{ \exp\left[\frac{\alpha_a F}{RT}\eta\right] - \exp\left[\frac{-\alpha_c F}{RT}\eta\right] \right\} \tag{1}$$

Eq. (1) comprises the exchange-current density i_0, the anodic and cathodic charge-transfer coefficients α_a and α_c, the Faraday constant F, the universal gas constant R, and the temperature T. The overpotential η is the difference $E - E_0$ of the applied potential E and the equilibrium potential E_0, or *OCP*. Ideally, the measured current is independent of the voltage scan direction.

On closer inspection, though, there is a pronounced hysteresis between the anodic and the cathodic scan in Fig. 1a. Especially evident around *OCP* in the upper inset in Fig. 1a, the cathodic scan shows a steeper slope (orange line) than the anodic scan (blue dashes).

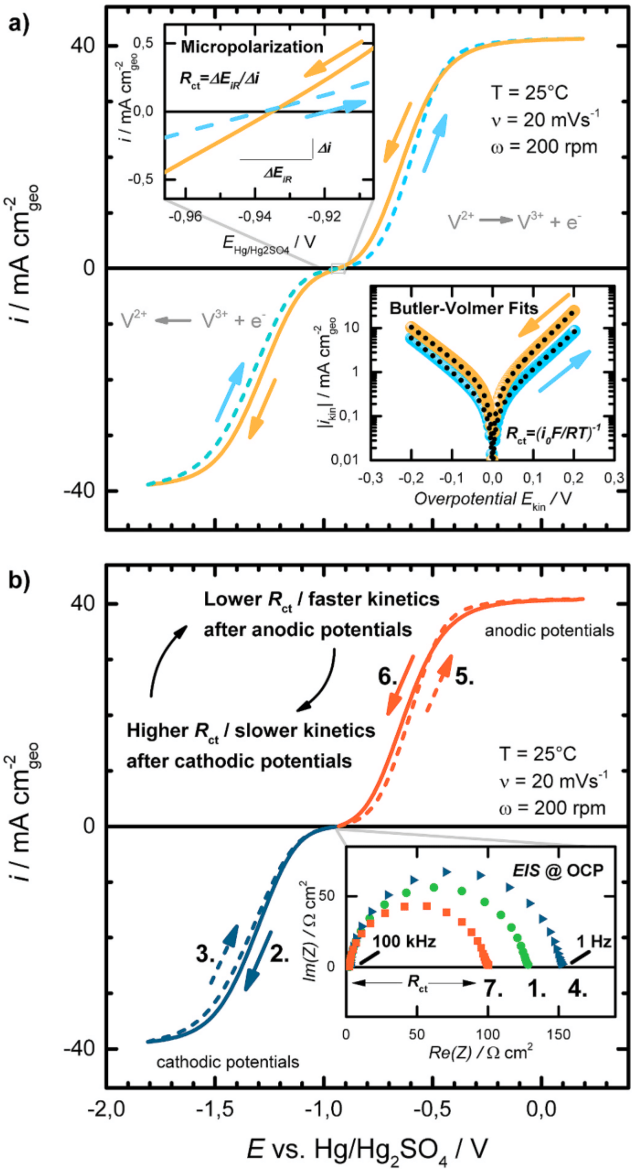

Fig. 1. Basal plane HOPG-RDE in 1.6 M V^{2+}/V^{3+} with a V^{2+}/V^{3+}-ratio of 1/1, at 25 °C electrolyte temperature, and 200 rpm rotation rate. a) CV between E = [-1.8; 0.2] V at 20 mV s^{-1} scan rate reveal slower charge-transfer kinetics (higher R_{ct}) during the scan in anodic than in cathodic direction (dashed and solid lines). The kinetics manifest in the micropolarization region around OCP (upper left inset in a), linear fits) and in the Butler-Volmer fit region (lower right inset in a), black dots). b) Sequence of EIS and CV: (1.): EIS at OCP (−0.935 V) (inset, green dots). (2./3.): CV scanning cathodically from OCP to −1.8 V and back to OCP (blue lines). (4.): EIS at OCP (inset, blue triangles). (5./6.): CV scanning anodically from OCP to 0.2 V and back to OCP (red lines). (7.): EIS at OCP (inset, red squares). Nyquist fitting to a Randles circuit revealed a variable kinetic activity, deteriorated after cathodic and enhanced after anodic scans. (For interpretation of the references to color in this figure legend, the reader is referred to the Web version of this article.)

We assessed the charge-transfer kinetics by three different analytical approaches, summarized in Table 2 and expressed as charge-transfer resistance R_{ct}. First, we linearized the Butler-Volmer equation in the *micropolarization* region around *OCP*. For small overpotentials $\eta \pm 10$ mV, the educt concentration on the electrode surface equals the one in the bulk electrolyte ($c^s_{\text{red}} \approx c^o_{\text{red}}$). Taylor series expansion of the exponential terms ($\exp(x) = 1 + x$) and assuming $\alpha_a = 1 - \alpha_c = \alpha$ simplifies

Table 1

Charge-transfer resistance R_{ct} derived in three ways: from the CV slope $\Delta E/\Delta I$ in the micropolarization region ±10 mV around OCP (c.f., magnification of OCP region in Fig. 1a), from Butler-Volmer fitting the kinetic current-potential-curve (c.f., Tafel plots in Fig. 1a), and from fitting the EIS spectra to a Randles circuit (c.f., Nyquist plot in Fig. 1b).

	Charge-transfer resistance fitted by		
	Micropolarization	Butler-Volmer	Randles circuit
Electrode after		R_{ct}/Ω cm^2	
cathodic potentials	155	145	147
anodic potentials	65	64	96

Table 2

Electrode resistances R_{ct} determined by EIS for the three different types of WE, i.e., basal plane HOPG, edge plane HOPG, and GC (see Fig. 1b and Fig. SI 5b, d, and f).

	Basal HOPG	Edge HOPG	Glassy carbon
Preceding electrode potential		R_{ct}/Ω cm^2	
OCP	123	31	48
negative potentials	147	55	142
positive potentials	96	28	47

Eq. (1) to

$$i = i_0 \frac{F}{RT}\eta \tag{2}$$

We *iR*-corrected the measured potential for the ohmic solution resistance R_Ω ($\eta = E - iR_\Omega$) and derived R_{ct} from linearly fitting the *micropolarization* region using the correlation

$$R_{ct} = \left(i_0 \frac{F}{RT}\right)^{-1} \tag{3}$$

$$= \frac{d\eta}{di} = \frac{\Delta(E - iR_\Omega)}{\Delta i}$$

Second, we analyzed the *Butler-Volmer* region within ±200 mV around *OCP*. At these elevated overpotentials, mass transfer became more significant. Consequently, the educt concentrations at the electrode c^s and in the electrolyte c^0 could not be assumed equal anymore. Instead, the measured potential carried an additional concentration overpotential η_c. Also, the measured current was smaller than the kinetic current. We corrected both current and potential for the mass transfer-induced shift in concentration [23] to receive the kinetic current and potential i_{kin} vs. η_{kin} derived in the supporting information. Curve fitting of i_{kin} vs. η_{kin} according to Eq. (1) delivered values for the parameters i_0, α_a, and α_c. The conversion of i_0 to R_{ct} according to Eq. (3) and the comparison in Table 2 shows that the evaluation of the *micropolarization* and *Butler-Volmer* region yielded comparable kinetics for the respective scans within a 3% standard deviation. The Tafel plot in the lower inset of Fig. 1a appears symmetric, indicating the charge-transfer coefficient α being close to 0.5. Also, the fit results confirmed this symmetry by determining $\alpha = (\alpha_a + \alpha_c)/2$ to $\alpha = 0.48$ for the cathodic scan and $\alpha = 0.47$ for the anodic scan. Consequently, the anodic and cathodic charge-transfer rates are balanced, not explaining the observed hysteresis.

Third, we derived R_{ct} directly by *EIS* combined with preceding *CV*s. The Nyquist inset in Fig. 1b shows three semi-circles (green dots, blue triangles, and red squares). Randles circuit fits of the semi-circles assigned most of the total resistance to charge-transfer R_{ct}, accounting for 123 Ω cm^2 in the initial *EIS* at *OCP* (green dots). Subsequently, we scanned the potential from *OCP* cathodically to $E = -1.8$ V (2.) and back to *OCP* (3.). Recording another *EIS* at *OCP* (4.) revealed an R_{ct} of 147 Ω cm^2, a value about 20% larger than after the first *EIS*. Next, we scanned the potential from *OCP* anodically to 0.2 V (5.) and back to *OCP* (6.). In the *EIS* (7.), we recorded an R_{ct} of 96 Ω cm^2, only 2/3 of the R_{ct} after cathodic potentials.

Comparing the resulting R_{ct} from the three analytical approaches, the *EIS*-derived R_{ct} deviated from the R_{ct} derived by *CV*, especially after anodic potentials (c.f., Table 1). However, considering the *EIS* recording time of 30 s at *OCP*, the difference is reasonable. During that time, the electrode rested at −0.26 V vs. NHE, a potential related to activity deterioration. By contrast, after scanning to cathodic potentials, when giving the electrode some time during consecutive *EIS*, the kinetics even slightly recovered over time.

Complementary, we verified the same behavior on two more graphite materials, i.e., HOPG in the edge plane orientation and glassy carbon (GC), following the same protocol as in Fig. 1. The advantage of using basal plane HOPG is that its surface is fully reproducible upon cleavage. Also, no foreign matter is involved, such as residual polishing paste. However, McCreery et al., Compton et al. and Unwin et al. have shown that basal plane HOPG can exhibit vastly different electrochemical behavior than edge plane HOPG or GC [9,17,24]. Hence, for comparison, Fig. SI 5 illustrates the experiment of Fig. 1 for all three (sp^2)-carbon materials (basal plane HOPG, edge plane HOPG, and GC). Indeed, the three materials comprised different kinetic activities discussed as follows. Basal plane HOPG showed slower V^{2+}/V^{3+}-kinetics than edge plane HOPG, as reported in the literature and summarized in Table 1 [25]. Also, as commonly observed, basal plane HOPG kinetics were generally slower than on GC [26]. However, GC kinetics is more sensitive to the preceding electrode potential. When coming from positive potentials, basal HOPG kinetics indeed is half the one on GC. Though, after negative potentials, the kinetics on GC and basal plane HOPG are similar. This sensitivity might be due to surface properties inherent to GC, such as surface pores or the fullerene-related structure incorporating non-six-membered carbon rings [27].

We conclude that different materials show similar *CV* responses, including the variable activity triggered by anodic and cathodic potentials. Scanning to cathodic potentials deactivates the electrode surface for the V^{2+}/V^{3+}-reaction. Accordingly, the anodic scan has the opposite effect. Similar behavior was reported by Bourke et al. [7] and Miller et al. [11]. Resting for 60 s at anodic potentials of 1.5 V vs. Hg/Hg_2SO_4 (2.1 V vs. NHE) or cathodic potentials of −2.0 V vs. Hg/Hg_2SO_4 (−1.4 V vs. NHE) distinctly activated or deactivated the electrode, respectively. Repetition moreover revealed high reversibility. Based on XPS results, the researchers suggested the activity changed due to surface oxide formation and destruction. However, in the current and referenced studies, the electrode polarization occurred in the presence of 1.6 M V^{2+}/V^{3+}, suggesting a vanadium involvement leading to the hysteresis. For clarifying the role of vanadium, we assay the electrode kinetics at altered V^{2+}/V^{3+}-ratio and V-concentration in the following sections.

3.2. Half-cell measurements – 1.6 M V^{2+}/V^{3+} at SoC 99%, 50%, and 1%

Fig. 2 compares *CV*s of basal plane HOPG in vanadium-free 2 M H_2SO_4 and 1.6 M V^{2+}/V^{3+} at different V^{2+}/V^{3+}-ratios. Edge plane HOPG and GC responded correspondingly, shown in Fig. SI 7.

The dotted red line representing three cycles in vanadium-free 2 M H_2SO_4 indicated a pronounced reduction current below −1.3 V due to vivid hydrogen evolution, according to $2H^+ + 2e^- \rightarrow H_2$. Coinciding with the reduction current, hydrogen bubbles formed in the transparent electrolyte. Higher electrode rotational speed increased the HER current only marginally. Likely, the more vigorous forced convection removed more H_2 bubbles from the surface, decreasing the local H_2 concentration overpotential [28,29].

The purple curve represents a *CV* in 1.6 M V^{2+}/V^{3+} at 99% V^{2+}/V^{3+}-ratio. Analogously, the green curve referred to a V^{2+}/V^{3+}-ratio of 1%, indicated by the diffusion-limited currents ratio for V^{2+}-oxidation and V^{3+}-reduction. Fig. SI 6 comprises CVs at additional V^{2+}/V^{3+}-ratios between 99 and 1% and a more in-depth analysis of the limited currents

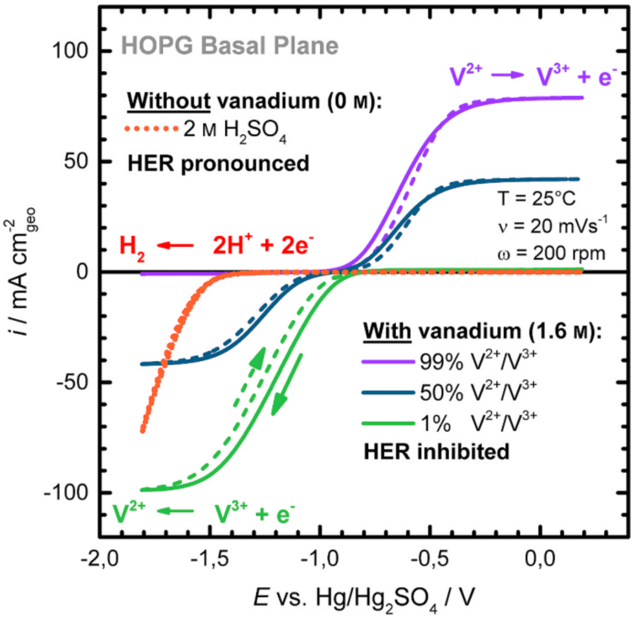

Fig. 2. Cyclic voltammograms of basal plane HOPG-RDE in 2 M H_2SO_4 containing 1.6 M V^{2+}/V^{3+} at different V^{2+}/V^{3+}-ratios of 99% (purple), 50% (blue), and 1% (green), compared with vanadium-free 2 M H_2SO_4 electrolyte (red curve). The electrolyte temperature was 25 °C, the scan rate at 20 mV s$^{-1,}$ and the rotation rate at 200 rpm. (For interpretation of the references to color in this figure legend, the reader is referred to the Web version of this article.)

and their associated *OCP*s. A comparison of measured and calculated data revealed good agreement of experiment and theory.

At $E < -1.0$ V, the purple curve developed no cathodic current for V^{3+}-reduction. However, most surprisingly, also the HER current entirely disappeared. Similarly, HER inhibition was evident by constant diffusion-limited currents, disregarding the V^{2+}/V^{3+}-ratio.

Up to this point, this observation could have different origins. Speculatively, electrolyte contaminants may have caused electrode poisoning hindering H^+ ions from adsorbing and combining to H_2. A possible source for contaminants was the VRFB full-cell setup, used for preparing the V^{2+}/V^{3+}-electrolyte by charging V^{3+}/VO^{2+}. The setup involved the tubing, pumps, tanks, and the full-cell. Other contaminants to be considered are those contained natively in the electrolyte. Other than that, vanadium itself may be involved in HER inhibition. In this case, to be identified is which vanadium species caused the inhibition and at which concentration.

3.3. Half-cell measurements – increased V^{3+}/VO^{2+}- and V^{2+}/V^{3+}-concentration

For determining the vanadium concentration sufficient for HER inhibition, we step-wise increased the V^{3+}/VO^{2+}-concentration. Although focusing on basal plane HOPG, we again validated the results on edge plane HOPG and GC, presented in Fig. SI 8.

Starting with vanadium-free aq. 2 M H_2SO_4, we pipetted commercial 1.6 M V^{3+}/VO^{2+} into the H_2SO_4 and concomitantly recorded the *CV* polarization curve (Fig. 3a). Below −1.3 V, hydrogen bubbles formed continuously, with a V^{3+}/VO^{2+} concentration of 0 mM (orange line) and still with 0.5/0.5 mM (red dots) and 5/5 mM (blue dashes).

With 50/50 mM V^{3+}/VO^{2+} (green line), the *CV* appearance below −1.1 V fundamentally changed. While the cathodic current started earlier, the curve was much flatter, indicating the reaction's nature changed. The cathodic current linearly increased when quadratically increasing the rotation rate, being characteristic for mass-transport control (c.f., Fig. SI 8b, d, and f). Also, the bubble formation on the electrode surface had stopped. Conclusively, instead of HER, now the cathodic current reflected VO^{2+}- and V^{3+}-reduction. At zero rotation, the *CV* revealed an anodic peak at −0.45 V representing the oxidation of V^{2+} formed by V^{3+}-reduction during the previous cathodic scan.

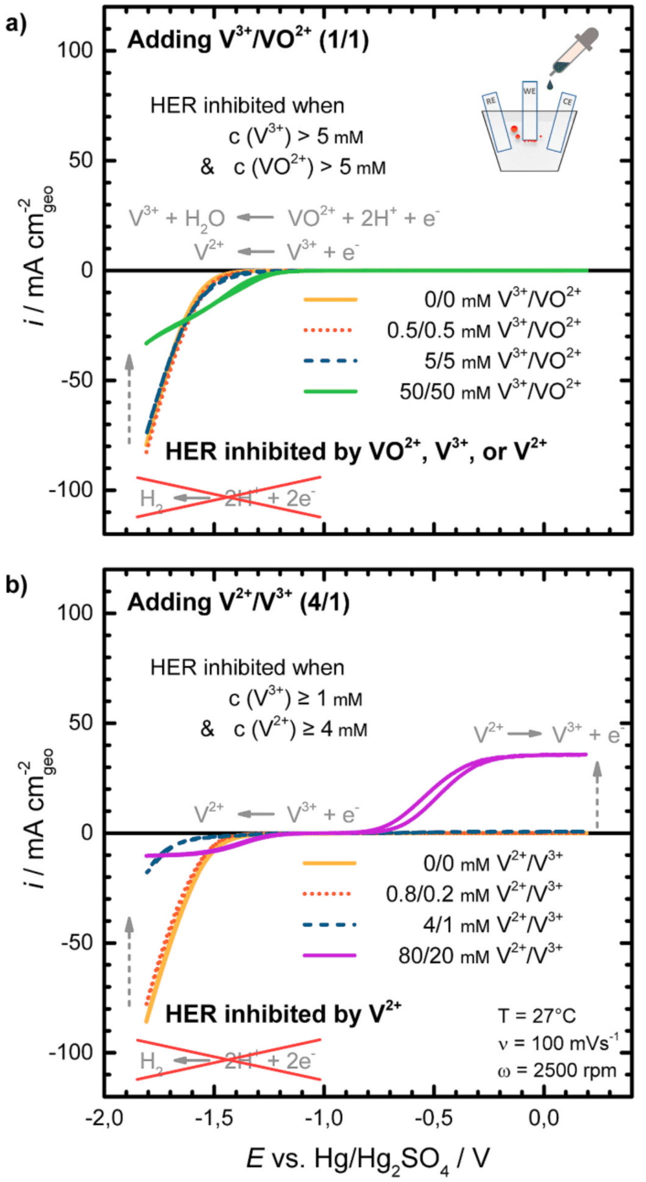

Fig. 3. Cyclic voltammograms of basal plane HOPG-RDE in 2 M H_2SO_4. a) Impact of step-wise increasing the concentrations of V^{3+}/VO^{2+} electrolyte. Representatively, we show 1, 10, and 100 mM V^{3+}/VO^{2+} in 2 M H_2SO_4 as we cycled the electrode potential between E = [-1.8; 0.2] V at a scan rate of 100 mV s^{-1} and a rotation rate of 2500 rpm. b) At identical experimental conditions, we step-wise increased the concentrations of V^{2+}/V^{3+} electrolyte. Representatives are CVs in 1, 5, and 100 mM V^{2+}/V^{3+} in 2 M H_2SO_4.

This first part of the experiment allows for different conclusions. First, commercial V^{3+}/VO^{2+}-electrolyte inhibits hydrogen evolution. No external contaminants could be responsible since the electrolyte was not in contact with the VRFB full-cell setup. Furthermore, HER inhibition required a threshold concentration of more than 10 mM V^{3+}/VO^{2+}. However, VO^{2+}, $V^{3+,}$ and V^{2+} were present on the electrode surface. Thus, identifying which vanadium species was responsible for the inhibition remained unfeasible.

To isolate the most contributing species, we repeated the experiment.

Again starting with vanadium-free aq. 2 M H_2SO_4, this time we increased the V^{2+}/V^{3+}-concentration, with V^{2+}/V^{3+} at a ratio of 4/1 (Fig. 3b). Hydrogen bubbles formed undisturbed, yet only up to a concentration of 0.8/0.2 mM V^{2+}/V^{3+} (red dots). At 4/1 mM V^{2+}/V^{3+}, the HER collapsed to 20% (blue dashes) and eventually vanished at 80/20 mM V^{2+}/V^{3+} (purple line).

In summary, we found that only 4 mM V^{2+} was sufficient to inhibit the HER. In contrast, with 5 mM V^{3+} and 5 mM VO^{2+}, the HER was not impaired. We conclude that V^{2+} inhibits hydrogen evolution – at least more effectively than V^{3+} or VO^{2+}. Notably, the fact that more than 5/5 mM V^{3+}/VO^{2+} eventually inhibited the HER, too, does not imply an explicit VO^{2+}-contribution. Alternatively, enough V^{2+} may have formed upon V^{3+}-reduction.

3.4. Half-cell measurements – V^{2+} air-oxidized into V^{3+}

In the following, we illustrate that the HER is more sensitive to V^{2+} than V^{3+}. Simultaneously, we exclude the role of external contaminants, as we left the electrolyte itself untouched. We continued analyzing the electrolyte with 80/20 mM V^{2+}/V^{3+} in 2 M H_2SO_4.

Without rotation, we first recorded the purple *CV* in Fig. 4, staying at reductive potentials at -1.8 V $< E < -1.0$ V. Below -1.6 V, the *CV* remained flat, proving no HER. Subsequently, we exposed the electrolyte for 18 h to air, oxidizing all V^{2+} to V^{3+} by atmospheric oxygen. Afterward, the electrolyte color changed from purple to green, indicating all V^{2+} had turned into V^{3+}.

This time, in pure 0/100 mM V^{2+}/V^{3+}, we repeated the *CV*. Interestingly, the first scan (green line) revealed a distinctive cathodic current below -1.6 V, attributable to evolved hydrogen visibly on the surface. Notably, the HER current quickly faded during the subsequent scans (not shown), presumably resulting from V^{2+} accumulating on the surface.

We conclude that, besides the vanadium concentration, also its valency determines the HER activity. Consequently, rather than contaminants, vanadium itself, and specifically V^{2+}, inhibits the HER.

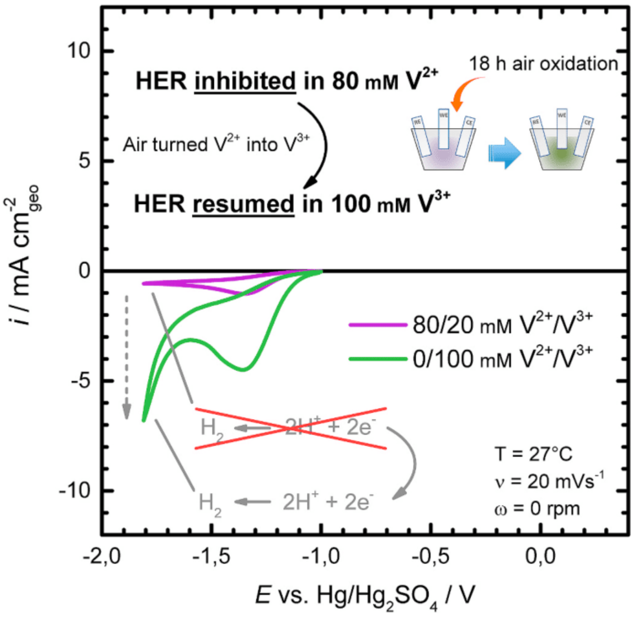

Fig. 4. Cyclic voltammograms of basal plane HOPG-RDE in 80/20 mM V^{2+}/V^{3+} (purple) and 0/100 V^{2+}/V^{3+} (green). Air-oxidation for 18 h converted all V^{2+} into V^{3+}. The electrode did not rotate, and the scan rate was 20 mV s^{-1}. An abundance of V^{2+} led to HER inhibition. In contrast, in V^{3+}, hydrogen evolution was significant. (For interpretation of the references to color in this figure legend, the reader is referred to the Web version of this article.)

3.5. Half-cell measurements – recovering hydrogen evolution and V^{2+}/V^{3+}-activity at cathodic potentials in 2 M H_2SO_4

The following experiment shows that the respective activities for hydrogen evolution and the V^{2+}/V^{3+}-reaction are related. We moved the working electrode between two half-cells, one filled with 1.6 M V^{2+}/V^{3+} and one with vanadium-free 2 M H_2SO_4. We determined the V^{2+}/V^{3+}-activity via EIS before and after cycling in vanadium-free H_2SO_4. As step 1 in Fig. 5, we recorded a CV in 1.28/0.32 M V^{2+}/V^{3+}. After returning from -1.8 V to *OCP*, we recorded an EIS at *OCP*, revealing an R_{ct} of about 250 Ω cm^2 (step 2, inset). Afterward, we moved the electrode into 2 M H_2SO_4 and scanned five CVs between *OCP* and -1.8 V (step 3). Remarkably, with each cycle, the HER current increased gradually (at -1.8 V from -5 mA to -15 mA). As we moved the electrode back to 1.28/0.32 M V^{2+}/V^{3+}, the R_{ct} was now 140 Ω cm^2 (step 4, inset), corresponding to only 60% of the value at step 2 before cycling in H_2SO_4.

In conclusion, cathodic cycling in vanadium-free 2 M H_2SO_4 recovered the activity for both hydrogen evolution and the V^{2+}/V^{3+}-reaction. This correlation implicates both inhibition phenomenons interconnected and resulting from the same reason, being V^{2+} adsorbing to the surface and hindering both reactions.

Notably, the electrode activity recovered during cycling exclusively between -1.8 V $< E < -0.9$ V vs. Hg/Hg_2SO_4 (referring to -1.25 V $< E < -0.25$ V vs. NHE). At these reductive potentials, presumably, no oxides form on the carbon surface. Consequently, our observations contradict the explanatory approach that ascribes the activity hysteresis to oxide formation and destruction on the surface. If valid, after cycling at cathodic, oxides-reducing potentials, we would instead expect a further decrease in V^{2+}/V^{3+}-activity. However, we observed the opposite trend, excluding oxide formation as a cause for activity

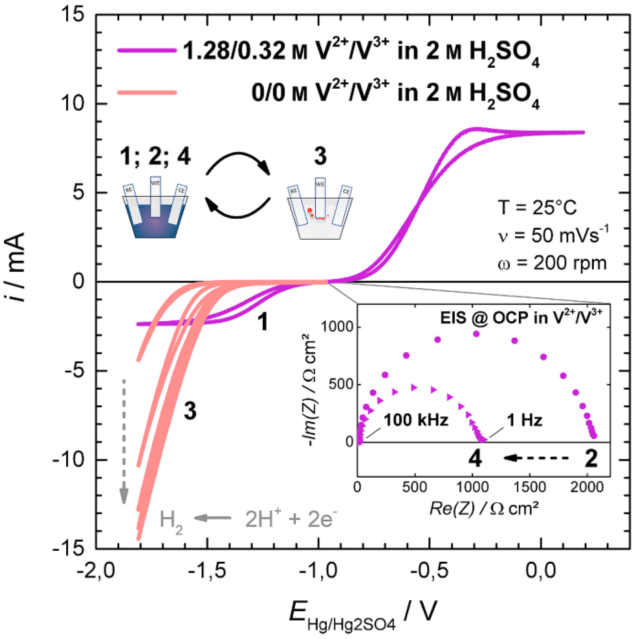

Fig. 5. A sequence of four half-cell measurements, moving the basal plane HOPG-RDE between two half-cells comprising 1.28/0.32 M V^{2+}/V^{3+} and vanadium-free 2 M H_2SO_4. Step 1: Cyclic voltammograms (CVs) between -1.8 V $< E < 0.2$ V at a scan rate of 50 mV s^{-1} in 1.28/0.32 M V^{2+}/V^{3+}; Step 2: EIS at OCP in 1.28/0.32 M V^{2+}/V^{3+}; Step 3: CVs between -1.8 V $< E < 0.2$ V at a scan rate of 50 mV s^{-1} in vanadium-free 2 M H_2SO_4, showing increasing hydrogen evolution activity; Step 4: EIS at OCP in 1.28/0.32 M V^{2+}/V^{3+}, showing increased V^{2+}/V^{3+}-activity. The CV scan rate was 50 mV s^{-1}, and the rotation rate was 200 rpm.

regeneration.

The activity recovery explains instead with oxidative desorption of adsorbed V^{2+}. When moved into vanadium-free H_2SO_4, the Nernstian V^{2+}/V^{3+}-equilibrium potential is shifted divergently negatively due to the absence of any V^{3+}, according to

$$E_{Nernst}\left(V^{2+}/V^{3+}\right) = E^0 + \frac{RT}{F} ln\frac{c\left(V^{3+}\right)}{c\left(V^{2+}\right)}. \tag{4}$$

Consequently, even at cathodic potentials below −0.25 V vs. NHE, surface-bound V^{2+} will be oxidized, desorb and leave the surface. This short-term experiment does not exclude oxide destruction to add to long-term degradation. However, our results suggest that, in this case, activity recovery resulted from V(II)-oxidation rather than oxide formation.

3.6. V(II)-adsorption mechanism – V^{2+} inhibiting active surface sites

In this section, we illustrate a V^{2+}-adsorption mechanism inhibiting the surface for the hydrogen evolution and V^{2+}/V^{3+}-reaction. We first reproduced the inner-sphere mechanism for the V^{2+}/V^{3+}-reaction, as suggested by Sun et al. (Fig. 6) [30]. Here, a hydroxy group represents the active reaction site. Nevertheless, any other active group is compatible with the following considerations. For the V^{3+}-reduction to V^{2+}, first, V^{3+} diffuses from the solution toward the electrode surface. It substitutes the hydrogen in a hydroxy group, building C–O–V(III)$^{2+}$ (step 1 to 2). In step 2 to 3, the C–O–V(III)$^{2+}$ receives an electron and converts into C–O–V(II)$^{+}$. In step 3 to 4, the V(II) desorbs, liberating its site and diffusing back into the solution. We propose that V(II) energetically favors its adsorbed over its desorbed state until reaching an equilibrium on the surface, indicated by the shorter red arrow in Fig. 6a.

In Fig. 6b, we illustrate a V(II) equilibrium surface coverage establishing over time. On the left, initially, the surface comprises free active sites accessible for hydrogen and V^{2+} and V^{3+} ions. On the right, over time, V(II) will occupy active sites until reaching an equilibrium coverage, inhibiting the hydrogen evolution and V^{2+}/V^{3+}-reaction.

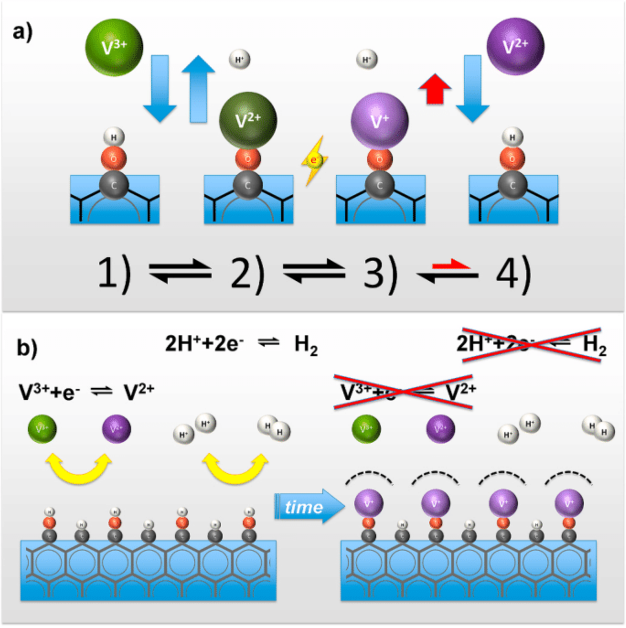

Fig. 6. Schematics illustrating the V^{2+}/V^{3+} and HER inhibition mechanism: a) V^{2+}/V^{3+} redox reaction mechanism proposed by Sun and Skyllas-Kazachos[23] involving surface hydroxides serving as adsorption site for the V^{3+} and V^{2+}. b) Graphite edge decorated with oxygen and hydrogen atoms (red and white spheres) catalytically active for the V^{2+}/V^{3+}- and hydrogen evolution reaction. The left-hand side shows the surface before and the right-hand side after accumulating an inhibiting V(II)-coverage, represented by C–O–V(II)$^{+}$. (For interpretation of the references to color in this figure legend, the reader is referred to the Web version of this article.)

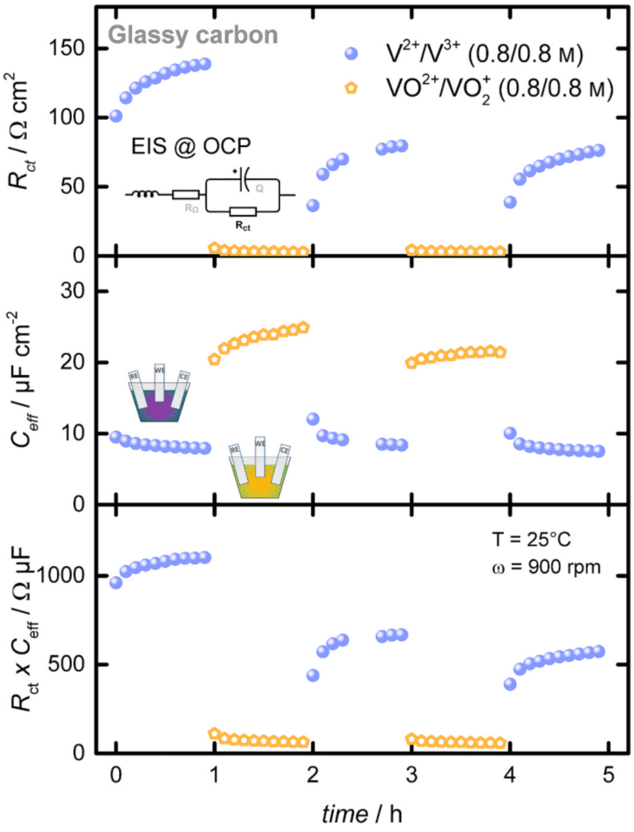

Fig. 7. Repetitive EIS at OCP recorded with a GC-RDE in either 1.6 M V^{2+}/V^{3+} (0.8 M/0.8 M) or 1.6 M VO^{2+}/VO_2^{+} (0.8 M/0.8 M). Electrolyte temperature was 25 °C, and the rotation rate was 900 rpm. After each hour, the electrode moved from either V^{2+}/V^{3+} (purple) to VO^{2+}/VO_2^{+} (yellow) or vice versa. The upper diagram plots R_{ct} over idle operation time, derived from fitting the EIS data to the displayed equivalent Randles circuit. The middle diagram shows the double-layer capacitance (C_{dl}) derived according to Eq. (6). The lower diagram presents the R_{ct} normalized to C_{dl}. Despite C_{dl} changes inversely to R_{ct}, they are not (in-)direct proportional to each other. Instead, C_{dl} and R_{ct} are inversely correlated. Possibly, V^{2+} adsorbs to active sites of the A_{ECSA}, inhibiting their contribution to C_{dl}. Additionally, adsorbed V^{2+} may increase the double-layer thickness t_{dl}, also decreasing C_{dl}. (For interpretation of the references to color in this figure legend, the reader is referred to the Web version of this article.)

The outlined V(II)-adsorption is plausible considering the similar surface complexation of related divalent 3d-transition metal (3d-TM) ions. Several studies demonstrated that Cu(II) [25,31], Zn(II) [32], Ni(II) [33], Co(II), and Cd(II) [25,34] adsorb on surface oxides due to surface complexation.

Jiang et al. validated computationally that V^{2+} and V^{3+} adsorb on keto group (C═O), facilitating electron transfer on the graphite surface [35].Although they found V^{3+} to bind more tightly on carbon edge sites than V^{2+} (−45 kcal mol^{-1} vs. −30 kcal mol^{-1}), on bare and hydroxylated basal planes, V^{2+} is more stable. However, the adsorbed V(II) species may prove more complicated than the suggested C–O–V(II)$^{+}$. Transition metals have several available valence orbitals and tend to participate in multiple ligand bonds [36]. In specific, they commonly bind to organic groups with orbital similarity [37].

The V^{3+}/VO^{2+}-electrolyte contains phosphoric acid (30–50 mM) as a precipitation inhibitor for V(IV) and V(V) at elevated temperatures > 40 °C [6]. Consequently, phosphate ions qualify as ligand candidates participating in the surface complexation. For clarification, future studies may evaluate whether the phosphate concentration influences the observed surface inhibition.

Furthermore, according to literature reports, negative polarization in V^{2+}/V^{3+}-electrolyte causes surface reconstruction from sp^2-to sp^3-hybridized carbon and surface corrosion [1,2,5,12]. Further studies must assess whether the observed corrosion and sp^2-to sp^3-transition is related to V(II)-adsorption.

In summary, many different possible surface configurations may explain our observations. Unequivocal identification of the suspected adsorbed V^{2+}-species requires techniques of surface characterization. However, standard ex-situ techniques such as XPS require the samples to be thoroughly washed and dried. Due to contact with atmospheric oxygen during this process, an electrochemical potential in the range of 1.0 V would establish. Accounting for the sensitivity to the EC potential demonstrated in Figs. 1, 4 and 5, the adsorbed vanadium would presumably desorb. Consequently, XPS measurements would not provide direct insight into the adsorbed state during electrode operation. Instead, in-situ techniques are promising. Unwin et al. pioneered several techniques combining electrochemical and lateral surface probing at high spatial resolution. Scanning electrochemical cell microscopy (SECCM) allowed attesting different site-specific redox kinetics for step edges and the basal surface on HOPG. In the vanadium system, SECCM could provide information on whether the adsorption is site-specific [38,39]. In-situ atomic force microscopy (AFM) may allow resolving adsorbents spatially. Patel et al. could show that the redox kinetics of Fe $(CN)_6^{4-/3-}$ deteriorates due to the deposition of material on the HOPG electrode [40]. Another suitable in-situ technique for identifying newly formed surface bonds may be electrochemical Fourier-transform infrared (EC-FTIR) spectroscopy, exciting surface bond vibration modes. Simultaneously to a change in EC surface activity, the IR absorption spectra may indicate a change in adsorbent composition, however diverse the binding relations may be.

3.7. Half-cell measurements – recovering V^{2+}/V^{3+}-activity upon contacting VO^{2+}/VO_2^+-electrolyte

This section demonstrates the R_{ct} development on glassy carbon while resting in either V^{2+}/V^{3+} or VO^{2+}/VO_2^+-electrolyte (0.8 M/0.8 M). To demonstrate independence from the electrode preparation, we chose not to use plasma-treatment. Instead, we only polished the GC-RDE tip with a 50 μm Al_2O_3 polishing paste. We then cleaned the tip by ultrasonication for 5 min in MilliQ™ water. After mounting the electrode (without further plasma treatment) in the respective half-cells, we recorded repetitive *EIS* at *OCP* over 1 h. During this time, the electrode rotated at 900 rpm. The electrolyte temperatures were constant at 25 °C.

The upper diagram in Fig. 7 shows the R_{ct} derived by fitting the *EIS* data to the displayed Randles circuit. The V^{2+}/V^{3+}-R_{ct} increased steadily, while its rate of increase decelerated. Subsequently, we moved the electrode into a second half-cell filled with 1.6 M VO^{2+}/VO_2^+ (0.8 M/0.8 M). For another hour, the potential rested again at *OCP* during the repetitive *EIS*. Here, the VO^{2+}/VO_2^+-R_{ct} was smaller by a factor of 30–50, owing to the generally faster kinetics of the VO^{2+}/VO_2^+-reaction [34]. In the third hour, we moved the electrode back from the positive to the negative electrolyte. The V^{2+}/V^{3+}-R_{ct} started with only a third compared to when it left the V^{2+}/V^{3+}. However, before long, the newly improved kinetics showed similar degradation. After the third hour, we repeated to alternate the electrode to VO^{2+}/VO_2^+ and back to V^{2+}/V^{3+}, demonstrating the V^{2+}/V^{3+}-R_{ct} regeneration upon VO^{2+}/VO_2^+-contact being reproducible.

Of course, crucial for the electrode kinetics is the size of the electrochemically active surface area (A_{ECSA}). Therefore, a change in A_{ECSA} would have explained the course in R_{ct}. An indicator for the A_{ECSA} is the double-layer capacitance (C_{dl}) since it correlates with the absolute permittivity $\varepsilon = \varepsilon_r\varepsilon_0$, the thickness of the double layer t_{dl} and specifically with A_{ECSA} [22,41]:

$$C_{dl} = \varepsilon_r\varepsilon_0\frac{A_{ECSA}}{t_{dl}} \tag{5}$$

The capacitance determination referred to the Randles circuit comprising a constant phase element (*CPE*). Interpreting the *CPE* to represent a planar surface distribution of impedance time constants, we used R_Ω, R_{ct}, and the *CPE* parameters Q and a to calculate the effective capacitance via [42–44].

$$C_{dl} = Q^{1/a}\left(R_\Omega^{-1} + R_{ct}^{-1}\right)^{(1-a)/a} \tag{6}$$

The middle diagram in Fig. 7 shows the double-layer capacitance C_{dl} evolution. Indeed, C_{dl} in V^{2+}/V^{3+} decreases slightly from an initial 10 μF cm^{-2} to 8 μF cm^{-2}, concurrent with the observed increase in R_{ct}. In contrast, C_{dl} in VO^{2+}/VO_2^+ is 20 μF cm^{-2}, about twice as large as in V^{2+}/V^{3+}, and increases steadily by 20% over the measurement hour. Back in V^{2+}/V^{3+}, C_{dl} started at 12 μF cm^{-2}, about 50% more than at the time it left V^{2+}/V^{3+}. However, upon further V^{2+}/V^{3+}-exposure, it dropped again to 8 μF cm^{-2}, being the same value as after the first hour of V^{2+}/V^{3+}-contact. This C_{dl} behavior inverted to R_{ct} may indicate that the effective A_{ECSA} increased and decreased over time.

The lower diagram in Fig. 7 shows the R_{ct} normalized to C_{dl}. Despite C_{dl} changed inversely to R_{ct}, the C_{dl}-normalized R_{ct} was not constant. Instead, there is no (in-)direct proportionality but rather a correlation between R_{ct} and C_{dl}. Here, C_{dl} could have changed due to A_{ECSA}. However, de- or increase of A_{ECSA} in a physical sense was not reasonable since it would imply that the carbon surface was reorganizing itself reversibly. Rather probable is that A_{ECSA} lost or gained EC activity. V^{2+}-adsorption may have inhibited specific surface groups such as carbon edge sites, so they contributed less to the double-layer capacitance. When not inhibited, these surface groups may have been particularly active for the V^{2+}/V^{3+} reaction, explaining why the R_{ct} increase is disproportionate compared to the C_{dl} decrease.

According to Eq. (5), C_{dl} could have also decreased because of an increased t_{dl} and a decreased ε. Similar to surface groups no longer contributing to the capacitance, adsorbed V^{2+} may have increased t_{dl} due to its larger ionic radius. Simultaneously, the double-layer may have decreased in ε as a measure for its polarizability. Again, these considerations agree with the observed accompanying surface kinetics deactivation.

3.8. Full-cell measurements – performance recovery in symmetric- and regular-cells

The kinetics deactivation by surface inhibition is also relevant with VRFB full-cell electrodes. In light of the findings obtained, below we demonstrate strategies implied for mitigating the performance degradation.

VRFB full-cells equipped with graphite felt (GF) electrodes operated in the symmetric-cell arrangement illustrated in Fig. 8a. Accordingly, the electrodes were fed by the same electrolyte precharged to 50% SoC, being either 1.6 M V^{2+}/V^{3+} or 1.6 M VO^{2+}/VO_2^+. The electrolyte continuously circulated controlled at 4 ml min^{-1} cm^{-2} and 20 °C. A conditioning cell identical to the test cell described in Fig. SI 1 maintained a stable SoC of 50%, indicated by 1.410 ± 0.005 V *OCV*.

Fig. 8b illustrates the GF electrodes resting at *OCV*, defined as idle cell operation. After every 24 h, we alternated the electrolyte feed lines. Defined by the respective electrolyte, the electrode potentials changed from −0.26 V to 1.0 V vs. NHE or vice versa.

While contacting the respective vanadium electrolyte, repetitive EIS resolved the R_{ct}-evolution over the idle operation time (Fig. 8c). We analyzed the EIS Nyquist plots (Fig. SI 9) using the displayed equivalent circuit. The R_{ct} represents the sum of both half-cell R_{ct}. Evident from the R_{ct}-evolution over day 1, when the electrodes contacted V^{2+}/V^{3+}-electrolyte, R_{ct} continuously increased substantially from 0.8 Ω cm^2 to 2.5 Ω cm^2. In contrast, during day 2 in VO^{2+}/VO_2^+, R_{ct} is much smaller and

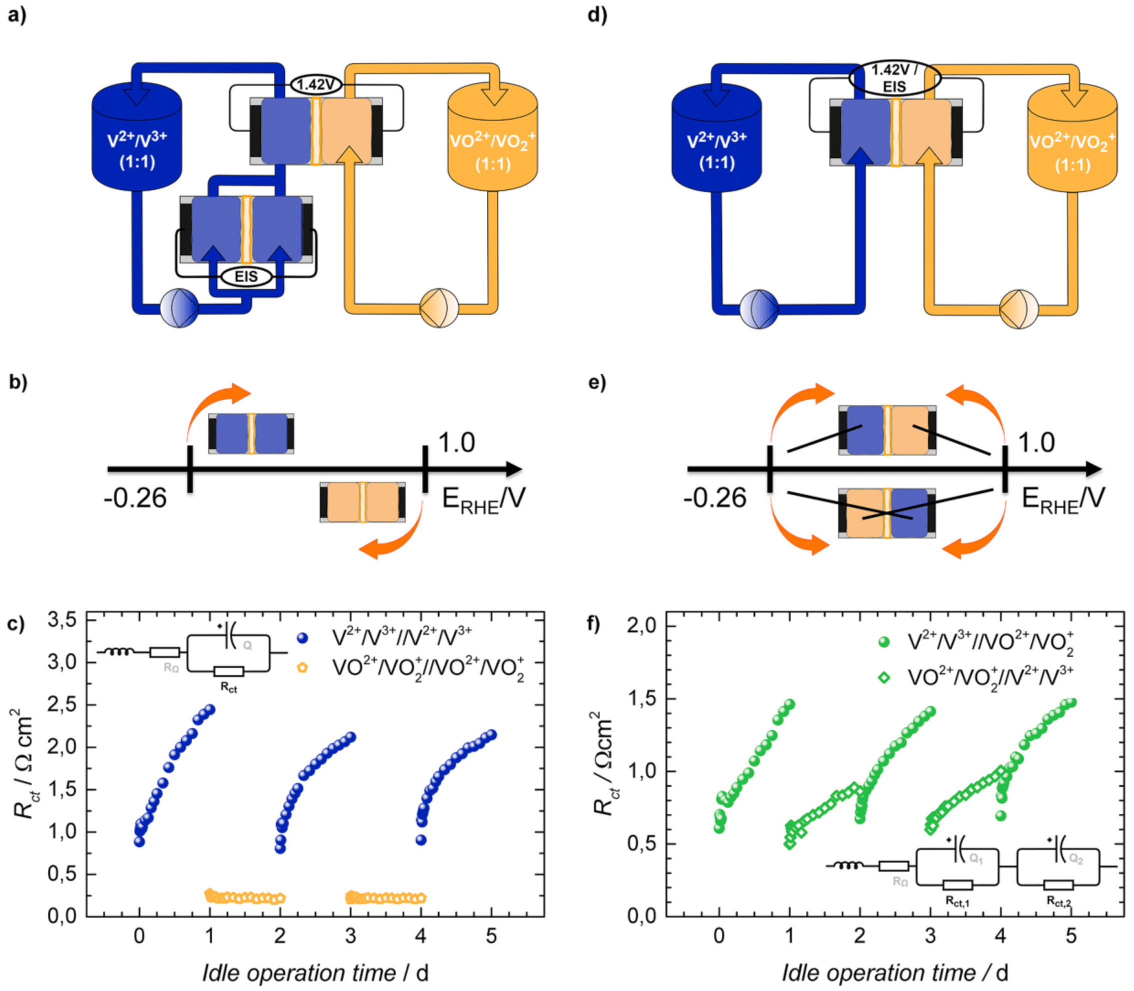

Fig. 8. Electrochemical impedance spectroscopy at OCV on a VRFB symmetric and regular full-cell assembly, working on 1.6 M vanadium electrolyte, precharged to 50% SoC, temperature-controlled to 20 °C, and at a flow rate of 4 ml min^{-1} cm^{-2}. After each 24 h, the electrolyte feed switched from either 1.6 M V^{2+}/V^{3+} (blue) to 1.6 M VO^{2+}/VO_2^+ (yellow) or vice versa. a) Symmetric-cell assembly in series with the conditioning cell maintaining constant SoC; b) Schematics of the negative and positive EC electrode potentials in the symmetric-cell; c) R_{ct} over idle operation time, derived from fitting the EIS data with the displayed equivalent circuit. d) Regular full-cell assembly; e) Schematics of the negative and positive electrode potentials with regular (top) and interchanged (bottom) electrolyte flow; f) R_{ct} over idle operation time; values derived by fitting EIS data with the displayed equivalent circuit. (For interpretation of the references to color in this figure legend, the reader is referred to the Web version of this article.)

stays constant at around 0.2 Ω cm^2. The results quantitatively agree with Schneider et al. who found similar R_{ct} for the two reactions [45].

Remarkably, on day 3, the V^{2+}/V^{3+}-activity had entirely recovered. As on day 1, R_{ct} started again at the initial value of 0.8 Ω cm^2 and showed an increasing R_{ct}. Further repetition of electrolyte alteration on day 4 in VO^{2+}/VO_2^+ and day 5 in V^{2+}/V^{3+} revealed that R_{ct} characteristics were highly reproducible. There are striking parallels to the half-cell electrode behavior described in Figs. 1 and 7. There, scanning the electrode potential from an *OCP* -0.26 V_{NHE} cathodically or simple resting at *OCP* caused the activity to deteriorate. In this case, resting the GF potential at *OCP* -0.26 V_{NHE} resulted in an increased R_{ct}. Correspondingly, resting at 1.0 V_{NHE} in the positive electrolyte imitated an anodic scan and caused the GF activity to recover.

Finally, we also alternated the electrolyte in VRFB full-cells in the regular-cell arrangement, this time fed in parallel with 1.6 M V^{2+}/V^{3+} and 1.6 M VO^{2+}/VO_2^+ (Fig. 8d). As with the symmetric-cells, we interchanged the electrolyte feed lines after 24 h, reversing the anode and cathode polarity, as sketched in Fig. 8e.

Considering the R_{ct} over idle operation time in Fig. 8f, each feed configuration revealed similar behavior. As expected from the previous symmetric-cell results, the R_{ct} increased steadily over time, reflecting the degradation in V^{2+}/V^{3+}-activity. When interchanging the electrolyte feed after each day, R_{ct} was reset and started growing from the same starting level of the day before. This behavior matches observations by Miller et al. where an electrolyte interchange resulted in resetting cell overpotentials [11].

In Fig. 8c and f, another striking feature of the R_{ct}-increase unfolds, i. e., its rate of increase decelerates, as was already observable for the half-cell experiment in Fig. 7. While the commonly observed slowing growth rate so far remained unexplained [1,2,4], it is coherent with the proposed image of growing V(II) surface coverage. A growing surface coverage translates to a vanishing of reaction sites. The consequent decrease in site number may correspond to an exponential decay of EC active surface area A_{ECSA} in the form of

$$A_{ECSA} = A_{ECSA,0}\left((1-\theta)+\theta\cdot e^{-k\cdot t}\right) \tag{7}$$

According to Eq. (7), the initial surface area $A_{ECSA,0}$ decays until reaching a constant equilibrium level $A_{ECSA,0}(1-\theta)$. Here, θ is the relative surface coverage, t the idle operation time, and k the decay constant.

Furthermore, R_{ct} is inversely proportional to the surface area according to

$$R_{ct} \propto (A_{ECSA})^{-1}. \tag{8}$$

Substituting Eq. (7) into Eq. (8), indeed, first-principle fitting verified the function coincides with the growing R_{ct}. However, it required more terms with additional decay constants. When assuming two or more terms, the fit gained significant accuracy, indicating several adsorption processes coincide. Although beyond the scope of this study, in general, the temporal evolution of full-cell kinetics also reflects an adsorption mechanism.

All in all, we tested the proposed inhibition mechanism in VRFB full-cells. The inhibition mechanism can explain why exposing a degraded anode to cathodic electrolyte restores the VRFB performance. Indeed, for practical battery management, interchanging the electrolyte feed may be technically extensive. A more feasible approach may be periodically reversing the electric electrode polarity. During the defined operation periods, the adsorption of V(II) still progresses. However, with desorption strategies regularly restoring the initial battery performance, the overall battery performance will increase significantly.

4. Conclusions

This study explains the anode degradation of vanadium redox flow batteries by relating V^{2+} with inhibiting the hydrogen evolution and the V^{2+}/V^{3+}-reaction. We examined highly-oriented pyrolytic graphite (HOPG) in basal and edge orientation and glassy carbon (GC) as rotating disk electrodes (RDE) in half-cells containing V(II), V(III), and V(IV) electrolytes. We then projected our findings onto the reversible kinetics of symmetric and regular VRFB full-cells. Our results suggest that the VRFB long-term performance degradation is due to anode surface inhibition by V(II)-adsorption. Simultaneously, the inhibiting V(II)-adsorption explains several features of electrode behavior that earlier appeared inconsistent but now provide a coherent picture.

V(II)-adsorption inhibits the hydrogen evolution reaction (HER). At cathodic potentials, V(II) covers and deactivates reaction sites for the H^+-reduction to H_2. Analogously, the adsorbed V(II) deteriorates the V^{2+}/V^{3+}-activity. In contrast, at anodic potentials, the V^{2+}/V^{3+}- and HER-activity regenerated reversibly – in vanadium-free sulfuric acid even at potentials below -0.26 V vs. NHE. While the Nernst shift facilitated V(II)-oxidation, explaining the regeneration, the negative potentials contradict oxide formation as an alternative reason for electrode activation. The picture of a surface coverage formation also explains the slow degradation of anode kinetics in VRFB full-cells. Moreover, the fact that the degradation rate decelerates is plausible as the adsorption rate decreases while striving towards equilibrium coverage.

The newly gained understanding of the anode degradation allows directing future electrode research and development towards manipulating the V(II)-adsorption. Directly assessing the surface using in-situ SECCM, AFM, or EC-FTIR-spectroscopy may identify specific surface configurations preferred for selective adsorption. A respective surface optimization may mitigate long-term degradation. Apart from surface properties, electrolyte additives – particularly the role of phosphoric acid – should be subject to a systematic examination. Further development of advanced operating strategies must optimize the cycle time of reversing the electrode polarity and automate its technical implementation.

In general, our findings explain why reversing the electrode polarity will reset the deteriorated kinetics and restore the degraded performance to initial levels. Such regenerating operating strategies can ensure reversibly high VRFB performance over the complete battery lifetime. Thus, VRFBs may ultimately be widely accepted, providing economic and sustainable energy storage.

CRediT authorship contribution statement

Tobias Greese: Conceptualization, Methodology, Investigation, Validation, Formal Analysisanalysis, Visualization, Writing – Original original Draftdraft. **Gudrun Reichenauer:** Writing – review & editing-Review Editing.

Declaration of competing interest

The authors declare that they have no known competing financial interests or personal relationships that could have appeared to influence the work reported in this paper.

Acknowledgments

Funding through the project ZAE-ST (storage technologies) the Bavarian Ministry of Economic Affairs and Media, Energy and Technology is highly acknowledged. The authors thank Prof. Hubert A. Gasteiger for valuable discussions.

Appendix A. Supplementary data

Supplementary data to this article can be found online at https://doi.org/10.1016/j.jpowsour.2021.229958.

References

[1] P. Mazúr, J. Mrlik, J. Pocedic, J. Vrána, J. Dundálek, J. Kosek, T. Bystron, Effect of graphite felt properties on the long-term durability of negative electrode in vanadium redox flow battery, J. Power Sources 414 (2019) 354–365.

[2] I. Derr, M. Bruns, J. Langner, A. Fetyan, J. Melke, C. Roth, Degradation of all-vanadium redox flow batteries (VRFB) investigated by electrochemical impedance and X-ray photoelectron spectroscopy: Part 2 electrochemical degradation, J. Power Sources 325 (2016) 351–359.

[3] I. Derr, A. Fetyan, K. Schutjajew, C. Roth, Electrochemical analysis of the performance loss in all vanadium redox flow batteries using different cut-off voltages, Electrochim. Acta 224 (2017) 9–16.

[4] A.M. Pezeshki, R.L. Sacci, G.M. Veith, T.A. Zawodzinski, M.M. Mench, The cell-in-series method: a technique for accelerated electrode degradation in redox flow batteries, J. Electrochem. Soc. 163 (1) (2015) A5202.

[5] I. Derr, D. Przyrembel, J. Schweer, A. Fetyan, J. Langner, J. Melke, C. Roth, Electroless chemical aging of carbon felt electrodes for the all-vanadium redox flow battery (VRFB) investigated by Electrochemical Impedance and X-ray Photoelectron Spectroscopy, Electrochim. Acta 246 (2017) 783–793.

[6] L. Cao, M. Skyllas-Kazacos, C. Menictas, J. Noack, A review of electrolyte additives and impurities in vanadium redox flow batteries, Journal of energy chemistry 27 (5) (2018) 1269–1291.

[7] A. Bourke, M.A. Miller, R.P. Lynch, X. Gao, J. Landon, J.S. Wainright, D.N. Buckley, Electrode kinetics of vanadium flow batteries: contrasting responses of VII-VIII and VIV-VV to electrochemical pretreatment of carbon, J. Electrochem. Soc. 163 (1) (2015) A5097.

[8] D.N. Buckley, A. Bourke, R.P. Lynch, N. Quill, M.A. Miller, J.S. Wainright, R. F. Savinell, Influence of pretreatment on kinetics at carbon electrodes and consequences for flow battery performance, MRS Advances 2 (21–22) (2017) 1131–1142.

[9] P. Chen, M.A. Fryling, R.L. McCreery, Electron transfer kinetics at modified carbon electrode surfaces: the role of specific surface sites, Anal. Chem. 67 (18) (1995) 3115–3122.

[10] J. Langner, M. Bruns, D. Dixon, A. Nefedov, C. Wöll, F. Scheiba, J. Melke, Surface properties and graphitization of polyacrylonitrile based fiber electrodes affecting the negative half-cell reaction in vanadium redox flow batteries, J. Power Sources 321 (2016) 210–218.

[11] M.A. Miller, A. Bourke, N. Quill, J.S. Wainright, R.P. Lynch, D.N. Buckley, R. F. Savinell, Kinetic study of electrochemical treatment of carbon fiber microelectrodes leading to in situ enhancement of vanadium flow battery efficiency, J. Electrochem. Soc. 163 (9) (2016) A2095.

[12] F. Chen, J. Liu, H. Chen, C. Yan, Study on hydrogen evolution reaction at a graphite electrode in the all-vanadium redox flow battery, Int. J. Electrochem. Sci 7 (1) (2012) 3750–3764.

[13] O. Nibel, S.M. Taylor, A. Pătru, E. Fabbri, L. Gubler, T.J. Schmidt, Performance of different carbon electrode materials: insights into stability and degradation under real vanadium redox flow battery operating conditions, J. Electrochem. Soc. 164 (7) (2017) A1608.

[14] R. Schweiss, A. Pritzl, C. Meiser, Parasitic hydrogen evolution at different carbon fiber electrodes in vanadium redox flow batteries, J. Electrochem. Soc. 163 (9) (2016) A2089.

[15] R.M. Darling, M.L. Perry, Half-cell, steady-state flow-battery experiments, ECS Transactions 53 (7) (2013) 31.

[16] D. Dixon, D.J. Babu, J. Langner, M. Bruns, L. Pfaffmann, A. Bhaskar, H. Ehrenberg, Effect of oxygen plasma treatment on the electrochemical performance of the rayon and polyacrylonitrile based carbon felt for the vanadium redox flow battery application, J. Power Sources 332 (2016) 240–248.

[17] C.E. Banks, T.J. Davies, G.G. Wildgoose, R.G. Compton, Electrocatalysis at graphite and carbon nanotube modified electrodes: edge-plane sites and tube ends are the reactive sites, Chem. Commun. (7) (2005) 829–841.

[18] P. Mazúr, J. Mrlík, J. Beneš, J. Pocedič, J. Vrána, J. Dundálek, J. Kosek, Performance evaluation of thermally treated graphite felt electrodes for vanadium redox flow battery and their four-point single cell characterization, J. Power Sources 380 (2018) 105–114.

[19] N. Bevilacqua, L. Eifert, R. Banerjee, K. Köble, T. Faragó, M. Zuber, R. Zeis, Visualization of electrolyte flow in vanadium redox flow batteries using synchrotron X-ray radiography and tomography–Impact of electrolyte species and electrode compression, J. Power Sources 439 (2019) 227071.

[20] H. Fink, Untersuchung von Verlustmechanismen in Vanadiumflussbatterien, Ph.D. thesis, Technische Universität München, 2019.

[21] M. Uhlemann, A. Krause, J.P. Chopart, A. Gebert, Electrochemical deposition of Co under the influence of high magnetic fields, J. Electrochem. Soc. 152 (12) (2005) C817.

[22] Allen J. Bard, Larry R. Faulkner, Electrochemical Methods: Fundamentals and Applications, 2 ed., Wiley, 2000, ISBN 0-471-04372-9.

[23] C.H. Hamann, A. Hamnett, W. Vielstich, Electrochemistry, 2 ed., 2007, ISBN 978-3-527-31069-2.

[24] P.R. Unwin, A.G. Güell, G. Zhang, Nanoscale electrochemistry of sp2 carbon materials: from graphite and graphene to carbon nanotubes, Accounts Chem. Res. 49 (9) (2016) 2041–2048.

[25] N. Pour, D.G. Kwabi, T. Carney, R.M. Darling, M.L. Perry, Y. Shao-Horn, Influence of edge-and basal-plane sites on the vanadium redox kinetics for flow batteries, J. Phys. Chem. C 119 (10) (2015) 5311–5318.

[26] K.K. Cline, M.T. McDermott, R.L. McCreery, Anomalously slow electron transfer at ordered graphite electrodes: influence of electronic factors and reactive sites, J. Phys. Chem. 98 (20) (1994) 5314–5319.

[27] P.J.F. Harris, Fullerene-related structure of commercial glassy carbons, Phil. Mag. 84 (29) (2004) 3159–3167.

[28] P.J. Rheinländer, P. Peitl, M. Bernt, H.A. Gasteiger, June). H2-Transport limitations in the hydrogen electrode in PEM water electrolysis, in: The Electrochemical Society-Meeting Abstracts, 2017, 1513-1513.

[29] M. Bernt, H.A. Gasteiger, Influence of ionomer content in IrO2/TiO2 electrodes on PEM water electrolyzer performance, J. Electrochem. Soc. 163 (11) (2016) F3179.

[30] B. Sun, M. Skyllas-Kazacos, Chemical modification of graphite electrode materials for vanadium redox flow battery application—part II. Acid treatments, Electrochim. Acta 37 (13) (1992) 2459–2465.

[31] S.T. Yang, Y. Chang, H. Wang, G. Liu, S. Chen, Y. Wang, A. Cao, Folding/aggregation of graphene oxide and its application in Cu2+ removal, J. Colloid Interface Sci. 351 (1) (2010) 122–127.

[32] R. Sitko, E. Turek, B. Zawisza, E. Malicka, E. Talik, J. Heimann, R. Wrzalik, Adsorption of divalent metal ions from aqueous solutions using graphene oxide, Dalton Trans. 42 (16) (2013) 5682–5689.

[33] C. Chen, X. Wang, Adsorption of Ni (II) from aqueous solution using oxidized multiwall carbon nanotubes, Ind. Eng. Chem. Res. 45 (26) (2006) 9144–9149.

[34] G. Zhao, J. Li, X. Ren, C. Chen, X. Wang, Few-layered graphene oxide nanosheets as superior sorbents for heavy metal ion pollution management, Environ. Sci. Technol. 45 (24) (2011) 10454–10462.

[35] Z. Jiang, K. Klyukin, V. Alexandrov, First-principles study of adsorption–desorption kinetics of aqueous V 2+/V 3+ redox species on graphite in a vanadium redox flow battery, Phys. Chem. Chem. Phys. 19 (23) (2017) 14897–14901.

[36] C. Elschenbroich, Energie, Polarität und Reaktivität der M-C-Bindung, in: Organometallchemie. Teubner Studienbücher Chemie, Vieweg+Teubner Verlag, Wiesbaden, 2003, https://doi.org/10.1007/978-3-322-99393-9_3.

[37] R. Hoffmann, Building bridges between inorganic and organic chemistry (Nobel Lecture), Angew Chem. Int. Ed. Engl. 21 (10) (1982) 711–724.

[38] A.G. Güell, A.S. Cuharuc, Y.R. Kim, G. Zhang, S.Y. Tan, N. Ebejer, P.R. Unwin, Redox-dependent spatially resolved electrochemistry at graphene and graphite step edges, ACS Nano 9 (4) (2015) 3558–3571.

[39] S.C. Lai, A.N. Patel, K. McKelvey, P.R. Unwin, Definitive evidence for fast electron transfer at pristine basal plane graphite from high-resolution electrochemical imaging, Angew. Chem. 124 (22) (2012) 5501–5504.

[40] A.N. Patel, M.G. Collignon, M.A. O'Connell, W.O. Hung, K. McKelvey, J. V. Macpherson, P.R. Unwin, A new view of electrochemistry at highly oriented pyrolytic graphite, J. Am. Chem. Soc. 134 (49) (2012) 20117–20130.

[41] H. Fink, J. Friedl, U. Stimming, Composition of the electrode determines which half-cell's rate constant is higher in a vanadium flow battery, J. Phys. Chem. C 120 (29) (2016) 15893–15901.

[42] B. Hirschorn, M.E. Orazem, B. Tribollet, V. Vivier, I. Frateur, M. Musiani, Determination of effective capacitance and film thickness from constant-phase-element parameters, Electrochim. Acta 55 (21) (2010) 6218–6227.

[43] P. Córdoba-Torres, T.J. Mesquita, O. Devos, B. Tribollet, V. Roche, R.P. Nogueira, On the intrinsic coupling between constant-phase element parameters α and Q in electrochemical impedance spectroscopy, Electrochim. Acta 72 (2012) 172–178.

[44] G.J. Brug, A.L. van den Eeden, M. Sluyters-Rehbach, J.H. Sluyters, The analysis of electrode impedances complicated by the presence of a constant phase element, J. Electroanal. Chem. Interfacial Electrochem. 176 (1–2) (1984) 275–295.

[45] J. Schneider, T. Tichter, P. Khadke, R. Zeis, C. Roth, Deconvolution of electrochemical impedance data for the monitoring of electrode degradation in VRFB, Electrochim. Acta 336 (2020) 135510.

GlossaryList of symbols

E: potential/V
I: current/mA
c: concentration/mol
i_{lim}: diffusion-limited current/mA
ω: rotation rate/rotations min^{-1}
ν: scan rate/mV s^{-1}
R: total resistance/Ω
R_{ct}: charge-transfer resistance/Ω cm^2
T: electrolyte temperature/°C
A_{ECSA}: electrochemically active surface area/cm^2
Θ: surface coverage/
k: decay constant/s^{-1}
t: idle operation time/dList of acronyms
AFM: atomic force microscopy
CV: cyclic voltammetry
EC-FTIR: electrochemical Fourier-transform infrared spectroscopy
EIS: electrochemical impedance spectroscopy
GC: glassy carbon
HER: hydrogen evolution reaction
Hg/Hg$_2$SO$_4$: mercury/mercurous sulfate
HOPG: highly-oriented pyrolytic graphite
NHE: normal hydrogen electrode
RDE: rotating disk electrodes
SECCM: scanning electrochemical cell microscopy
SoC: state-of-charge
OCP: open-circuit-potential
OCV: open-circuit-voltage
VRFB: vanadium redox flow batteries
XPS: x-ray photoemission spectroscopy

]

5. Conclusion

This work aimed at better understanding the graphite electrode performance in vanadium redox flow batteries (VRFB). The first part focused on the effects of thermal treatment, changing several electrode properties simultaneously. As a result, the effectiveness of the treatment was confirmed. However, the underlying working principles were different than expected based on the literature and had to be re-defined. The second part presented a new approach to explaining a commonly observed but unresolved phenomenon of performance degradation. A battery testing environment was developed to demonstrate the findings mentioned above, enabling highly stable system parameters and, hence, reproducible performance monitoring for extended battery operation times.

The first study investigated graphite felt (GF) electrodes after submitting them to a plasma treatment followed by thermal treatment in air at 400°C for different treatment times. The resulting electrode surface was examined by *SEM*, krypton adsorption analysis, and *XPS*. Also, their electrochemical performance was measured in a vanadium redox flow battery (VRFB) single cell during 20 h of idle cell operation. The plasma treatment ensured complete wettability by introducing oxygen surface functionalities. According to *SEM* and krypton adsorption measurements, the successive thermal treatment corroded the electrode surface, increasing the surface roughness and total surface area (*TSA*). However, against expectation, the surface corrosion decreased the oxygen surface functionalities, as indicated by *XPS*. The electrochemical performance did not correlate with the oxygen surface content, which contradicts reports in the literature that claim a significant catalytic activity by oxygen functionalities. Instead, the performance increase corresponded with the surface roughness and *TSA*. Since the *TSA* did not proportionally scale with the enhanced kinetics, a rather indirect correlation is suggested. When increasing the *TSA*, the carbon surface corrosion presumably created both inactive carbon basal-plane sites and active edge-plane sites, the latter of which catalyzing the V^{2+}/V^{3+}-reaction.

Additionally, commercial electrodes with considerable *TSA* were analyzed for their long-term performance during 400 h of cell operation at idle conditions. As a result, high surface roughness and area suppressed the commonly observed performance degradation over time. Moreover, the degradation rate decelerated over time.

The second publication presented a generally new concept, explaining the poorly understood performance degradation in VRFB graphite electrodes. According to this, V(II) is proposed to adsorb on the electrode surface and inhibit the V^{2+}/V^{3+}-reaction. The strength of this new interpretation is that it combines several, in part, unresolved features of the electrochemical behavior of the VRFB anode. Moreover, these features were confirmed with different graphite electrode materials, indicating that the observations are a general physical phenomenon. Materials tested in three-electrode half-cells were glassy carbon (GC) and highly-oriented pyrolytic graphite (HOPG) in the basal- and edge-plane orientation as rotating disk electrodes. The material tested in full cells was graphite felt, which is a standard electrode material in VRFBs.

In half-cell tests, already small concentrations of V^{2+}, V^{3+}, and VO^{2+} added to pure sulfuric acid electrolyte led to the inhibition of the previously pronounced hydrogen evolution reaction (*HER*). The effect was especially sensitive for the V^{2+}-concentration, pointing at its central role for the surface inhibition. Simultaneously to *HER*-inhibition, also the kinetics for the V^{2+}/V^{3+}-reaction decreased. Furthermore, when cycling to or resting at anodic potentials of 0.8-1.0 V vs. RHE in 2 M aqueous sulfuric acid containing 1.6 M vanadium, the V^{2+}/V^{3+}-activity regenerated reversibly. In vanadium-free sulfuric acid, the regeneration already took place at -0.26 V vs. RHE. Both observations can be explained by the oxidation of adsorbed V(II) and its release from the surface, in the vanadium-free case being facilitated by the Nernst shift of the oxidation potential in the cathodic direction. The cathodic potentials excluded oxide formation as an alternative reason for the observed regeneration.

The regeneration concept was transferred to full cells. In symmetric and regular cells, bringing the anodes in contact with the catholyte at resting potentials around 1.0 V vs. RHE also reversibly regenerated the anode kinetics. In addition, the steady anode kinetics degradation in full cells during extended operation times agrees well with the idea of continuous adsorption. The decelerating degradation rate reflects an adsorption rate that decelerates upon the slow formation of an equilibrium coverage. The newly gained understanding implies operation strategies that mitigate the VRFB kinetics degradation: Regularly reversing the electrode potentials will increase the average electrode kinetics and ensure stable performance during long-term battery operation.

In summary, the findings on the performance of graphite electrodes in VRFB have shown that the thermal electrode treatment and its effectiveness are attributable to different causes than those that are commonly suggested in the literature. Specifically, no oxide functionalities but carbon edge-sites were found to be responsible for enhancing the electrode performance. Thus, future research and development may be redirected towards more effective electrode treatment procedures, resulting in tailored graphite electrodes. Moreover, understanding the common effect of anode kinetics degradation and interpreting it to be due to the activity-inhibiting V(II)-adsorption opens up new paths for performance enhancement strategies. Finally, these enhancements may pave the way for a wide future adoption and implementation of the VRFB technology

Danksagungen

Ich danke Prof. Dr. Hubert A. Gasteiger für die Möglichkeit zur Promotion und das Korrekturlesen dieser Arbeit, Prof. Dr. Christina Roth für ihre Unterstützung meiner Promotion als Gutachterin, sowie den ZAE-Kollegen Susanne Wegertseder, Barbara Friese und Matthias Rzepka für die administrative Unterstützung meiner Arbeit am ZAE. Ich bin außerdem sehr dankbar für meine Zeit im ZAE-Palmenhain mit Max Möckl, Amadeus Teuffel, Petra Dotzauer und Friederike Kennett. Liebe Palmis Max, Amadeus, Petra und Friederike, vielen Dank für Eure Hilfe und Unterstützung und die Freundschaft die während dieser Arbeit entstanden ist. Ich danke Gudrun Reichenauer, dass sie sich durch das Korrekturlesen meiner Veröffentlichungen meinem Thema fachlich angenommen hat. Danke Gudrun für die Unterstützung und den professionellen Rat den Du mir zuteilwerden hast lassen. Vielen Dank Olivia Daisy für Deinen letzten englischen Schliff der Paper und vielen Dank auch Renate Hörwick für Dein fachliches Feedback! Vielen Dank Roman, Anna & Joschi Schneider, dafür, Euch meine Fachthemen immer wieder anzuhören - besonders an unseren Dienstagabenden – womit ihr mir viel Leichtigkeit ins Leben gebracht habt. Meiner ganzen Familie gilt großer Dank für ihre fachliche und seelische Unterstützung. Herzlich möchte ich mich bei der Zeller-Oma bedanken. Danke Oma für Deine guten Ratschläge, Deinen Zuspruch und natürlich Deine fantastisch gute Verpflegung, besonders Deine Suppe und die berühmten Heicharl, die einfach immer schmecken. Ich danke auch Gisela Grassl, der besten Schwiegermama die man sich wünschen kann sowie Gerhard Zeller der mir so oft ein wertvoller Mentor war. Ich danke Barbara und Werner Greese für ihre Begeisterung für mein Thema und ihren selbstlosen Einsatz und Ehrlichkeit, um meinen Schreibstil zu verbessern. Vielen Dank Werner und Barbara für Eure umfangreiche Unterstützung und Eure wertvollen Tipps! Vielen Dank an meine Mutter Erika Greese, meinen Vater Eugen Schmidt-Greese und meine Schwester Britta Binder und ihre Familie. Mama, Papa, Britta, Fabi, Ben und Miriam, danke für den Halt und die Ablenkung während unserer schönen Familienwochenenden! Ganz besonders danke ich meiner Mutter, die mich über die gesamte Zeit meiner Arbeit motiviert und bestärkt hat und mich während der Entstehung meiner Paper unermüdlich mit Verbesserungen meines Englisch unterstützt hat, und dabei tatsächlich nahezu jede Version der Paper gelesen hat. Vielen Dank Mama für Dein

jeder Zeit offenes Ohr, Dir meine Sorgen, meinen Ärger und meine Begeisterung anzuhören – du bist die Beste!

Das Letzte kommt zum Schluss: Ich möchte meiner Frau Susi Greese Danke sagen, die sich trotz starkem Widerwillen immer wieder meine totlangweiligen Arbeitsgeschichten anhört sowie meine schlechten Launen und mein andauerndes Geschimpfe erträgt. Danke Schatz, dass du mir auch in den dunkelsten Stunden immer die Sonnenseiten des Lebens zeigst und mir damit wieder die richtige Perspektive gibst. Mitunter hast Du mir unseren Sohn Luis geschenkt, der sich gleich in den ersten Wochen seines Lebens während meiner Schreibnächte zu mir auf die Couch gesellt und mir damit viel Freude und Kraft gegeben hat. Danke Knödel, ich freu‘ mich schon auf ein Leben mit viel Zeit mit Dir – von nun an ganz ohne Doktorarbeit!

Appendix. Publication List

Scientific Papers

Greese, T., Torres, P. A. L., Menga, D., Dotzauer, P., Wiener, M., & Reichenauer, G. (2021). Impact of Plasma and Thermal Treatment on the Long-term Performance of Vanadium Redox Flow Electrodes–Significance of Surface Structure vs. Oxygen Functionalities. *Journal of The Electrochemical Society*. 168(7), 070554.

Greese, T., & Reichenauer, G. (2021). Anode kinetics degradation in vanadium redox flow batteries–Reversible inhibition of the V^{2+}/V^{3+}-reaction due to V (II)-adsorption. *Journal of Power Sources*, 500, 229958.

Patent Applications

Greese, T., & Dotzauer, P. (2017). *Vorrichtung zum Schneiden von streifen- oder plattenförmigen Filzelementen* (DE 10 2017 203 160 B4). Deutsches Patent- und Markenamt.
https://depatisnet.dpma.de/DepatisNet/depatisnet?action=pdf&docid=DE102017203160B4
(accessed 11/04/2022).

Greese, T. (2018). *Elektrode für chemische Reaktoren, insbesondere für Redox-Flow-Batterien und Redox-Flow-Batterie mit einer solchen Elektrode* (DE 10 2018 222 728 A1). Deutsches Patent- und Markenamt.
https://depatisnet.dpma.de/DepatisNet/depatisnet?action=pdf&docid=DE102018222728A1
(accessed 11/04/2022).

Greese, T., & Rieth, T. (2018). *Monopolarplattenbauteil für chemische Reaktoren, insbesondere für Redox-Flow-Batterien, Verfahren zur Herstellung eines Monopolarplattenbauteils und Redox-Flow-Batterie mit einem solchen Monopolarplattenbauteil* (DE 10 2018 200 818 A1). Deutsches Patent- und Markenamt.
https://depatisnet.dpma.de/DepatisNet/depatisnet?action=pdf&docid=DE102018200818A1
(accessed 11/04/2022).

Conference Presentations

Greese, T., & Friedrich, F. (June 07th-09th 2016) *Synthesis and Validation of Carbon Model Surfaces for the Vanadium (IV/V) Redox Reaction* [Conference Poster]. 7th International Flow Battery Forum, Karlsruhe, Germany.

Greese, T., Schick, L., & Rieth, T. (July 27th-29th 2017) *Measurement Procedures and Test Conditions for Reproducible and Transparent Flow Battery Research* [Conference Poster]. 8th International Flow Battery Forum, Manchester, England.

Dotzauer, P., Greese, T., Hoffmann, L. & Jossen, A. (July 10th-12th 2018) *Electrolyte Characteristics of a Vanadium Flow Battery and Influence on Cell Performance* [Conference Poster]. 9th International Flow Battery Forum, Lausanne, Switzerland

Greese, T. (September 25th 2019) *Multi-Step Electrochemical Passivation Suggested for Degradation of* V^{2+}/V^{3+} *Charge-Transfer Reaction* [Conference Poster]. Flow Batterie Kolloquium, Karlsruhe, Germany.

Greese, T. (October 18th-19th 2021) *Anode kinetics degradation in VRFB explained due to a suggested adsorption of* V^{2+} [Conference Talk]. Prague Flow Battery Seminar, Prague, Czech Republic.

Bibliography

---

[1] Stern, N., & Stern, N. H. (2007). *The economics of climate change: the Stern review*. Cambridge University Press.

[2] Stocker, T. (2014). *Climate change 2013: the physical science basis: Working Group I contribution to the Fifth assessment report of the Intergovernmental Panel on Climate Change*. Cambridge University Press.

[3] Robinson, E., & Robbins, R. C. (1968). *Sources, abundance, and fate of gaseous atmospheric pollutants. Final report and supplement*. United States. (https://www.osti.gov/biblio/6852325, accessed 10/04/2022).

[4] Royer, D. L., Berner, R. A., & Park, J. (2007). Climate sensitivity constrained by CO_2 concentrations over the past 420 million years. *Nature*, 446(7135), 530-532.

[5] Hansen, J., Sato, M., Russell, G., & Kharecha, P. (2013). Climate sensitivity, sea level and atmospheric carbon dioxide. *Philosophical Transactions of the Royal Society A: Mathematical, Physical and Engineering Sciences*, 371(2001), 20120294.

[6] Edenhofer, O. (Ed.). (2015). *Climate change 2014: mitigation of climate change (Vol. 3)*. Cambridge University Press.

[7] Kaufmann, J., Kienscherf, P. A., & Ketter, W. (2020). Modeling and managing joint price and volumetric risk for volatile electricity portfolios. *Energies*, 13(14), 3578.

[8] Sterner, M. (2017). *Energiespeicher-Bedarf, Technologien, Integration*. Springer Berlin Heidelberg.

[9] Yang, Z., Zhang, J., Kintner-Meyer, M. C., Lu, X., Choi, D., Lemmon, J. P., & Liu, J. (2011). Electrochemical energy storage for green grid. *Chemical Reviews*, 111(5), 3577-3613.

[10] Chen, H., Cong, T. N., Yang, W., Tan, C., Li, Y., & Ding, Y. (2009). Progress in electrical energy storage system: A critical review. *Progress in Natural Science*, 19(3), 291-312.

[11] Sánchez-Díez, E., Ventosa, E., Guarnieri, M., Trovò, A., Flox, C., Marcilla, R., Soavi, F., Mazur, P., Aranzabe, E., & Ferret, R. (2021). Redox flow batteries: Status and perspective towards sustainable stationary energy storage. *Journal of Power Sources*, 481, 228804.

[12] Huang, Z., & Mu, A. (2021). Research and analysis of performance improvement of vanadium redox flow battery in microgrid: a technology review. *International Journal of Energy Research*, 45(10), 14170-14193.

[13] Dunn, B., Kamath, H., & Tarascon, J. M. (2011). Electrical energy storage for the grid: a battery of choices. *Science*, 334(6058), 928-935.

[14] Zhang, M., Moore, M., Watson, J. S., Zawodzinski, T. A., & Counce, R. M. (2012). Capital cost sensitivity analysis of an all-vanadium redox-flow battery. *Journal of The Electrochemical Society*, 159(8), A1183-A1188.

[15] Perry, M. L., & Weber, A. Z. (2015). Advanced redox-flow batteries: a perspective. *Journal of The Electrochemical Society*, 163(1), A5064-A5067.

---

[16] Ulaganathan, M., Aravindan, V., Yan, Q., Madhavi, S., Skyllas-Kazacos, M., & Lim, T. M. (2016). Recent advancements in all-vanadium redox flow batteries. *Advanced Materials Interfaces*, 3(1), 1500309.

[17] Pezeshki, A. M., Clement, J. T., Veith, G. M., Zawodzinski, T. A., & Mench, M. M. (2015). High performance electrodes in vanadium redox flow batteries through oxygen-enriched thermal activation. *Journal of Power Sources*, 294, 333-338.

[18] Aaron, D., Tang, Z., Papandrew, A. B., & Zawodzinski, T. A. (2011). Polarization curve analysis of all-vanadium redox flow batteries. *Journal of Applied Electrochemistry*, 41(10), 1175-1182.

[19] Rabbow, T. J., & Whitehead, A. H. (2017). Deconvolution of electrochemical double layer capacitance between fractions of active and total surface area of graphite felts. *Carbon*, 111, 782-788.

[20] Banks, C. E., Davies, T. J., Wildgoose, G. G., & Compton, R. G. (2005). Electrocatalysis at graphite and carbon nanotube modified electrodes: edge-plane sites and tube ends are the reactive sites. *Chemical Communications*, (7), 829-841.

[21] Pour, N., Kwabi, D. G., Carney, T., Darling, R. M., Perry, M. L., & Shao-Horn, Y. (2015). Influence of edge-and basal-plane sites on the vanadium redox kinetics for flow batteries. *The Journal of Physical Chemistry C*, 119(10), 5311-5318.

[22] Wei, G., Jing, M., Fan, X., Liu, J., & Yan, C. (2015). A new electrocatalyst and its application method for vanadium redox flow battery. *Journal of Power Sources*, 287, 81-86.

[23] Li, Y., Parrondo, J., Sankarasubramanian, S., & Ramani, V. (2019). Impact of surface carbonyl- and hydroxyl-group concentrations on electrode kinetics in an all-vanadium redox flow battery. *The Journal of Physical Chemistry C*, 123(11), 6370-6378.

[24] Dixon, D., Babu, D. J., Langner, J., Bruns, M., Pfaffmann, L., Bhaskar, A., Schneider, J. J., Scheiba, F., & Ehrenberg, H. (2016). Effect of oxygen plasma treatment on the electrochemical performance of the rayon and polyacrylonitrile based carbon felt for the vanadium redox flow battery application. *Journal of Power Sources*, 332, 240-248.

[25] Derr, I., Fetyan, A., Schutjajew, K., & Roth, C. (2017). Electrochemical analysis of the performance loss in all vanadium redox flow batteries using different cut-off voltages. *Electrochimica Acta*, 224, 9-16.

[26] Derr, I., Bruns, M., Langner, J., Fetyan, A., Melke, J., & Roth, C. (2016). Degradation of all-vanadium redox flow batteries (VRFB) investigated by electrochemical impedance and X-ray photoelectron spectroscopy: Part 2 electrochemical degradation. *Journal of Power Sources*, 325, 351-359.

[27] Derr, I., Przyrembel, D., Schweer, J., Fetyan, A., Langner, J., Melke, J., Weinelt, M., & Roth, C. (2017). Electroless chemical aging of carbon felt electrodes for the all-vanadium redox flow battery (VRFB) investigated by Electrochemical Impedance and X-ray Photoelectron Spectroscopy. *Electrochimica Acta*, 246, 783-793.

[28] Rampl, D. J. (2020). *Verlustmechanismen von Ionenaustauscher-Membranen in einer Redox-Flow-Batterie* (Bachelor’s thesis). Hochschule für Angewandte Wissenschaften München.

[29] Hamann, C. H. & Vielstich, W. (2005). *Elektrochemie.* Wiley-VCH-Verlag.

---

[30] Knopf, D. A., Luo, B. P., Krieger, U. K., & Koop, T. (2003). Thermodynamic dissociation constant of the bisulfate ion from Raman and ion interaction modeling studies of aqueous sulfuric acid at low temperatures. *The Journal of Physical Chemistry A*, 107(21), 4322-4332.

[31] Knehr, K. W., & Kumbur, E. C. (2011). Open circuit voltage of vanadium redox flow batteries: Discrepancy between models and experiments. *Electrochemistry Communications*, 13(4), 342-345.

[32] Fink, H. (2019). *Untersuchung von Verlustmechanismen in Vanadium-Flussbatterien* (Doctoral dissertation). Technische Universität München.

[33] Greese, T., & Reichenauer, G. (2021). Anode kinetics degradation in vanadium redox flow batteries–Reversible inhibition of the V^{2+}/V^{3+}-reaction due to V (II)-adsorption. *Journal of Power Sources*, 500, 229958.

[34] Bard, A. J., & Faulkner, L. R. (2001). *Fundamentals and applications. Electrochemical methods.* Wiley New York, 482, 580-632.

[35] Levich, V. G. (1962). *Physicochemical hydrodynamics.* Prentice-Hall Inc.

[36] Tang, A., Bao, J., & Skyllas-Kazacos, M. (2014). Studies on pressure losses and flow rate optimization in vanadium redox flow battery. *Journal of Power Sources*, 248, 154-162.

[37] Cao, L., Skyllas-Kazacos, M., Menictas, C., & Noack, J. (2018). A review of electrolyte additives and impurities in vanadium redox flow batteries. *Journal of Energy Chemistry*, 27(5), 1269-1291.

[38] Bhattarai, A., Whitehead, A. H., Schweiss, R., Scherer, G. G., Skyllas-Kazacos, M., Wai, N., Nguyen, T. D., Ghimire, P. C., Oo, M. O., & Hng, H. H. (2019). Anomalous behavior of anion exchange membrane during operation of a vanadium redox flow battery. *ACS Applied Energy Materials*, 2(3), 1712-1719.

[39] Roznyatovskaya, N. V., Fühl, M., Roznyatovsky, V. A., Noack, J., Fischer, P., Pinkwart, K., & Tübke, J. (2020). The Influence of Free Acid in Vanadium Redox-Flow Battery Electrolyte on "Power Drop" Effect and Thermally Induced Degradation. *Energy Technology*, 8(10), 2000445.

[40] Sun, S., Shao, Z., Yu, H., Li, G., & Yi, B. (2014). Investigations on degradation of the long-term proton exchange membrane water electrolysis stack. *Journal of Power Sources*, 267, 515-520.

[41] Thiam, B. G., & Vaudreuil, S. (2021). Recent Membranes for Vanadium Redox Flow Batteries. *Journal of The Electrochemical Society*, 168, 070553.

[42] Sun, C., Chen, J., Zhang, H., Han, X., & Luo, Q. (2010). Investigations on transfer of water and vanadium ions across Nafion membrane in an operating vanadium redox flow battery. *Journal of Power Sources*, 195(3), 890-897.

[43] Tang, A., Bao, J., & Skyllas-Kazacos, M. (2011). Dynamic modelling of the effects of ion diffusion and side reactions on the capacity loss for vanadium redox flow battery. *Journal of Power Sources*, 196(24), 10737-10747.

[44] Darling, R. M., Weber, A. Z., Tucker, M. C., & Perry, M. L. (2015). The influence of electric field on crossover in redox-flow batteries. *Journal of The Electrochemical Society*, 163(1), A5014-A5022.

---

[45] Agar, E., Knehr, K. W., Chen, D., Hickner, M. A., & Kumbur, E. C. (2013). Species transport mechanisms governing capacity loss in vanadium flow batteries: Comparing Nafion® and sulfonated Radel membranes. *Electrochimica Acta*, 98, 66-74.

[46] Knehr, K. W., & Kumbur, E. C. (2012). Role of convection and related effects on species crossover and capacity loss in vanadium redox flow batteries. *Electrochemistry Communications*, 23, 76-79.

[47] Fink, H., & Remy, M. (2015). Shunt currents in vanadium flow batteries: Measurement, modelling and implications for efficiency. *Journal of Power Sources*, 284, 547-553.

[48] Skyllas-Kazacos, M., McCann, J., Li, Y., Bao, J., & Tang, A. (2016). The mechanism and modelling of shunt current in the vanadium redox flow battery. *ChemistrySelect*, 1(10), 2249-2256.

[49] Kim, S., Thomsen, E., Xia, G., Nie, Z., Bao, J., Recknagle, K., Wang, W., Viswanathan, V., Luo, Q., Wei, X., Crawford, A., Coffey, G., Maupin, G., & Sprenkle, V. (2013). 1 kW/1 kWh advanced vanadium redox flow battery utilizing mixed acid electrolytes. *Journal of Power Sources*, 237, 300-309.

[50] Macauley, N., Papadias, D. D., Fairweather, J., Spernjak, D., Langlois, D., Ahluwalia, R., More, K. L., Mukundan, R., & Borup, R. L. (2018). Carbon corrosion in PEM fuel cells and the development of accelerated stress tests. *Journal of The Electrochemical Society*, 165(6), F3148-F3160.

[51] Pourbaix, M. (1966). *Atlas of chemical equilibria in aqueous solutions.* Pergamon Press.

[52] Haisch, T., Ji, H., Holtz, L., Struckmann, T., & Weidlich, C. (2021). Half-Cell State of Charge Monitoring for Determination of Crossover in VRFB—Considerations and Results Concerning Crossover Direction and Amount. *Membranes*, 11(4), 232.

[53] Poli, N., Schäffer, M., Trovò, A., Noack, J., Guarnieri, M., & Fischer, P. (2021). Novel electrolyte rebalancing method for vanadium redox flow batteries. *Chemical Engineering Journal*, 405, 126583.

[54] Nibel, O., Taylor, S. M., Pătru, A., Fabbri, E., Gubler, L., & Schmidt, T. J. (2017). Performance of different carbon electrode materials: insights into stability and degradation under real vanadium redox flow battery operating conditions. *Journal of The Electrochemical Society*, 164(7), A1608-A1615.

[55] Kim, K. J., Park, M. S., Kim, Y. J., Kim, J. H., Dou, S. X., & Skyllas-Kazacos, M. (2015). A technology review of electrodes and reaction mechanisms in vanadium redox flow batteries. *Journal of Materials Chemistry A*, 3(33), 16913-16933.

[56] Ni, X. Y., Liu, H., Wang, C., Wang, W. L., Xu, Z. B., Chen, Z., Wu, Y. H., & Hu, H. Y. (2020). Comparison of carbonized and graphitized carbon fiber electrodes under flow-through electrode system (FES) for high-efficiency bacterial inactivation. *Water Research*, 168, 115150.

[57] Greese, T., Torres, P. A. L., Menga, D., Dotzauer, P., Wiener, M., & Reichenauer, G. (2021). Impact of Plasma and Thermal Treatment on the Long-term Performance of Vanadium Redox Flow Electrodes–Significance of Surface Structure vs. Oxygen Functionalities. *Journal of The Electrochemical Society*. 168(7), 070554.

[58] Yue, L., Li, W., Sun, F., Zhao, L., & Xing, L. (2010). Highly hydroxylated carbon fibres as electrode materials of all-vanadium redox flow battery. *Carbon*, 48(11), 3079-3090.

---

[59] Sun, B., & Skyllas-Kazacos, M. (1992). Chemical modification of graphite electrode materials for vanadium redox flow battery application—part II. Acid treatments. *Electrochimica Acta*, 37(13), 2459-2465.

[60] Kabir, H., Gyan, I. O., & Cheng, I. F. (2017). Electrochemical modification of a pyrolytic graphite sheet for improved negative electrode performance in the vanadium redox flow battery. *Journal of Power Sources*, 342, 31-37.

[61] Liu, H., Yang, L., Xu, Q., & Yan, C. (2014). An electrochemically activated graphite electrode with excellent kinetics for electrode processes of V (II)/V (III) and V (IV)/V (V) couples in a vanadium redox flow battery. *RSC Advances*, 4(98), 55666-55670.

[62] Zhang, W., Xi, J., Li, Z., Zhou, H., Liu, L., Wu, Z., & Qiu, X. (2013). Electrochemical activation of graphite felt electrode for VO^{2+}/VO_2^+ redox couple application. *Electrochimica Acta*, 89, 429-435.

[63] Li, X. G., Huang, K. L., Liu, S. Q., Ning, T. A. N., & Chen, L. Q. (2007). Characteristics of graphite felt electrode electrochemically oxidized for vanadium redox battery application. *Transactions of Nonferrous Metals Society of China*, 17(1), 195-199.

[64] Estevez, L., Reed, D., Nie, Z., Schwarz, A. M., Nandasiri, M. I., Kizewski, J. P., Wang, W., Thomson, E., Liu, J., Zhang, J. G., Sprenkle, V., & Li, B. (2016). Tunable oxygen functional groups as electrocatalysts on graphite felt surfaces for all-vanadium flow batteries. *ChemSusChem*, 9(12), 1455-1461.

[65] Kim, K. J., Kim, Y. J., Kim, J. H., & Park, M. S. (2011). The effects of surface modification on carbon felt electrodes for use in vanadium redox flow batteries. *Materials Chemistry and Physics*, 131(1-2), 547-553.

[66] Ghimire, P. C., Schweiss, R., Scherer, G. G., Lim, T. M., Wai, N., Bhattarai, A., & Yan, Q. (2019). Optimization of thermal oxidation of electrodes for the performance enhancement in all-vanadium redox flow betteries. *Carbon*, 155, 176-185.

[67] Sun, B., & Skyllas-Kazacos, M. (1992). Modification of graphite electrode materials for vanadium redox flow battery application—I. Thermal treatment. *Electrochimica Acta*, 37(7), 1253-1260.

[68] Radinger, H., Ghamlouche, A., Ehrenberg, H., & Scheiba, F. (2021). Origin of the catalytic activity at graphite electrodes in vanadium flow batteries. *Journal of Materials Chemistry A*, 9(34), 18280-18293.

[69] Mazúr, P., Mrlík, J., Beneš, J., Pocedič, J., Vrána, J., Dundálek, J., & Kosek, J. (2018). Performance evaluation of thermally treated graphite felt electrodes for vanadium redox flow battery and their four-point single cell characterization. *Journal of Power Sources*, 380, 105-114.

[70] Schweiss, R., Meiser, C., & Goh, F. W. T. (2017). Steady-State Measurements of Vanadium Redox-Flow Batteries to Study Particular Influences of Carbon Felt Properties. *ChemElectroChem*, 4(8), 1969-1974.

[71] Langner, J., Bruns, M., Dixon, D., Nefedov, A., Wöll, C., Scheiba, F., Ehrenberg, H., Roth, C., & Melke, J. (2016). Surface properties and graphitization of polyacrylonitrile based fiber electrodes affecting the negative half-cell reaction in vanadium redox flow batteries. *Journal of Power Sources*, 321, 210-218.

---

[72] Mazúr, P., Mrlik, J., Pocedic, J., Vrána, J., Dundálek, J., Kosek, J., & Bystron, T. (2019). Effect of graphite felt properties on the long-term durability of negative electrode in vanadium redox flow battery. *Journal of Power Sources*, 414, 354-365.

[73] Pezeshki, A. M., Sacci, R. L., Veith, G. M., Zawodzinski, T. A., & Mench, M. M. (2015). The cell-in-series method: A technique for accelerated electrode degradation in redox flow batteries. *Journal of The Electrochemical Society*, 163(1), A5202-A5210.

[74] Bourke, A., Miller, M. A., Lynch, R. P., Gao, X., Landon, J., Wainright, J. S., Savinell, R.F., & Buckley, D. N. (2015). Electrode kinetics of vanadium flow batteries: contrasting responses of VII-VIII and VIV-VV to electrochemical pretreatment of carbon. *Journal of The Electrochemical Society*, 163(1), A5097-A5105.

[75] Buckley, D. N., Bourke, A., Lynch, R. P., Quill, N., Miller, M. A., Wainright, J. S., & Savinell, R. F. (2017). Influence of Pretreatment on Kinetics at Carbon Electrodes and Consequences for Flow Battery Performance. *MRS Advances*, 2(21-22), 1131-1142.

[76] Mazúr, P., Mrlik, J., Pocedic, J., Vrána, J., Dundálek, J., Kosek, J., & Bystron, T. (2019). Effect of graphite felt properties on the long-term durability of negative electrode in vanadium redox flow battery. *Journal of Power Sources*, 414, 354-365.

[77] Aaron, D. S., Liu, Q., Tang, Z., Grim, G. M., Papandrew, A. B., Turhan, A., Zawodzinski, T. A., & Mench, M. M. (2012). Dramatic performance gains in vanadium redox flow batteries through modified cell architecture. *Journal of Power Sources*, 206, 450-453.

[78] Park, S. K., Shim, J., Yang, J. H., Jin, C. S., Lee, B. S., Lee, Y. S., Shin, K. H., & Jeon, J. D. (2014). The influence of compressed carbon felt electrodes on the performance of a vanadium redox flow battery. *Electrochimica Acta*, 116, 447-452.

[79] Gerber, T., Fischer, P., Pinkwart, K., & Tübke, J. (2019). Segmented printed circuit board electrode for locally-resolved current density measurements in all-vanadium redox flow batteries. *Batteries*, 5(2), 38.

[80] Becker, M., Bredemeyer, N., Tenhumberg, N., & Turek, T. (2016). Polarization curve measurements combined with potential probe sensing for determining current density distribution in vanadium redox-flow batteries. *Journal of Power Sources*, 307, 826-833.

[81] Bhattarai, A., Wai, N., Schweiss, R., Whitehead, A., Scherer, G. G., Ghimire, P. C., Lim, T. M. & Hng, H. H. (2019). Vanadium redox flow battery with slotted porous electrodes and automatic rebalancing demonstrated on a 1 kW system level. *Applied Energy*, 236, 437-443.

[82] Greese, T. (2018). *Elektrode für chemische Reaktoren, insbesondere für Redox-Flow-Batterien und Redox-Flow-Batterie mit einer solchen Elektrode* (DE 10 2018 222 728 A1). Deutsches Patent- und Markenamt. https://depatisnet.dpma.de/DepatisNet/depatisnet?action=pdf&docid=DE102018222728A1 (accessed 11/04/2022).

[83] Greese, T., & Dotzauer, P. (2017). *Vorrichtung zum Schneiden von streifen- oder plattenförmigen Filzelementen* (DE 10 2017 203 160 B4). Deutsches Patent- und Markenamt. https://depatisnet.dpma.de/DepatisNet/depatisnet?action=pdf&docid=DE102017203160B4 (accessed 11/04/2022).

[84] Luo, T., Abdu, S., & Wessling, M. (2018). Selectivity of ion exchange membranes: A review. *Journal of Membrane Science*, 555, 429-454.

---

[85] Prifti, H., Parasuraman, A., Winardi, S., Lim, T. M., & Skyllas-Kazacos, M. (2012). Membranes for redox flow battery applications. *Membranes*, 2(2), 275-306.

[86] Cha, M. S., Jo, S. W., Han, S. H., Hong, S. H., So, S., Kim, T. H., Oh, S. G., Hong, Y. T., & Lee, J. Y. (2019). Ether-free polymeric anion exchange materials with extremely low vanadium ion permeability and outstanding cell performance for vanadium redox flow battery (VRFB) application. *Journal of Power Sources*, 413, 158-166.

[87] Liao, J. B., Lu, M. Z., Chu, Y. Q., & Wang, J. L. (2015). Ultra-low vanadium ion diffusion amphoteric ion-exchange membranes for all-vanadium redox flow batteries. *Journal of Power Sources*, 282, 241-247.

[88] Oldenburg, F. J., Nilsson, E., Schmidt, T. J., & Gubler, L. (2019). Tackling capacity fading in vanadium redox flow batteries with amphoteric PBI/Nafion bilayer membranes. *ChemSusChem*, 12(12), 2620-2627.

[89] Maurya, S., Shin, S. H., Lee, J. Y., Kim, Y., & Moon, S. H. (2016). Amphoteric nanoporous polybenzimidazole membrane with extremely low crossover for a vanadium redox flow battery. *RSC Advances*, 6(7), 5198-5204.

[90] Ling, L., Xiao, M., Han, D., Ren, S., Wang, S., & Meng, Y. (2019). Porous composite membrane of PVDF/Sulfonic silica with high ion selectivity for vanadium redox flow battery. *Journal of Membrane Science*, 585, 230-237.

[91] Kim, S., Choi, J., Choi, C., Heo, J., Kim, D. W., Lee, J. Y., Hong, Y. T., Jung, H. T., & Kim, H. T. (2018). Pore-size-tuned graphene oxide frameworks as ion-selective and protective layers on hydrocarbon membranes for vanadium redox-flow batteries. *Nano Letters*, 18(6), 3962-3968.

[92] Zhou, X. L., Zhao, T. S., An, L., Zeng, Y. K., & Zhu, X. B. (2016). Performance of a vanadium redox flow battery with a VANADion membrane. *Applied Energy*, 180, 353-359.

[93] Wang, W., Luo, Q., Li, B., Wei, X., Li, L., & Yang, Z. (2013). Recent progress in redox flow battery research and development. *Advanced Functional Materials*, 23(8), 970-986.

[94] Rahman, F., & Skyllas-Kazacos, M. (2009). Vanadium redox battery: Positive half-cell electrolyte studies. *Journal of Power Sources*, 189(2), 1212-1219.

[95] Tian, F., Wang, L., & Wang, C. S. (2018). The effect of phosphate additive on the positive electrolyte stability of vanadium redox flow battery. *Journal of Energy Chemistry*, 27(5), 1376-1380.

[96] Wang, G., Chen, J., Wang, X., Tian, J., Kang, H., Zhu, X., Zhang, Y., Liu, X., & Wang, R. (2014). Study on stabilities and electrochemical behavior of V (V) electrolyte with acid additives for vanadium redox flow battery. *Journal of Energy Chemistry*, 23(1), 73-81.

[97] Vijayakumar, M., Nie, Z., Walter, E., Hu, J., Liu, J., Sprenkle, V., & Wang, W. (2015). Understanding aqueous electrolyte stability through combined computational and magnetic resonance spectroscopy: a case study on vanadium redox flow battery electrolytes. *ChemPlusChem*, 80(2), 428-437.

[98] Yang, Y., Zhang, Y., Liu, T., & Huang, J. (2019). Improved broad temperature adaptability and energy density of vanadium redox flow battery based on sulfate-chloride mixed acid by optimizing the concentration of electrolyte. *Journal of Power Sources*, 415, 62-68.

---

[99] Jia, Z., Wang, B., Song, S., & Chen, X. (2012). Effect of polyhydroxy-alcohol on the electrochemical behavior of the positive electrolyte for vanadium redox flow batteries. *Journal of the Electrochemical Society*, 159(6), A843-A847.

[100] Shen, J., Liu, S., He, Z., & Shi, L. (2015). Influence of antimony ions in negative electrolyte on the electrochemical performance of vanadium redox flow batteries. *Electrochimica Acta*, 151, 297-305.

[101] Li, B., Gu, M., Nie, Z., Shao, Y., Luo, Q., Wei, X., Li, X., Xiao, J., Wang, C., Sprenkle, V., & Wang, W. (2013). Bismuth nanoparticle decorating graphite felt as a high-performance electrode for an all-vanadium redox flow battery. *Nano Letters*, 13(3), 1330-1335.

[102] Kear, G., Shah, A. A., & Walsh, F. C. (2012). Development of the all-vanadium redox flow battery for energy storage: a review of technological, financial and policy aspects. *International Journal of Energy Research*, 36(11), 1105-1120.

[103] Shigematsu, T. (2011). Redox flow battery for energy storage. *SEI Technical Review*, 73(7), 4-13.

[104] Satola, B. (2021). Bipolar Plates for the Vanadium Redox Flow Battery. *Journal of The Electrochemical Society*, 168 060503.

[105] Satola, B., Komsiyska, L., & Wittstock, G. (2018). Corrosion of graphite-polypropylene current collectors during overcharging in negative and positive vanadium redox flow battery half-cell electrolytes. *Journal of The Electrochemical Society*, 165.5 (2018): A963- A969.

[106] Caglar, B., Fischer, P., Kauranen, P., Karttunen, M., & Elsner, P. (2014). Development of carbon nanotube and graphite filled polyphenylene sulfide based bipolar plates for all-vanadium redox flow batteries. *Journal of Power Sources*, 256 88-95.

[107] Schweiss, R., Schmitt, R., & Oettinger, O. (2011). Carbon and graphite components for redox flow batteries. Influence of material properties on electrode and battery performance. *Conference paper, Annual World Conference on Carbon 2011*, Curran Associates Inc.

[108] https://www.sglcarbon.com/pdf/SGL-Datasheet-SIGRACELL-Bipolar-Plates-EN.pdf (accessed 10/04/2022).

[109] Dongjiang, Y., Jingyuan, L., & Litao, K. (2020). High-temperature conductive binder for an integrated electrode bipolar plate and its application in vanadium redox flow battery. *International Journal of Energy Research*, 44(3), 1920-1929.

[110] Lim, J. W. (2015). Carbon fiber/polyethylene bipolar plate-carbon felt electrode assembly for vanadium redox flow batteries (VRFB). *Composite Structures*, 134, 483-492.

[111] Gerhardt, M. R., Wong, A. A., & Aziz, M. J. (2018). The effect of interdigitated channel and land dimensions on flow cell performance. *Journal of The Electrochemical Society*, 165(11), A2625-A2643.

[112] Aramendia, I., Fernandez-Gamiz, U., Martinez-San-Vicente, A., Zulueta, E., & Lopez-Guede, J. M. (2021). Vanadium Redox Flow Batteries: A Review Oriented to Fluid-Dynamic Optimization. *Energies*, 14(1), 176.

[113] Tang, A., Bao, J., & Skyllas-Kazacos, M. (2014). Studies on pressure losses and flow rate optimization in vanadium redox flow battery. *Journal of Power Sources*, 248, 154-162.

[114] Chang, C. H., Chou, H. W., Hsu, N. Y., & Chen, Y. S. (2016). Development of integrally molded bipolar plates for all-vanadium redox flow batteries. *Energies*, 9(5), 350.

---

[115] Greese, T., & Rieth, T. (2018). *Monopolarplattenbauteil für chemische Reaktoren, insbesondere für Redox-Flow-Batterien, Verfahren zur Herstellung eines Monopolarplattenbauteils und Redox-Flow-Batterie mit einem solchen Monopolarplattenbauteil* (DE 10 2018 200 818 A1). Deutsches Patent- und Markenamt. https://depatisnet.dpma.de/DepatisNet/depatisnet?action=pdf&docid=DE102018200818A1 (accessed 11/04/2022).

[116] Karvonen, S., Hottinen, T., Ihonen, J., & Uusalo, H. (2008). Modeling of polymer electrolyte membrane fuel cell stack end plates. *Journal of Fuel Cell Science and Technology*, 5(4) 041009.

[117] Lin, P., Zhou, P., & Wu, C. W. (2011). Multi-objective topology optimization of end plates of proton exchange membrane fuel cell stacks. *Journal of Power Sources*, 196(3), 1222-1228.

[118] Kim, J. S., Park, J. B., Kim, Y. M., Ahn, S. H., Sun, H. Y., Kim, K. H., & Song, T. W. (2008). Fuel cell end plates: a review. *International Journal of Precision Engineering and Manufacturing*, 9(1), 39-46.

[119] Masa, J., Batchelor-McAuley, C., Schuhmann, W., & Compton, R. G. (2014). Koutecky-Levich analysis applied to nanoparticle modified rotating disk electrodes: electrocatalysis or misinterpretation. *Nano Research*, 7(1), 71-78.

[120] Schmidt, T. J., Gasteiger, H. A., Stäb, G. D., Urban, P. M., Kolb, D. M., & Behm, R. J. (1998). Characterization of high-surface-area electrocatalysts using a rotating disk electrode configuration. *Journal of the Electrochemical Society*, 145(7), 2354-2358.

[121] Yamamura, T., Watanabe, N., Yano, T., & Shiokawa, Y. (2005). Electron-transfer kinetics of Np^{3+}⁄Np^{4+}, NpO_2^{+}⁄NpO_2^{2+}, V^{2+}⁄V^{3+}, and VO^{2+}⁄VO_2^{+} at carbon electrodes. *Journal of The Electrochemical Society*, 152(4), A830-A836.

[122] Uhlemann, M., Krause, A., Chopart, J. P., & Gebert, A. (2005). Electrochemical deposition of Co under the influence of high magnetic fields. *Journal of the Electrochemical Society*, 152(12), C817-C826.

[123] Nguyen, T. Q., & Breitkopf, C. (2018). Determination of diffusion coefficients using impedance spectroscopy data. *Journal of The Electrochemical Society*, 165(14), E826-E831.

[124] Chang, J. H., Park, J., Pak, Y. K., & Pak, J. J. (2007). Fitting improvement using a new electrical circuit model for the electrode-electrolyte interface. *IEEE Proceedings of the 3rd International IEEE/EMBS Conference on Neural Engineering* (572-574).

[125] Goldstein, J. I., Newbury, D. E., Michael, J. R., Ritchie, N. W., Scott, J. H. J., & Joy, D. C. (2017). *Scanning electron microscopy and X-ray microanalysis.* Springer.

[126] Oura, K., Lifshits, V. G., Saranin, A. A., Zotov, A. V., & Katayama, M. (2013). *Surface science: an introduction.* Springer Science & Business Media.

[127] Zhu, G., & Ren, H. (2014). *Porous Organic Frameworks: Design, Synthesis and Their Advanced Applications.* Springer.